Correlation and decomposition concepts for identifying and disentangling flow structures Framework and insights into turbulence organization

Mukherjee, Siddhartha; Mascini, Merlijn; Portela, Luis M.

DOI
10.1063/5.0075914

Publication date
2022

Document Version
Final published version

Published in
Physics of Fluids

Correlation and decomposition concepts for identifying and disentangling flow structures: Framework and insights into turbulence organization

Cite as: Phys. Fluids **34**, 015119 (2022); https://doi.org/10.1063/5.0075914
Submitted: 19 October 2021 • Accepted: 21 December 2021 • Published Online: 18 January 2022

Siddhartha Mukherjee, Merlijn Mascini and Luis M. Portela

Physics of Fluids ARTICLE scitation.org/journal/phf

Correlation and decomposition concepts for identifying and disentangling flow structures: Framework and insights into turbulence organization

Cite as: Phys. Fluids **34**, 015119 (2022); doi: 10.1063/5.0075914
Submitted: 19 October 2021 · Accepted: 21 December 2021 ·
Published Online: 18 January 2022

Siddhartha Mukherjee,[1,2] Merlijn Mascini,[1] and Luis M. Portela[1,a)]

AFFILIATIONS

[1]Section of Transport Phenomena, Department of Chemical Engineering, Delft University of Technology, 2629 HZ Delft, The Netherlands
[2]International Centre for Theoretical Sciences, Tata Institute of Fundamental Research, Bengaluru 560089, India

[a)]Author to whom correspondence should be addressed: L.Portela@tudelft.nl

ABSTRACT

Turbulence and its organization, long conceptualized in terms of "coherent structures," has resisted clear description. A significant limitation has been the lack of tools to identify instantaneous, spatially finite structures, while unraveling their superposition. We present a framework of generalized correlations, which can be used to readily define a variety of correlation measures, aimed at identifying field patterns. Coupled with Helmholtz-decomposition, this provides a paradigm to identify and disentangle structures. We demonstrate the correlations using vortex-based canonical flows and then apply them to incompressible, homogeneous, isotropic turbulence. We find that high turbulence kinetic energy (E_k) regions form compact *velocity-jets* that are spatially exclusive from high enstrophy (ω^2) regions that form *vorticity-jets* surrounded by *swirling velocity*. The correlation fields reveal that the energetic structures in turbulence, being invariably jets, are distinct from those in vortex-based canonical flows, where they can be jet-like as well as swirling. A full Biot–Savart decomposition of the velocity field shows that the velocity-jets are neither self-induced, nor induced by the interaction of swirling, strong vorticity regions, and are almost entirely induced, non-locally, by the permeating intermediate range (rms level) vorticity. Velocity-swirls, instead, are a superposition of self-induced and background-induced velocity. Interestingly, it is the mild *intermediate* vorticity that dominantly induces the velocity-field everywhere. This suggests that turbulence organization could result from non-local and non-linear field interactions, leading to an emergent description unlike the notion of a strict structural hierarchy. Our correlation-decomposition framework lends itself readily to the study of generic vector and scalar fields associated with diverse phenomena.

I. INTRODUCTION

"Structure" in a field can be defined as a distribution of the properties of the field in a region, characterized by a small number of parameters, which can be described (deterministically) in a "simple way." For instance, in a velocity field, swirling motion is a kind of structure, which brings to mind examples such as a tornado, a cyclone, or a simple bathtub vortex. The concept of structure in flow fields immediately also invokes the notion of "coherent motion," which we interpret as regions of the flow that have a certain spatial pattern (as in a swirling motion). This idea of structure can also be understood by considering its opposite, i.e., a structure-less field, which mathematically may be defined as random. In this context, structure can also be conceptually related to the idea of information entropy, where a highly organized structure is easily described using a few parameters and is a low information entropy state of the underlying field. The Laminar flow in a pipe, for instance, is a very low (information) entropy flow state, whereas turbulence fields are the opposite, being a complex tangle of structure and randomness.

Structure in a general field, and, in particular, in a velocity field, can be the result of (arbitrary) choices in constructing the field and of the (intrinsic) dynamics of the field. For example, the addition of a translation or a rotation generates a coherent motion that is not related to the intrinsic dynamics of the velocity field. The pattern of the field at infinity can be seen as the result of these arbitrary choices, and it

can be "removed," in order to obtain patterns associated with the (intrinsic) dynamics of the field. In classical Newtonian mechanics, this is equivalent to observing the motion with respect to the "distant stars." The use of correlation and Helmholtz decomposition concepts allows the generalization of these ideas, which are essential for deciphering instrinsic field structures. For instance, the spatial correlation of a field over a sphere with an infinite radius can be made zero by performing an opposite transformation in the field (e.g., a translation or a rotation). From a Helmholtz decomposition perspective, this is equivalent to making a transformation in the field such that the generalized contribution of any region of the infinity-field (far-field contribution from "large distances") becomes equal to zero. We apply these techniques to study turbulence, to investigate both the structures that arise in turbulent flows and the makeup of these structures from a Helmholtz decomposition perspective.

Turbulent flows have been found to be very rich in structure across different representational spaces, so much so that turbulence has been held synonymous to structure.[1] In describing velocity field structures in turbulence, a key idea often used, albeit ill-defined, is that of the "eddy," which also refers to coherent regions of swirling motion. The superposition of eddies (or coherent motion across all scales) has served as the conceptual background upon which most of turbulence theory has been built.[2,3] How these coherent structures arise across all scales, and what they look like, however, is not fully known. In this paper, we are interested in finding out whether the finite-sized spatial structures comprising turbulence can be identified and isolated in the vector fields where they are believed to arise. Furthermore, we are interested in considering instantaneous structures, which are continuously produced and destroyed, and are not the result of an averaging procedure. According to the conventional "cascade" perspective, these structures may range from the largest scales that contain most of the kinetic energy and "drive" the dynamics, to the small scales associated with the dissipation of kinetic energy. In this context, it should be noted that the smallest scales are merely a *consequence* of the turbulence dynamics and are, hence, not dynamically significant in determining the overall flow.[1]

There have been various approaches aimed at identifying coherent structures in different contexts that are prevalent in the turbulence literature. Most widely used are techniques based upon the velocity gradient tensor ($A_{ij} = \partial u_i/\partial x_j$) and its symmetric ($S_{ij}$) and skew-symmetric ($\Omega_{ij}$) parts. For instance, Hunt *et al.*[4] proposed velocity-gradient and pressure based measures to identify streamline patterns described as "eddies," "streams," and "convergence zones." Jeong and Hussain[5] defined a criterion (called λ_2) based on the eigenvalues of the local pressure Hessian, which is related to S_{ij} and Ω_{ij}. Dubief and Delcayre[6] used the second and third invariants (Q and R) of A_{ij}, originally used to characterize the topology of point flow patterns,[7] and Haller[8] used the strain acceleration tensor along fluid trajectories. Farge and Pellegrino[9] used a wavelet decomposition to identify coherent and incoherent vorticity structures, Hussain[10] and Sirovich[11] studied statistically emerging lower dimensional attractors, while others have extensively studied Lagrangian structures crucial for material transport.[12–14] Non-linear equilibrium solutions have also been classified as exact coherent structures.[15–17] Lozano-Durán and Jiménez[18] studied spatio-temporally coherent vortical structures, while Siggia,[19] Kerr,[20] She, Jackson, and Orszag,[21] and Jiménez *et al.*[22] investigated the structure of strong vorticity (worms) in incompressible homogeneous isotropic turbulence, and Moisy and Jiménez[23] quantified the large-scale spatial distribution of small, localized, intense vorticity worms.

These (and many other) studies and techniques have greatly informed our understanding of coherent structures in turbulence. Several of these studies use a "functional decomposition" approach (e.g., wavelet and spectral decomposition) to study the coherent structures, their relations and "hierarchy"; e.g., Argoul *et al.*[24] and Alexakis and Biferale[25] address the cascade concept[26] using wavelet and spectral decompositions, respectively. Modal analysis[27] see recent reviews,[28,29] and lower-order models[30] have also been widely used. Recently, machine learning approaches are also being introduced to "learn" and reproduce turbulence fields and patterns.[31,32] However, when using a functional decomposition approach, the turbulence fields are separated into "classes" and this "class perspective" does not represent individual coherent structures and their relations, occurring in the actual physical space. Machine learning methods also serve different purposes, viz. data assimilation, prediction, and aiding computational fluid dynamics models, but so far they have not been applied to identifying and extracting individual flow structures.

Many basic concepts associated with coherent structures, like the existence of a hierarchy of coherent structures (as invoked, for instance, in the Richardson[26] cascade), or the energetic interaction of eddies[33] and eddy breakups, have remained intractable in the physical space, where these ideas were first envisioned. Part of this disconnect is due to the lack of tools designed to identify instantaneous spatial structures, which may be driving these processes. The other issue is extracting these structures from their obfuscating scale superposition in order to study their form and dynamics.

To address these issues, we use correlation and Helmholtz-decomposition concepts, which enable us to identify and extract individual flow structures from turbulence fields. In this study, we deal with incompressible, homogeneous, isotropic turbulence, with a zero mean velocity; hence, the removal of a velocity pattern associated with an "artificial frame of reference" is not an issue. We approach the concept of coherent structures with a focus on the following key aspects:

1. **Finite structure size**—We consider a coherent structure to be a finite region of spatio-temporal organization, which represents a unit of coherent motion (e.g., an eddy is a coherent structure in which the coherent motion is a swirling velocity field). It must, hence, have a spatial form, that is to say, it cannot be completely irregular. "Coherence," in this context, becomes almost synonymous to "correlation," as an ordered spatial structure must comprise of a neighborhood of vectors that are strongly correlated (either positively or negatively).
   Here, it becomes important to highlight the distinction from *point-criteria*, which are based on the velocity gradient tensor (or derivatives thereof, like Q, R, etc.), or *Fourier/orthogonal* decomposition methods, for reducing structures. Essentially, these techniques represent two extremes. Point-criteria describe *point-structures*, reasoning from the Taylor expansion perspective of the velocity field in the infinitesimal neighborhood of each point in the flow field. Therefore, in general, point-criteria may not identify *finite* size structures. For example, both the "$Q - R$"[7] and "λ_2"[5] criteria identify the flat plate boundary layer as a vortex, while the λ_2-criterion can miss the identification of a Burgers vortex, depending upon its parameters.[34,35] Fourier or other

functional decompositions describe the energetics of *space-filling* modes, which serve as proxies for structure. However, a field containing a single structure like an isolated Burgers vortex, perturbs multiple Fourier modes, and the spectra does not reveal either the location, or the form of the structure being represented.

Additionally structures, being finite, may not necessarily relate to the local velocity gradients, as the velocity at a point results from spatial integrals of the velocity derivatives. The form and location of a finite-sized field structure, further, do not have an identifiable or distinct spectral footprint. Therefore, it is important to have a framework for structure education where this "finite aspect" is incorporated *a priori*, which is what we provide in this work.

2. **Instantaneity**—The spatial structures described above exist instantaneously and are not consequences of averaging procedures. In fact, a structure will have an entire lifecycle, from generation until destruction (driven by the dynamics of the Navier–Stokes equations). While ignoring the temporal evolution of the structures, in this work, we limit ourselves to identifying structures in instantaneous realizations (i.e., snapshots) of turbulence fields. Hence, we consider only the geometry of structures and not their kinematics or dynamics.
3. **Disentangling structures**—Part of the complexity of turbulence fields comes from the superposition of structures, which makes it difficult to even define, let alone extract and study, an individual structure. The reason for this superposition of (velocity field) structures can be understood from the Biot–Savart law, which gives that the velocity at each point in space is generated by the *spatial* integrals of quantities associated with the gradients of the velocity. The integrals account for both *near-field* and *far-field* contributions. The summative nature of the Biot–Savart law, hence, provides a paradigm for *disentangling* the contributions that generate any given velocity field pattern or structure, as different contributions may be isolated by employing suitable conditional sampling criteria on the velocity reconstruction. We use this method to identify regions of the velocity gradient field, which "generates"—in a Biot–Savart sense—a particular velocity structure.

The tools developed in this study, namely, a set of generalized correlation measures, along with velocity reconstruction using the Biot–Savart law, allow us to look at turbulence fields from a different perspective; for instance, they enable us to identify the structure of high kinetic energy and high enstrophy regions. Reconstructing the velocity field using the Biot–Savart law, furthermore, reveals the distribution of the vorticity contributions in the generation of these structures, and in the generation of the total velocity field. Note that Biot–Savart decomposition has been previously used to define local and non-local strain[36] and separate local shear-layer contributions to velocity generation.[37] However, it has not been used to study field composition at the level and context of *individual* coherent structures that arise in turbulence. Our correlation measures serve an important first step in realizing that, by aiding unambiguous identification of local coherent regions. This allows easily separating local and non-local vorticity contributions to the generation of velocity field structures. The *combination* of correlation and decomposition, hence, is what we propose in this work.

Conceptually, this paves the way for studying turbulence as a dynamical system of interacting structures that arise in its physical fields, the interplay between which manifests as the dynamics. Our results also give novel insights into the emergence of flow organization.

The layout of this paper is as follows:

1. In Sec. II, the concept of generalized correlation is introduced. Using this, some specific instantaneous correlation measures, designed to identify simple vector-field structures in flows, are proposed in Sec. III, together with correlations motivated by the Biot–Savart law in Sec. IV.
2. In Sec. V, all correlations are tested on several vortex-based canonical flows, where we focus on the relation between the correlation field features viz-a-vis the flow fields.
3. In Sec. VI, the correlations are applied to incompressible homogeneous isotropic turbulence fields. Correlation fields are discussed and analyzed in the light of the canonical flows examples, and the differences therein are highlighted, revealing certain features of the turbulence structures.
4. In Sec. VII, we focus on individual turbulence structures. Using the Biot–Savart law, we qualitatively show and quantify the vorticity composition of these structures, and of the total velocity field; i.e., we decompose the structures and the velocity field according to their "generation" by different parts of the vorticity field.
5. We conclude this study in Sec. VIII, describing the Biot–Savart picture of the emergence of structure and coherence in turbulence, resulting from the application of our tools. Avenues for expanding this study, together with the general applicability of our tools to diverse fields, are also discussed.

II. GENERALIZED CORRELATION

Correlation, in its most general form, can be interpreted as the relation between one region of a phase-space (or a field) with another; the two regions and their relation being defined based upon certain rules, when viewed from another phase-space region (the region of observation). This can be expressed as the relation between $\mathcal{R}_1(\mathcal{S}_1, \mathcal{T}_1)$ and $\mathcal{R}_2(\mathcal{S}_2, \mathcal{T}_2)$ as viewed from $\mathcal{R}_0(\mathcal{S}_0, \mathcal{T}_0)$, as illustrated in Fig. 1. Here, $\mathcal{S}$ denotes a space-set (e.g., a bounded continuous region or a set of points), $\mathcal{T}$ denotes a time-set (e.g., a continuous time interval or a set of time instances), and $\mathcal{R}$ denotes a phase-space-set defined over $(\mathcal{S}, \mathcal{T})$ (which could be defined, for example, using the velocity field or the pressure field). Based upon a set of rules given by any function ψ, defined over $\mathcal{S}_1, \mathcal{S}_2, \mathcal{S}_o, \mathcal{T}_1, \mathcal{T}_2, \mathcal{T}_o$, the original

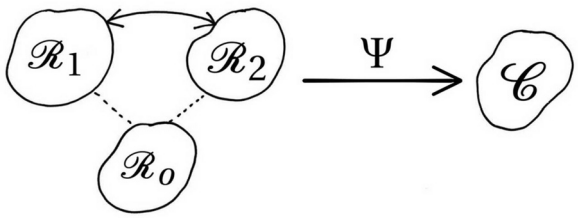

FIG. 1. Correlation between phase-space regions $\mathcal{R}_1$ and $\mathcal{R}_2$, as observed from phase-space region $\mathcal{R}_0$; each region is defined over a space-set $\mathcal{S}$ and a time-set $\mathcal{T}$. Using a function ψ, these regions are mapped onto a correlation space, producing a region shown here as $\mathcal{C}$.

phase-space-sets can be mapped to a correlation-set $\mathcal{C}$, with appropriate dimensions, based upon the definition of ψ.

The usual definition of the two-point correlation tensor for turbulent flows can be seen as a particular case of this generalized definition, where the definition, additionally, also involves *statistical* (averaging) concepts, with the phase-space-sets being composed of an ensemble of different realizations, making it a statistical measure. We first frame the usual definition of the two-point correlation tensor in the context of this generalized definition. Then, via analogy, we will define a *deterministic* two-point correlation, in order to characterize the structure of individual fields. Note that since the usual definition of the two-point correlation tensor is a statistical-concept, applied to an ensemble of different field realizations, it is not necessarily a good representation of the structure of each *individual* field. On the other hand, the deterministic two-point correlation that we will define contains a (simplified) characterization of the structure of each individual field.

The usual two-point correlation tensor for turbulent flows is defined as

$$\mathcal{R}_{ij}(\mathbf{x}, \mathbf{r}, t, \Delta t) = \langle u_i(\mathbf{x}, t) u_j(\mathbf{x} + \mathbf{r}, t + \Delta t) \rangle, \tag{1}$$

where $\mathbf{x}$ denotes a position, $\mathbf{r}$ is the separation between two positions, t is the time, Δt is the difference between two times, $\mathbf{u} = (u_x, u_y, u_z)$ is the velocity at a given position and time, and $\langle \cdot \rangle$ is ensemble averaging. In the context of the generalized correlation, this definition can be framed as

- $\mathcal{S}_1$ and $\mathcal{S}_2$: spatial regions of interest, containing $\mathbf{x}$ and $\mathbf{x} + \mathbf{r}$, respectively,
- $\mathcal{T}_1$ and $\mathcal{T}_2$: time intervals of interest, containing t and $t + \Delta t$, respectively,
- $\mathcal{R}$: phase-space-set, composed of the ensemble of velocity fields defined over $\mathcal{S}$ and $\mathcal{T}$. So, $\mathcal{R}_1(\mathcal{S}_1, \mathcal{T}_1) = \cup_n \mathbf{u}_n(\mathcal{S}_1, \mathcal{T}_1)$ and $\mathcal{R}_2(\mathcal{S}_2, \mathcal{T}_2) = \cup_n \mathbf{u}_n(\mathcal{S}_2, \mathcal{T}_2)$,
- $\mathcal{S}_0 = \mathcal{S}_1$, $\mathcal{T}_0 = \mathcal{T}_1$, $\mathcal{R}_0 = \mathcal{R}_1$,
- ψ, a function composed of a deterministic part, defined over the individual velocity fields of the ensemble, $\mathbf{u}_n = (u_{x,n}, u_{y,n}, u_{z,n})$, and a statistical part:
  - Elements of the deterministic part:

$$\psi_{ij,n}(\mathbf{x}, \mathbf{r}, t, \Delta t) = u_{i,n}(\mathbf{x}, t) u_{j,n}(\mathbf{x} + \mathbf{r}, t + \Delta t).$$

  - Elements of the statistical part:

$$\overline{\psi_{ij}}(\mathbf{x}, \mathbf{r}, t, \Delta t) = \langle \psi_{ij}(\mathbf{x}, \mathbf{r}, t, t + \Delta t) \rangle,$$

    where $\langle \cdot \rangle$ denotes ensemble averaging, which is usually a linear operator (e.g., arithmetic averaging); however, different (nonlinear) operations could also be used, leading to definitions different from the usual two-point two-time correlation tensor.

Therefore, in the context of the generalized definition, it results that the usual two-point two-time correlation can be defined as $\mathcal{C}(\mathcal{R}_1, \mathcal{R}_2)$, whose elements are given by the correlation tensor

$$\mathcal{R}_{ij}(\mathbf{x}, \mathbf{r}, t, \Delta t) = \overline{\psi_{ij}}(\mathbf{x}, \mathbf{r}, t, \Delta t). \tag{2}$$

By considering $\Delta t = 0$, i.e., $\mathcal{T}_1 = \mathcal{T}_2$, the two-point two-time correlation tensor is reduced to the usual two-point correlation tensor,

$$\mathcal{R}_{ij}(\mathbf{x}, \mathbf{r}, t) = \langle u_i(\mathbf{x}, t) u_j(\mathbf{x} + \mathbf{r}, t) \rangle. \tag{3}$$

This is a tensor with nine components, which for a generic turbulent flow is a function of $\mathbf{x}$, $\mathbf{r}$, and t. It contains a lot of information (from a statistical perspective); however, for some turbulent flows, the information needed for its characterization can be significantly reduced. In particular, for incompressible homogeneous isotropic turbulence: (i) due to homogeneity, the dependence on $\mathbf{x}$ disappears and (ii) due to isotropy, the dependence on $\mathbf{r}$ reduces to a dependence on the radial distance $r = |\mathbf{r}|$ alone. The velocity $\mathbf{u}$ can be decomposed into components parallel ($\mathbf{u}_\parallel$) and perpendicular ($\mathbf{u}_\perp$) to $\mathbf{r}$, yielding two correlation functions: (i) $f(r, t)$ (longitudinal) associated with the correlation of $\mathbf{u}_\parallel$ and (ii) $g(r, t)$ (transverse) associated with the correlation of $\mathbf{u}_\perp$. These two correlation functions completely characterize the usual two-point correlation tensor, and if the turbulence is also statistically steady, they depend only on r. Finally, a simplified characterization of the two correlation functions can be given by integral lengths, obtained by integrating $f(r)$ and $g(r)$ over r. For an incompressible flow, continuity further imposes a relation between $f(r)$ and $g(r)$ (e.g., see Batchelor[38]) and the two-point correlation tensor is completely characterized by $f(r)$ alone, with a single associated integral length.

The usual two-point correlation is a statistical concept, which mixes measures of the structure of individual fields with a measure of the structure of their ensemble. In general, the structure of the ensemble does not represent the structure of individual fields; actually, it can be completely different. For example, homogeneous isotropic turbulence refers to the ensemble; the individual fields are often far from being homogeneous and isotropic.[2] The characterization of the structure using the usual two-point correlation, even of individual field realizations, only holds *statistically* (i.e., upon suitable spatial averaging). We propose a deterministic characterization of the individual (instantaneous) fields using a correlation definition similar to the one employed for the usual two-point correlation, but considering only the *deterministic* part of ψ. This will be supplemented by a simplified characterization of the correlation, using integral measures, which, since the individual fields are not homogeneous and isotropic, are different and more elaborate that the usual integral measures for homogeneous isotropic turbulence. This simplified characterization, even though incomplete, is more manageable.

We propose $\mathcal{C}(\mathcal{R}_1, \mathcal{R}_2)$ as a definition for the correlation of individual (instantaneous) vector fields, which, for the sake of concreteness, is illustrated here for the velocity field. Here, again $\mathcal{S}_1$ is the spatial region of interest containing $\mathbf{x}$, $\mathcal{S}_2$ is the spatial region of interest containing $\mathbf{x} + \mathbf{r}$, $\mathcal{T}_1 = \mathcal{T}_2$ is the time interval of interest containing t. The elements of the phase-space-sets are the velocity fields, and the phase-space-set of observation, $\mathcal{R}_0$, is equivalent to $\mathcal{R}_1$. The elements of $\mathcal{C}(\mathcal{R}_1, \mathcal{R}_2)$ are the correlation tensor fields

$$\mathcal{R}_{ij}(\mathbf{x}, \mathbf{r}, t) = \psi_{ij}(\mathbf{x}, \mathbf{r}, t), \tag{4a}$$

$$\psi_{ij}(\mathbf{x}, \mathbf{r}, t) = u_i(\mathbf{x}, t) u_j(\mathbf{x} + \mathbf{r}, t). \tag{4b}$$

The separation vector $\mathbf{r}$ can be represented by a scalar, $r = |\mathbf{r}|$ denoting the separation distance, and a direction. In 3D space, this direction can be specified by two angles (and with only one angle in 2D), i.e., the azimuthal angle α and the elevation angle β. We can define the separation vector $\mathbf{r}_{\alpha\beta}$ as a vector of length r, which points along the direction specified by α and β, while being placed at point $\mathbf{x}$.

Hence, the correlation tensor can be written as $\mathcal{R}(\mathbf{x}, \mathbf{r}_{\alpha\beta}, t)$, which is a function of seven variables, namely, $x, y, z, r, \alpha, \beta, t$, where x, y, and z are the Cartesian components of $\mathbf{x}$. Since in this work, we limit ourselves to identifying structures in instantaneous field realizations, for the remainder of this paper, we will omit the time dependence t. The correlation tensor can then be expressed in the matrix form as

$$\mathcal{R}(\mathbf{x}, \mathbf{r}_{\alpha\beta}) = \begin{bmatrix} u_x(\mathbf{x})u_x(\mathbf{x}+\mathbf{r}_{\alpha\beta}) & u_x(\mathbf{x})u_y(\mathbf{x}+\mathbf{r}_{\alpha\beta}) & u_x(\mathbf{x})u_z(\mathbf{x}+\mathbf{r}_{\alpha\beta}) \\ u_y(\mathbf{x})u_x(\mathbf{x}+\mathbf{r}_{\alpha\beta}) & u_y(\mathbf{x})u_y(\mathbf{x}+\mathbf{r}_{\alpha\beta}) & u_y(\mathbf{x})u_z(\mathbf{x}+\mathbf{r}_{\alpha\beta}) \\ u_z(\mathbf{x})u_x(\mathbf{x}+\mathbf{r}_{\alpha\beta}) & u_z(\mathbf{x})u_y(\mathbf{x}+\mathbf{r}_{\alpha\beta}) & u_z(\mathbf{x})u_z(\mathbf{x}+\mathbf{r}_{\alpha\beta}) \end{bmatrix}. \tag{5}$$

This contains a lot of information, which needs to be reduced for practical reasons. Thus, instead of considering the entire $\mathcal{R}$ matrix, we work with one of its invariants, the trace, which is written as

$$\mathcal{R}_{ii}(\mathbf{x}, \mathbf{r}_{\alpha\beta}) = u_i(\mathbf{x})u_i(\mathbf{x} + \mathbf{r}_{\alpha\beta}). \tag{6}$$

This is easier to conceptualize, as the trace is also the dot product between the velocities at points $\mathbf{x}$ and $\mathbf{x} + \mathbf{r}_{\alpha\beta}$,

$$\mathcal{R}_{ii}(\mathbf{x}, \mathbf{r}_{\alpha\beta}) = \mathbf{u}(\mathbf{x}) \cdot \mathbf{u}(\mathbf{x} + \mathbf{r}_{\alpha\beta}). \tag{7}$$

A further reduction can be performed by integrating this quantity along directions specified by $\mathbf{r}_{\alpha\beta} = r\mathbf{e}_{\alpha\beta}$ (where $\mathbf{e}_{\alpha\beta}$ is the direction vector along α and β), to associate an integral measure $L_{\alpha\beta}(\mathbf{x}, \Lambda)$ along each direction as

$$L_{\alpha\beta}(\mathbf{x}, \Lambda) = \int_{r=0}^{\Lambda} \mathbf{u}(\mathbf{x}) \cdot \mathbf{u}(\mathbf{x} + r\mathbf{e}_{\alpha\beta})\, \mathrm{d}r. \tag{8}$$

The correlation tensor field is, hence, reduced to a 2D manifold around each point; i.e., around each point, we have a surface, which completely characterizes the structure of the field as a function of the elevation and azimuthal angles, as illustrated in Fig. 2. For a given Λ, its shape gives an integral measure of how this structure depends on the direction. For instance, the direction of maximum $L_{\alpha\beta}$ could be determined as a function of position; however, even though interesting in itself, this will not be explored here. Furthermore, this manifold is invariant under translation and rotation of the original coordinate axes, along with being invariant under reflection (similarly to an axial vector). In principle, such a manifold can be calculated for any vector field, leading, for a given Λ, to a correlation surface for each point in space. Since we shall utilize numerical datasets, the calculation of the manifold requires binning the angles α and β into discrete increments. The resolution of these angles will depend significantly upon the resolution of the data, where high resolution simulations will be required to accurately describe even a small subset of angles, along with demanding computational requirement to calculate the correlation manifold at each point in space.

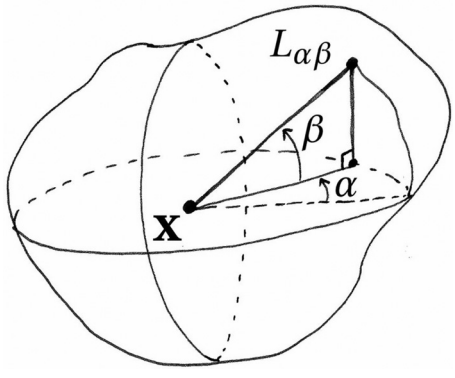

FIG. 2. A correlation surface around point $\mathbf{x}$, defined by the measure $L_{\alpha\beta}$ found by integrating $\mathcal{R}_{ii}(\mathbf{x}, \mathbf{r}_{\alpha\beta})$ up to distance Λ, along a direction specified by the angles α (azimuth) and β (elevation).

III. CORRELATION MEASURES FOR VELOCITY AND VORTICITY FIELDS

For the present study, we perform a final simplification where, instead of the entire manifold $L_{\alpha\beta}(\mathbf{x}, \Lambda)$, we represent it by a three-tuple $\mathbf{L}(\mathbf{x}, \Lambda)$, along three arbitrary orthogonal directions x, y, z (forming an orthonormal base), which can be summarized as

$$\mathbf{L}(\mathbf{x}, \Lambda) = \begin{bmatrix} L_x(\mathbf{x}, \Lambda) \\ L_y(\mathbf{x}, \Lambda) \\ L_z(\mathbf{x}, \Lambda) \end{bmatrix}, \tag{9}$$

where

$$L_i(\mathbf{x}, \Lambda) = \int_{r=-\Lambda}^{\Lambda} \mathbf{u}(\mathbf{x}) \cdot \mathbf{u}(\mathbf{x} + r\mathbf{e}_i)\, \mathrm{d}r,$$

where $\mathbf{e}_i \in \{\mathbf{e}_1, \mathbf{e}_2, \mathbf{e}_3\}$ represents the three spatial directions. Note that this three-tuple, being a simplification of the manifold, is also invariant to rotation, translation and reflection. Hence, $\mathbf{L}$ at each point $\mathbf{x}$ depends only on the choice of the arbitrary orthogonal bases used to "sample" the manifold.

Furthermore, $\mathbf{L}$ can be expected to yield large absolute values at points $\mathbf{x}$ that are surrounded by large regions in which (i) the local flow streamlines are well-aligned (such that the directions of $\mathbf{u}(\mathbf{x})$ and $\mathbf{u}(\mathbf{x} + \mathbf{r})$ are similar) and (ii) the magnitude of these vectors is high. The definition of $\mathbf{L}$, therefore, provides a *combined* measure of the organization and size of the identified structure and of the magnitude of the field in that region. In the limit $\Lambda \to 0$, $|\mathbf{L}| \to E_k$, but for all $\Lambda > 0$, $\mathbf{L}$ is a *non-local* measure of structure and, therefore, distinct from E_k, which is a point-criterion. Finite Λ values weigh in structure *size* in the correlation measure, and a very small field region with a high magnitude and a high structural organization will not yield large absolute values of $\mathbf{L}$. A separate consideration of the size of the structure could be achieved by analyzing the influence of Λ on $\mathbf{L}$. For "large" values of Λ, structures of all sizes can contribute to $\mathbf{L}$, with the larger ones being associated with larger absolute values of $\mathbf{L}$; hence, the analysis of the variation of $\mathbf{L}$ with Λ allows to separate the effect of the size from the structural organization and field magnitude effects. Moreover, in the limit $\Lambda \to \infty$, $\mathbf{L}$ might also be seen as a kind of "local" integral lengthscale.

The definition of $\mathbf{L}$ here does not include an implicit normalization and is sensitive to *both* the extent of spatial organization and the field magnitude. A normalized (and nondimensional) $\mathbf{L}$ could be achieved by dividing $L_i(\mathbf{x}, \Lambda)$ by the integral of E_k along the $\mathbf{e}_i$ direction, within the limits $-\Lambda < r < \Lambda$. This would allow identifying regions with structural organization alone, while disregarding the field magnitude. These two aspects could also be explicitly decoupled. For instance, a measure $\hat{\mathbf{L}}$ could be constructed, which operates on the *locally* normalized velocity field $\hat{\mathbf{u}}(\mathbf{x}) = \mathbf{u}(\mathbf{x})/|\mathbf{u}(\mathbf{x})|$. Such a measure can be used to focus purely on flow organization. These examples are

illustrative of how the correlations can be easily modified for particular applications, although we do not explore these possibilities here.

Another important aspect is the choice of Λ. We demonstrate the influence of Λ using canonical flows in Sec. V. Furthermore, in Sec. VI C, we perform a limited study to show that, for homogeneous, isotropic turbulence, the Taylor microscale is a good benchmark value for Λ.

A different correlation measure $\mathbf{L^s}$ (for $\mathbf{L}$-symmetric) is defined using the dot product between velocity pairs equidistant from $\mathbf{x}$, symmetrically, along a given direction, given as

$$L_i^s(\mathbf{x}, \Lambda) = \int_{r=0}^{\Lambda} \mathbf{u}(\mathbf{x} - r\mathbf{e}_i) \cdot \mathbf{u}(\mathbf{x} + r\mathbf{e}_i)\, \mathrm{d}r. \tag{10}$$

This measure is also expected to yield high values when the flow streamlines are parallel (or anti-parallel) in the Λ-neighborhood of $\mathbf{x}$, and when the magnitude of the vectors is high. Moreover, this measure will be more sensitive to the larger symmetries and anti-symmetries in the field. While $\mathbf{L}$ and $\mathbf{L^s}$ will in general be sensitive to different underlying flow patterns, in special cases like well-aligned streamlines, both correlations can be expected to yield high values.

Similarly, we define correlation measures $\mathbf{G}(\mathbf{x}, \Lambda)$ and $\mathbf{G^s}(\mathbf{x}, \Lambda)$ for the vorticity field $\boldsymbol{\omega} = \nabla \times \mathbf{u}$, which by analogy are given as

$$G_i(\mathbf{x}, \Lambda) = \int_{r=-\Lambda}^{\Lambda} \boldsymbol{\omega}(\mathbf{x}) \cdot \boldsymbol{\omega}(\mathbf{x} + r\mathbf{e}_i)\, \mathrm{d}r \tag{11}$$

and

$$G_i^s(\mathbf{x}, \Lambda) = \int_{r=0}^{\Lambda} \boldsymbol{\omega}(\mathbf{x} - r\mathbf{e}_i) \cdot \boldsymbol{\omega}(\mathbf{x} + r\mathbf{e}_i)\, \mathrm{d}r. \tag{12}$$

The correlation measure $\mathbf{G}$ is expected to yield large absolute values at points $\mathbf{x}$ that are surrounded by large regions in which (i) the *vorticity streamlines* (i.e., streamlines of the vorticity field) are well-aligned and (ii) the magnitude of the vorticity is high. The correlation measure $\mathbf{G^s}$ is the vorticity field equivalent of $\mathbf{L^s}$ and is expected to be more sensitive to the symmetries and anti-symmetries in the vorticity field, along with being sensitive to the vorticity magnitude. For simplicity of language, here onward we will refer to correlation measures as *correlations*.

Note that, in general, structures in the velocity and vorticity fields can be very different, with very different sizes and magnitudes; hence, the concept of "large regions" and "large values" is relative and needs to be interpreted in the individual context of the different correlation measures. In homogeneous isotropic turbulence, regions of high vorticity magnitude are related to the smaller scales of turbulence; they correspond to the long tails of the statistical distribution of the vorticity (i.e., $\omega \gg \omega'$ where $\omega' = \langle \omega^2 \rangle^{1/2}$) and occur intermittently. The $\mathbf{L}$ (and $\mathbf{L^s}$) and $\mathbf{G}$ (and $\mathbf{G^s}$) correlations give a separate (simplified) characterization of the structure of the individual (instantaneous) velocity and vorticity fields.

These correlations consider the velocity and vorticity fields separately; however, other correlations can be defined, which use both these fields, exploiting the relation between the velocity and vorticity. Particularly, the velocity field can be reconstructed from the vorticity field using the Biot–Savart law. This serves as an important tool to identify, as well as disentangle, structures, and is briefly described below.

IV. BIOT–SAVART RECONSTRUCTION AND ASSOCIATED CORRELATIONS

A. Biot–Savart reconstruction

We start with the Helmholtz decomposition, which states that a sufficiently smooth (twice continuously differentiable) vector field, defined on a bounded or an unbounded domain, can be uniquely decomposed into three components: (i) an irrotational vector field $\mathbf{D}$, (ii) a solenoidal vector field $\mathbf{C}$, and (iii) a harmonic vector field $\mathbf{B}$. Applied to the velocity field $\mathbf{u}$, this can be written as

$$\mathbf{u} = \mathbf{D} + \mathbf{C} + \mathbf{B}, \tag{13}$$

where

$$\mathbf{D} = \nabla\phi, \tag{14a}$$
$$\mathbf{C} = \nabla \times \boldsymbol{\varphi}, \tag{14b}$$
$$\mathbf{B} = \nabla\psi, \tag{14c}$$

and

$$\nabla^2\phi = \nabla \cdot \mathbf{u}, \tag{15a}$$
$$\nabla^2\boldsymbol{\varphi} = -\nabla \times \mathbf{u} = -\boldsymbol{\omega}, \tag{15b}$$
$$\nabla^2\psi = 0. \tag{15c}$$

In a bounded domain with a volume V and a bounding surface S, the three components can be written as a generalized Biot–Savart law (see, for instance, Wu *et al.*[39]),

$$\mathbf{D} = \frac{1}{4\pi}\int_V \frac{\nabla \cdot \mathbf{u}}{|\mathbf{r}|^3}\mathrm{d}V', \tag{16}$$

$$\mathbf{C} = \frac{1}{4\pi}\int_V \frac{\boldsymbol{\omega} \times \mathbf{r}}{|\mathbf{r}|^3}\mathrm{d}V', \tag{17}$$

$$\begin{aligned}\mathbf{B} &= -\frac{1}{4\pi}\int_S \frac{(\mathbf{n} \cdot \mathbf{u})\mathbf{r} + (\mathbf{n} \times \mathbf{u}) \times \mathbf{r}}{|\mathbf{r}|^3}\mathrm{d}S' \\ &= -\frac{1}{4\pi}\int_S \frac{(\mathbf{n} \cdot \mathbf{r})\mathbf{u} + (\mathbf{n} \times \mathbf{r}) \times \mathbf{u}}{|\mathbf{r}|^3}\mathrm{d}S',\end{aligned} \tag{18}$$

where $\mathbf{r}$ is the position vector, from a point in the volume V (or the surface S) to the point $\mathbf{x}$ where the integrals are being evaluated. The integrals over the volume V can be considered the "near-field" contribution, whereas the surface integral over the bounding surface S can be considered the "far-field" contribution. Any region within the domain has a bounding surface that separates it from the rest of the domain. Therefore, the integral over this bounding surface can be seen, representing the sum of the contributions of (i) the integral over the volume surrounding the region and (ii) the integral over the bounding surface of the whole domain.

In an unbounded (infinite) domain, the Helmholtz decomposition reduces to

$$\mathbf{u} = \mathbf{D} + \mathbf{C}, \tag{19}$$

provided that $\mathbf{B}$ goes to zero when $|\mathbf{r}|$ goes to infinity. This happens if the distance over which the velocity field is correlated along the surface grows slower than $|\mathbf{r}|$ when $|\mathbf{r}|$ goes to infinity.

This can be illustrated by considering an integral correlation measure L_α defined on the surface of a sphere, similarly to what was done for 3D, which is given as

$$L_\alpha(\mathbf{x}_s, \Lambda) = \int_{r_s=0}^{\Lambda} \mathbf{u}(\mathbf{x}_s) \cdot \mathbf{u}(\mathbf{x}_s + r_s \mathbf{e}_\alpha)\, \mathrm{d}r_s, \tag{20}$$

where $\mathbf{x}_s$ is a point on the surface of the sphere and $\mathbf{r}_s = r_s \mathbf{e}_\alpha$ denotes the separation from $\mathbf{x}_s$ on the surface of the sphere ($\mathbf{e}_\alpha$ is the direction of the unit-vector along the angle α on the surface; r_s is the distance from $\mathbf{x}_s$ on the surface along the angle α). Since this calculation is confined to the surface, the correlation around each point $\mathbf{x}$ is simply a function of an angle α and an integration length Λ, measured along the direction (on the surface) specified by α. In the Helmholtz decomposition, the contribution of the boundary to the velocity field (i.e., the contribution of $\mathbf{B}$ to $\mathbf{u}$) goes to zero if

$$\lim_{|\mathbf{r}|\to\infty} \frac{L_\alpha(\mathbf{x}_s, \Lambda)}{|\mathbf{r}|} = 0 \tag{21}$$

for any $\mathbf{x}$, α, and $\Lambda < \pi|\mathbf{r}|$ (see, for example, Phillips[40]). For an infinite domain, the contribution of $\mathbf{B}$ to the velocity field could be the result of an "organized motion over an infinite distance," which can be seen as the result of (arbitrary) choices in constructing the field (e.g., the choice of a particular frame of reference). This arbitrary artificial coherent motion, which is the "extrinsic motion" can be removed by making a transformation in the velocity field such that the condition given by Eq. (21) becomes true for any $\mathbf{x}$, α, and $\Lambda < \pi|\mathbf{r}|$; this condition will result in the integrals given by Eq. (18) becoming equal to zero for any surface S in the sphere, when the radius of the sphere goes to infinity.

When doing turbulent flow simulations with periodic boundary conditions, any arbitrary artificial coherent motion can be removed by not considering $\mathbf{B}$, provided that the domain is large enough to take into account any relevant "intrinsic motion"; i.e., provided that the domain is "significantly" larger than the distance over which the velocity field is correlated; this requires that the domain needs to be significantly larger than the integral length scale of the turbulence, which is our case. If this happens, for $|\mathbf{r}|$ larger than half the domain size, the contribution of $\mathbf{B}$ to the velocity approaches a constant, which can be made zero by neglecting $\mathbf{B}$ (which is equivalent to "choosing the appropriate frame of reference"). Actually, in our case, as usually true for turbulence simulations in triperiodic domains, this constant is already zero, since the mean velocity is equal to zero; as it will be shown, in this case $\mathbf{C}$ [i.e., Eq. (17)] gives a good approximation of $\mathbf{u}$ (since we deal with an incompressible flow, $\mathbf{D} = 0$) for $|\mathbf{r}|$ approaching the domain size.

With these considerations, the generalized Helmholtz decomposition reduces to the simplified Biot–Savart law, applicable for incompressible flows over periodic (or infinite) domains, which is given as

$$\mathbf{u}(\mathbf{x}) = \frac{1}{4\pi} \int_V \frac{\boldsymbol{\omega} \times \mathbf{r}}{|\mathbf{r}|^3} \mathrm{d}V'. \tag{22}$$

The Biot–Savart law provides a way to disentangle flow structures by isolating the contributions from different vorticity regions to a local velocity structure. For instance, *local* and *non-local* vorticity contributions can be separated using this paradigm, or the vorticity field can be conditionally sampled to identify the contribution of different vorticity levels in generating velocity field structures.

Note that, even though far-field vorticity contribution, i.e., $\mathbf{B}$, may be absent, the volumetric region can also be split into an isolated *local* region (V_L), surrounded by the *non-local* region (V_NL), which essentially behaves as a *far-field* for the region V_L. This leads to the consequence that, if the local region has negligible vorticity within V_L, while the non-local region V_NL *induces* a velocity field within V_L, then this velocity field must be a *potential flow*. This means that the local flow in V_L can be described by the gradient of a harmonic function ψ, i.e., $\mathbf{u}_\mathrm{L} = \nabla\psi$, while $\nabla^2\psi = 0$. The non-local contributions from V_NL *cannot* generate vorticity within the local region V_L (as illustrated in Fig. 3). A last feature to note regarding the Biot–Savart law is the rapid decay (of $1/r^2$ over a distance r) of the vorticity contribution, which means that a small, isolated, vorticity region cannot extend its influence over a large distance beyond its immediate neighborhood.

B. Correlations related to the Biot–Savart law

Ideas associated with the Biot–Savart law can be used to define correlation measures in order to identify, extract, and disentangle structures associated with the relation between the velocity and vorticity fields. In regions of strong vorticity associated with swirling-flow in the orthogonal plane, the Lamb vector, i.e., $\boldsymbol{\omega} \times \mathbf{u}$, yields high values. However, this is again a *local* quantity. We propose a correlation, which utilizes this idea and extends it to a *non-local* form, where the vorticity at point $\mathbf{x}$ is correlated with the velocity at point $\mathbf{x} + \mathbf{r}_i$, leading to a three-tuple $\mathbf{H}(\mathbf{x}, \Lambda)$, which, similarly to $\mathbf{L}(\mathbf{x}, \Lambda)$, can be written as follows:

$$H_i(\mathbf{x}, \Lambda) = \int_{r=-\Lambda}^{\Lambda} \left(\frac{\boldsymbol{\omega}(\mathbf{x}) \times r\mathbf{e}_i}{|r|} \right) \cdot \mathbf{u}(\mathbf{x} + r\mathbf{e}_i)\, \mathrm{d}r. \tag{23}$$

The above correlation has a flavor of the Biot–Savart law, and it allows correlating the contribution of the *local* vorticity $\boldsymbol{\omega}(\mathbf{x})$ with the *global* vorticity contribution to its neighboring velocity field, since the velocity $\mathbf{u}(\mathbf{x} + \mathbf{r}_i)$ can be seen as an integral result of the global vorticity field. Note that, with the above definition, $\mathbf{H}(\mathbf{x}, \Lambda)$ will tend to be *orthogonal* to $\boldsymbol{\omega}(\mathbf{x})$, as H_i (i.e., H along the $i-$direction) will have a high magnitude when the vorticity is large and orthogonal to the $i-$direction.

The strongest flow generated by vorticity at a point, in a Biot–Savart sense, is in the plane *orthogonal* to the vorticity vector; hence, a more natural correlation is defined, which takes into account this fact. This is done by correlating the vorticity along a particular direction, say x, to the flow in the orthogonal plane, i.e., yz. At each

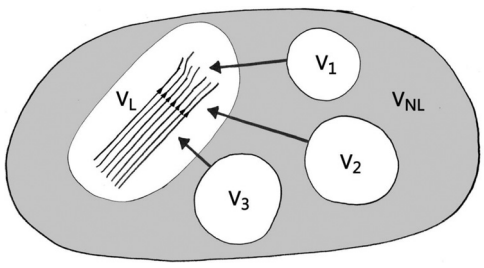

FIG. 3. Schematic of a Biot–Savart reconstruction of the velocity field in a region V_L, from three isolated non-local regions V_1, V_2, and V_3. When the region V_L has negligible vorticity of its own, the flow generated within the region by non-local vorticity contributions is a potential flow, which can be written as the gradient of a harmonic function ψ.

point, a velocity field is generated using the x-vorticity (i.e., ω_x) in the orthogonal yz-plane within a circular region (along perimeters of circles of radius $0 < r_{yz} \leq \Lambda$). This local velocity field is calculated with a simplification of the Biot–Savart law, by taking the cross product of the vorticity with unit vectors in the orthogonal plane ($\mathbf{r}_{yz}/|\mathbf{r}_{yz}|$), as done for the $\mathbf{H}$ correlation. This is illustrated in Fig. 4, where the ω_x vorticity component generates the velocity field shown in blue (solid lines), while the *real* velocity field generated from the global vorticity contributions is shown in red (dashed lines). The $\mathbf{H^p}$ correlation (for $\mathbf{H}-$*planar*) is calculated as the integral of the dot product between the vorticity-generated velocity vectors (blue) and the real velocity (red), over rings of radius $0 < r_{yz} < \Lambda$. Since the length of the rings increases proportionally with the radius r, the integral over each ring is further divided by r (i.e., $|\mathbf{r}_{yz}|$), to give an average correlation at a distance r, though other definitions can be used. This correlation is given by

$$H_x^p(\mathbf{x},\Lambda) = \int_0^\Lambda \frac{1}{|\mathbf{r}_{yz}|} \oint_{\mathcal{L}} \mathrm{d}l \left(\frac{\omega_x(\mathbf{x})\hat{i} \times \mathbf{r}_{yz}}{|\mathbf{r}_{yz}|} \right) \cdot \mathbf{u}(\mathbf{x}+\mathbf{r}_{yz})\, \mathrm{d}r_{yz}, \quad (24)$$

where $\hat{i}$ is the unit vector in the x-direction. H_y^p and H_z^p are defined in a similar way. Evidently, this correlation is more computationally expensive to calculate than $\mathbf{H}$, as three planar regions need to be considered for each point in space. This requirement can be relaxed by sampling the rings $0 < r \leq \Lambda$ with a chosen frequency, i.e., using every nth ring such that $r \in \{n, 2n, 3n, \ldots\}$.

$\mathbf{H^p}(\mathbf{x},\Lambda)$ can be seen as an area-integral correlation-measure of the planar (2D) version of $\mathbf{C}$ in Eq. (17) (see, e.g., Wu *et al.*[39]) with $\mathbf{u}$. In other words, it correlates the contribution of ω_x (the vorticity at $\mathbf{x}$) to $\mathbf{C}$ at $\mathbf{x}+\mathbf{r}$ with $\mathbf{u}$ at $\mathbf{x}+\mathbf{r}$; i.e., it correlates the value of $\mathbf{u}(\mathbf{x}+\mathbf{r})$ *due to* $\omega_x(\mathbf{x})$ with the *actual value* of $\mathbf{u}(\mathbf{x}+\mathbf{r})$. As shown in Fig. 4(a), when the local flow is swirling and is induced by the vorticity at its core, a strong correlation will be found. Meanwhile, a strong vorticity region immersed in a coherent uniform flow, Fig. 4(b) (or a disorganized flow), will give a weak correlation. This is because the "total" velocity field in the region is dominated by an "externally induced" flow (as illustrated in Fig. 3), which does not resemble the "self-induced" swirling motion due to the vorticity. This also highlights a simple scenario where velocity-gradient based criteria, in general, will be unable to identify coherent *velocity* patterns, while being able to find structures in the gradient fields.

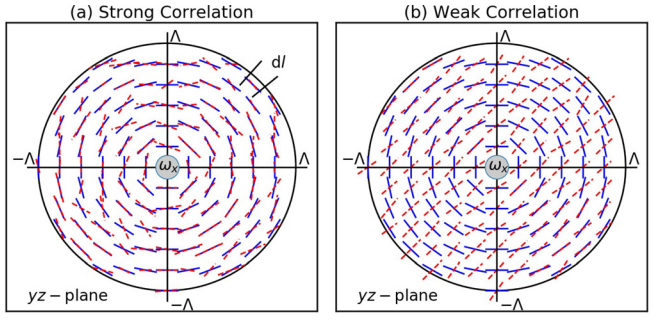

FIG. 4. Schematic of the $\mathbf{H^p}$ correlation, which gives (a) high values when the real velocity (red lines) is correlated with the Biot–Savart velocity (blue lines) generated by $\boldsymbol{\omega}$ within a radius Λ and (b) low values when these two velocity patterns are different.

Contrary to, e.g., $L_{\alpha\beta}(\mathbf{x},\Lambda)$, which is a line-integral correlation-measure over a distance Λ, $\mathbf{H^p}(\mathbf{x},\Lambda)$ is an area-integral correlation-measure over a disk of radius Λ. Similarly, different combinations of the 2D and 3D versions of $\mathbf{C}$, and line, area and volume integral correlation-measures can also be constructed. This may, further, be extended by defining correlations based upon locally defined coordinate axes that may align with the vorticity or strain eigenvectors, etc. Of course, any other vector or tensor fields of interest may also be employed. For example, correlations involving force density fields like the pressure-gradient and viscous stress could be of interest for studying turbulence as well, but we do not explore these in this work.

V. CORRELATIONS APPLIED TO SIMPLIFIED CANONICAL FLOWS

We begin by testing the correlations on 1D, 2D, and 3D flow fields resulting from the interaction of canonical vortices. This serves two purposes. First, it allows us to study features of the correlation measures themselves on fields that are well-defined. Second, the features found from canonical flows form the backdrop against which we shall study the correlations applied to turbulence in Sec. V A.

It has been proposed in the literature that structures in turbulence could be understood using the interaction of canonical vortices as a basis. For example, Hunt *et al.*[4] proposed that coherent flow patterns like streams and "convergent zones" could emerge in turbulence due to a distribution of eddies. While these structures indeed arise in flow fields resulting from the interaction of canonical vortices, whether turbulence gives rise to such organization remains to be seen. Our tools provide a way to test this idea.

A. One-dimensional fields

We construct a 1D velocity field along a line, starting with Oseen vortices, which can be defined by a tangential velocity field and a vorticity field, given as

$$u_\theta(r) = \frac{\Gamma}{2\pi r}\left[1 - \exp\left(-\frac{r^2}{4\nu t}\right)\right], \quad (25)$$

$$\omega_z(r) = \frac{\Gamma}{4\pi\nu t}\exp\left(-\frac{r^2}{4\nu t}\right), \quad (26)$$

where r is the radial distance from the vortex center, Γ is the circulation, ν is the fluid kinematic viscosity, and t is the time. The Oseen vortex comprises a small core region in (near) solid body rotation, within which the velocity increases radially as $u_\theta \propto r$ to its maximum value. Beyond this, there exists a (near) potential flow region where $\omega_z \approx 0$ and $u_\theta \propto 1/r$. We add a noise ζ to the velocity field given by Eq. (25), to generate a "structure immersed in noise." The vortex has a certain "reach," which depends on the amplitude of ζ, and is defined as the distance beyond which $\zeta > u_\theta$. The vorticity of the Oseen vortex is calculated in Cartesian coordinates as $\omega_z = \nabla \times \mathbf{u} = \partial u_y/\partial x - \partial u_x/\partial y$, and not using Eq. (26), due to the addition of the noise to the velocity field.

We generate a nondimensional, periodic velocity field of length $N_x = 500$ by placing two counter-rotating Oseen vortices at $x = 150$ and $x = 350$ and consider the velocity along the $x-$ axis to get the 1D velocity field u_y. The other parameters are chosen as $\Gamma = 10$, $\nu = 2.0$,

$t = 2.0$, and ζ is scaled to 1% of $|u_y|_{\max}$. Figure 5(a) shows u_y, which contains a pattern of symmetries and anti-symmetries. It consists of a "larger structure" (approximately in the range $50 < x < 450$), which is symmetric, except for the noise, with respect to its middle ($x \approx 250$). This structure contains the following sub-structures: (i) two Oseen velocity patterns around the center of each vortex (within approximately $100 < x < 200$ and $300 < x < 400$) and (ii) an almost uniform velocity region (roughly $200 < x < 300$) due to the interaction between the two vortices, which is reminiscent of the streams proposed by Hunt *et al.*[4]

Figures 5(b) and 5(c) show $\mathbf{L}$ and $\mathbf{L^s}$, respectively (which, here, only have a x-component, i.e., L_x and L_x^s). A few features of the correlation profiles point at the nature of the correlation definitions, as well as the importance of the choice of Λ. For $\Lambda = 250$, L_x is found to have a shape similar to the function itself. This follows from L_x involving products between (i) the value of the function at each point and (ii) the integral of the function between $-\Lambda < r_x < \Lambda$. Hence, if either of the two is zero, L_x becomes zero. L_x will have significant values where the function itself has significant values, and the structure of the function (i.e., its symmetries and/or anti-symmetries) does not make its integral small. However, the addition of the noise term breaks these symmetries here, such that the integral of the function becomes finite, and L_x, hence, has the same shape as the function itself for $\Lambda = 250$ (this is also true for G_x).

L_x^s for $\Lambda = 250$, in Fig. 5(c), has completely different features than L_x. It has a central peak around $x = 250$, exactly between the two counter-rotating vortices (although u_y is small there), associated with the symmetry of the larger structure since the velocity field is mirrored across this point (except ζ values). At the core of the two vortices ($x = 150$ and $x = 350$), where L_x becomes zero, L_x^s shows large negative peaks due to the anti-symmetry of the "local sub-structures," i.e., the Oseen vortices. L_x^s in the region of approximately $x < 100$ and $x > 400$ is a repetition of the central L_x^s profile (between $150 < x < 350$) due to the periodicity of u_y and the value of Λ spanning the complete field.

For $\Lambda = 35$ (or slightly different values), which roughly corresponds to the size of the individual vortices, L_x and L_x^s show some similarities and differences. At the vortex cores, where $u_y \approx 0$, $L_x \approx 0$, while L_x^s yields large negative peaks because of the anti-correlated velocity across the core region. In the potential flow regions of the two vortices and the uniform, streaming, flow region between the vortices, the general shape of the two correlations is similar, with both L_x and L_x^s yielding positive correlation values. Here, we highlight a crucial aspect that corresponding to regions of swirling flow (or eddies), the patterns in $\mathbf{L}$ and $\mathbf{L^s}$ are *distinct*, while in regions of uniform flow, they are similar. This point will be of significance in the later discussion of turbulence fields. Furthermore, since Λ is relatively small in this case, L_x^s no longer identifies the larger structure, which has a lengthscale larger than Λ. This shows the importance of the choice of Λ in identifying larger or smaller symmetries and anti-symmetries of vector fields. We shall also discuss the effect of Λ in the context of turbulence in Sec. VI C.

Figure 5(d) shows G_x, i.e., the vorticity field equivalent of L_x. For $\Lambda = 250$, G_x has a shape similar to ω_z, but with a change in sign of the peak values (since the integral of ω_z happens to be negative in the current example). High values of the correlation are found corresponding to the vortex cores, the only regions where ω_z is large and uniform.

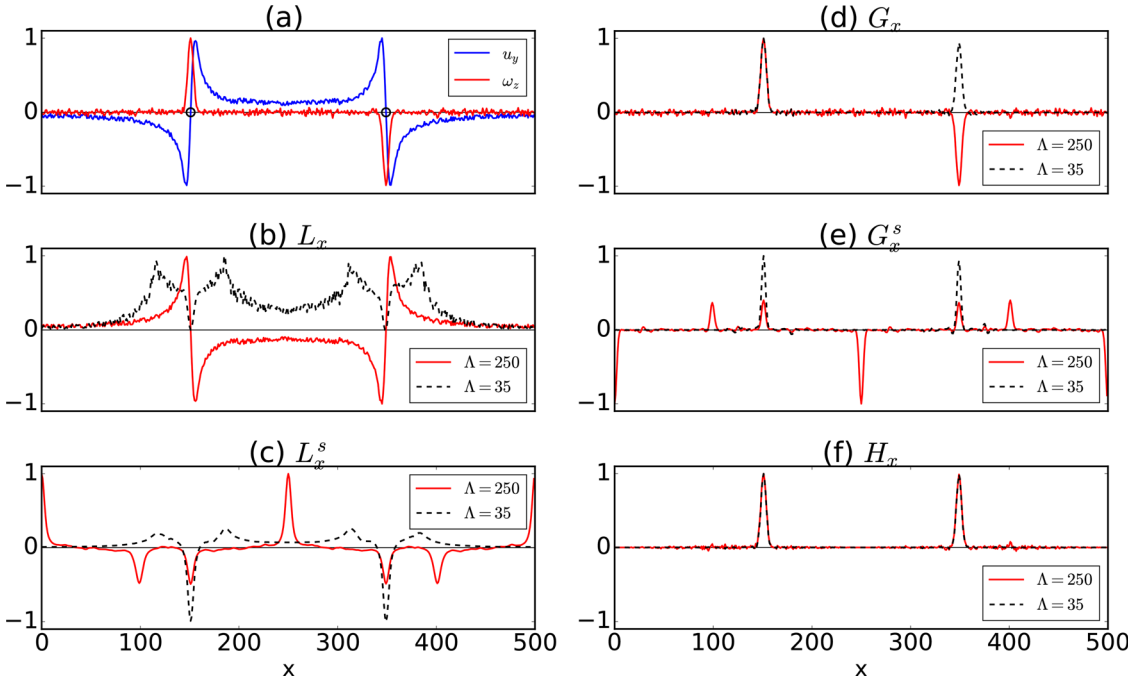

FIG. 5. (a) A one-dimensional velocity field comprising a larger structure composed of two smaller sub-structures (i.e., two counter-rotating Oseen vortices, with their centers marked with circles). Correlations calculated for this field are shown in panels (b) L_x, (c) L_x^s, (d) G_x, (e) G_x^s, and (f) H_x, for integration lengths of $\Lambda = 250$ and $\Lambda = 35$. Each field ψ is normalized by $|\psi|_{\max}$, to make the quantities comparable.

For $\Lambda = 35$, G_x retains the same relative shape of the peaks at the vortex cores, where the vorticity is high and symmetric, while both peaks are now positive.

G_x^s correlation in Fig. 5(e) has a very similar behavior to L_x^s. It yields a large negative peak at the middle of the larger structure, associated with the anti-symmetry of the vorticity around this point (while L_x^s has a large positive peak, associated with the symmetry of the velocity field). It also shows smaller positive peaks at the core of the vortices ($x = 150$ and $x = 350$), around which the vorticity is high and symmetric (while L_x^s has a negative peak, associated the anti-symmetry of the velocity field around the vortex cores). The G_x^s profile is also repeated due to the periodicity of the velocity field and the large integration length, similarly to the L_x^s profile in Fig. 5(c). For $\Lambda = 35$, G_x^s has a sharper profile at the vortex core (in comparison to G_x), since the vorticity values around the core are perfectly symmetric (apart from the noise values), and this *symmetry* decays faster with distance from the core than the vorticity itself.

Finally, Fig. 5(f) shows H_x, whose shape is found to be almost *insensitive* to the choice of Λ (while its magnitude increases with higher Λ). This can be understood from the construction of the correlation, which, in a Biot–Savart sense, is designed to identify regions where the angular velocity aligns with the vorticity. In this example, H_x yields large positive values in the core region of the two vortices, since the neighboring flow is generated by the vorticity at the cores. The independence of the choice of Λ is because the influence of the local vorticity at a point x_0 rapidly decays over distance such that at larger Λ values, the velocity field $u_y(x_0 \pm \Lambda)$ is not influenced by $\omega_z(x_0)$. The uniform flow between the two vortices in this example is induced by the sum of the individual vortex contributions and is, hence, "externally generated," which is why H_x remains zero in the middle of the two structures. The results, for a "linear" version of the H_x^p correlation (instead of its planar construction), are identical and are not additionally shown here.

Note that it is not only the length of integration Λ, but also the lower and upper limits of integration which determine the symmetries and structures being identified. For instance, Eq. (8) can be adapted to find non-local structures around $\mathbf{x}$ in the range $\Lambda_1 < r < \Lambda_2$. For example, the $\mathbf{L^s}$ correlation can be redefined as

$$L_i^s(\mathbf{x}, \Lambda_1, \Lambda_2) = \int_{r=\Lambda_1}^{\Lambda_2} \mathbf{u}(\mathbf{x} - r\mathbf{e}_i) \cdot \mathbf{u}(\mathbf{x} + r\mathbf{e}_i)\, \mathrm{d}r. \tag{27}$$

Figure 6 shows $\mathbf{L^s}$ with $\Lambda_1 = 75$ and $\Lambda_2 = 125$. These integration limits are such that, when x_0 corresponds to the middle of the larger structure in the velocity field (i.e., at $x = 250$), Λ_1 and Λ_2 span across most of the vortex regions. The L_x^s profile, consequently, shows a strong peak in between the two vortices, resulting from the larger structure comprising the two counter-rotating vortices. These particular limits of integration do not identify any significant larger symmetries, as observed from other x locations.

B. Two-dimensional Taylor–Green flow

We next test the correlations on a two-dimensional Taylor–Green flow field, which comprises a set of counter-rotating vortices. Interaction between vortex-pairs generates regions of the unidirection flow, separated by regions of swirling flow. A simplified

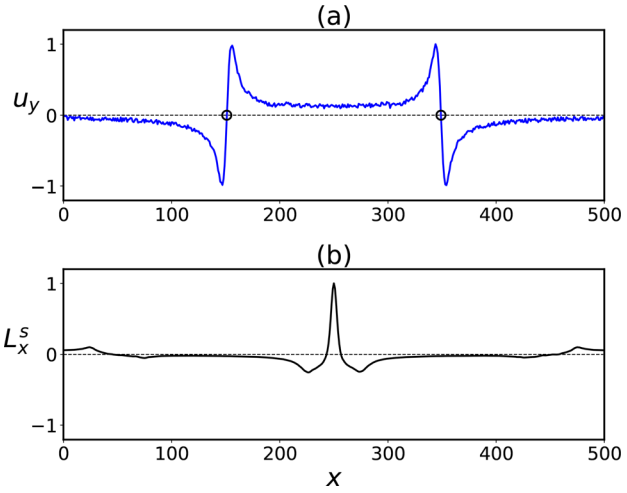

FIG. 6. (a) One-dimensional velocity profile, as shown in Fig. 5 and (b) L_x^s correlation integrated from $\Lambda_1 = 75$ to $\Lambda_2 = 125$ shows how non-local symmetries can be identified by varying the limits of integration.

Taylor–Green flow pattern can be generated by creating a velocity field as follows:

$$u_x(x, y) = \sin(x)\cos(y), \tag{28a}$$

$$u_y(x, y) = -\cos(x)\sin(y). \tag{28b}$$

We generate a velocity field within $\{x, y\} \in [0, 2\pi]$ (arbitrary units), adding uniform noise of amplitude 1% of $|\mathbf{u}|_{\max}$ (which is scaled to unity). The vorticity field, ω_z, is calculated using central differences. Figures 7(a) and 7(b) show kinetic energy (E_k) and vorticity (ω_z) with the flow streamlines, respectively, showing the counter-rotating vortices. The velocity field consists of structures which arise, reminiscent of the manner described by Hunt *et al.*,[4] as follows—(i) Eddies: four large vortices with core regions of high ω_z and low E_k, (ii) Streams: regions of well-aligned jet-like velocity, with high E_k and low ω_z, resulting from the interaction of large vortices, and (iii) convergent zone: a stagnation flow in the center with low E_k and low ω_z, also due to the interaction between the vortices.

The correlations, calculated for $\Lambda = \pi/2$, yield two-tuple fields (i.e., values along the x and y directions), except $\mathbf{H^p}$, which yields only a single valued field. Correlation magnitudes, normalized by the maximum (i.e., $|\boldsymbol{\psi}|/|\boldsymbol{\psi}|_{\max}$), are shown in Figs. 7(c)–7(h). Figure 7(c) shows $\mathbf{L}$, which has the highest magnitude in the streaming regions, which have both a high E_k and a high degree of local vector alignment. At the vortex core regions, $\mathbf{L}$ yields low values. It should be noted that for this velocity pattern, the regions of highest $\mathbf{L}$ are separated from regions of high vorticity.

Figure 7(d) shows $\mathbf{L^s}$, which has a very different structure than $\mathbf{L}$. Regions of highest $\mathbf{L^s}$ are found at the *vortex cores* (where $\mathbf{L}$ is low), around which there is anti-correlated swirling velocity. Furthermore, high $\mathbf{L^s}$ is also found in the streaming regions (like high $\mathbf{L}$), where the flow has a symmetry associated with jet-like, parallel streamlines. Regions of high $\mathbf{L^s}$ are separated by thin regions where $\mathbf{L^s}$ goes to zero, due to the larger symmetry in the velocity field. Note that there is also a region of high $\mathbf{L^s}$ coinciding with the stagnation flow region, due to the velocity anti-symmetry across the stagnation point.

Figure 7(e) shows **G**, which yields high values in the vortex core regions where the vorticity is uniform and high. In the regions of jet-like flow between vortex-pairs, **G** has values very close to zero, which is due to the negligible vorticity in these regions. Figure 7(f) shows $\mathbf{G}^{\mathbf{s}}$, which has a very different structure than **G**, since it identifies larger symmetries and anti-symmetries in the vorticity field. First, diffused regions of high $\mathbf{G}^{\mathbf{s}}$ are found corresponding to the vortex cores, similarly to **G** (but smaller in size), since the vorticity across the cores is symmetric. In between counter-rotating vortex-pairs, there appear slightly elongated regions of high $\mathbf{G}^{\mathbf{s}}$ due to the anti-symmetry of the vorticity along lines connecting the centers of counter-rotating vortex-pairs. Note that at the center, there exists also a strong symmetry in the vorticity field along *diagonals*; however, this is not reflected in $\mathbf{G}^{\mathbf{s}}$, which is constructed along the x and y directions where the vorticity is zero. This indicates that the particular alignment of the structures can lead to different values of the correlation, depending on the directions

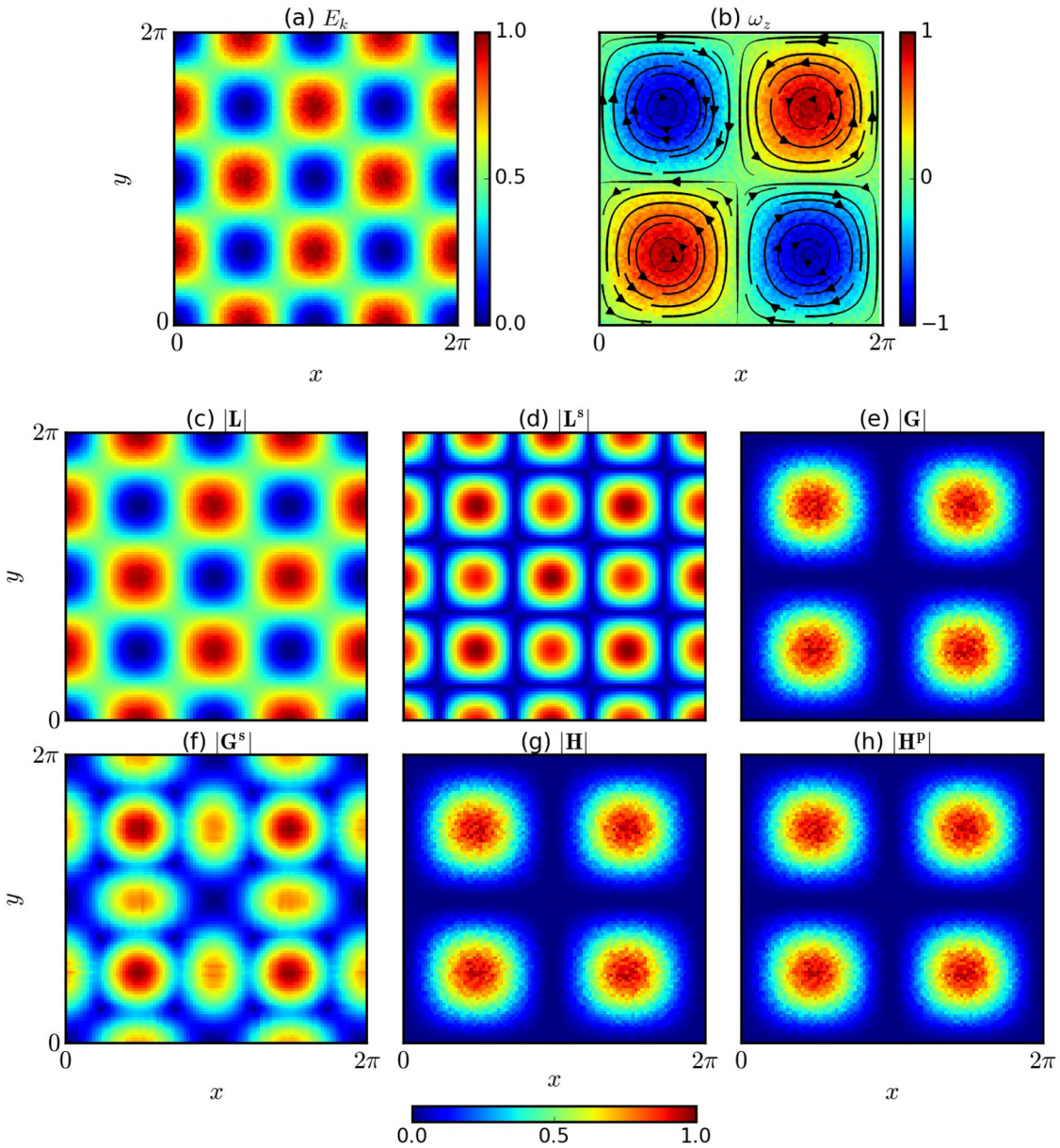

FIG. 7. A Taylor–Green velocity field. Panel (a) shows the kinetic energy E_k field and panel (b) the vorticity field ω_z, along with the flow streamlines (in black, with thickness varying with the velocity magnitude). Normalized correlation field amplitudes ($\psi/|\psi|_{\max}$), obtained upon integrating the correlations over $\Lambda = \pi/2$, are shown in (c) **L**, (d) $\mathbf{L}^{\mathbf{s}}$, (e) **G**, (f) $\mathbf{G}^{\mathbf{s}}$, (g) **H**, and (h) $\mathbf{H}^{\mathbf{p}}$.

chosen for calculating the correlations. However, in homogeneous isotropic turbulence, with an arbitrary distribution of structures, this effect will not appear in a statistical sense.

Finally, Figs. 7(g) and 7(h) show $\mathbf{H}$ and $\mathbf{H^p}$, respectively. Both correlations have a pattern that closely resembles $\mathbf{G}$, with large values at the vortex core regions, since the vortices are generated by strong vorticity values at the vortex cores. Regions of jet-like flow, which are *externally* induced by the interaction between the velocity fields of adjacent vortices, yield negligible values of $|\mathbf{H}|$ and $|\mathbf{H^p}|$.

C. Three-dimensional Burgers vortices

As a final canonical flows example, we now consider a three-dimensional velocity field generated by superposing Burgers vortices. Here, we mainly intend to test whether the correlations along a fixed bases can identify arbitrary aligned structures adequately. The Burgers vortex is an exact solution of the Navier–Stokes equation, consisting of a radial velocity component along with a tangential velocity, and can be constructed as

$$u_z = az, \tag{29a}$$

$$u_r = -\frac{ar}{2}, \tag{29b}$$

$$u_\theta = \frac{\Gamma}{2\pi r}\left[1 - \exp\left(-\frac{ar^2}{4\nu}\right)\right], \tag{29c}$$

where a represents the rate of strain, Γ is the circulation, and ν is the kinematic viscosity. Here, u_z, u_r, and u_θ give velocity components in the axial, radial, and tangential directions, which are converted from cylindrical to Cartesian coordinates. We limit the vortex in space to a spherical region by multiplying the velocity field with a three-dimensional Gaussian function $\mathcal{G}$,

$$\mathcal{G}(x, y, z) = \exp\left[-\left(\frac{x^2 + y^2 + z^2}{\sigma^2}\right)\right], \tag{30}$$

where x, y, and z are measured from the vortex core. This suppresses the strain regions generated by each vortex, far away from its center, such that the velocity field comprises primarily of two swirling vortices. The swirling-flow of the Burgers vortex resembles the one-dimensional Oseen vortex (as was described in Sec. V A). A low amplitude uniform noise, ζ, is added to the final velocity field. Finally, the vortices are also rotated at arbitrary azimuthal and elevation angles (α, β), to change the orientation of the velocity field symmetries with respect to the orthogonal bases along which the correlations are calculated.

We generate two vortices, on a grid of 100^3, with $a = 0.1$, $\nu = 0.025$, $\Gamma = 15$, and $\zeta = 0.004$ (i.e., $\sim$1% of the maximum velocity magnitude), all quantities being presented in arbitrary units, since we simply intend to generate a velocity field with a Burgers vortex *structure*. The resulting vortex has a core region with solid body rotation up to five units (grid cells) from its axis, and the velocity magnitude in the potential flow region (with swirling motion) decays to approximately 40% and 10% of the maximum velocity magnitude within 15 and 30 grid cells from the axis, respectively. Both vortices are multiplied with the Gaussian function $\mathcal{G}$, generated with $\sigma = 5$. The vortices are rotated at arbitrary azimuthal and elevation angles of $(0.6, 0.25)$ and $(-0.45, -0.3)$, measured in radians (while results were similar for several other random choices). These vortices are then superposed by adding their velocity fields, with their centers placed at (40, 40, 40) and (70, 70, 70). The resulting velocity field is shown in Fig. 8. Since the vortices are placed close to each other, their velocity fields begin to entangle and interact. The larger structure of the Burgers vortex-pair, however, is distinct from the Oseen vortex-pair in Sec. V A, and it does not have the same kind of symmetries and anti-symmetries. Figure 9 shows the amplitude of all the correlations, integrated over a length of $\Lambda = 12$, which is large enough to encompass most of the structure of each vortex (while results are qualitatively similar for $8 < \Lambda < 16$). The correlation fields have features that are analogous to the one-dimensional correlations of the Oseen vortex-pair (see Fig. 5). Figures 9(a) and 9(b) show that both $\mathbf{L}$ and $\mathbf{L^s}$ identify the swirling-flow region well, yielding high values where the streamlines are locally well-aligned and parallel. However, at the vortex cores $\mathbf{L^s}$ is large due to the anti-symmetry of the vortex, whereas $\mathbf{L}$ is zero due to the zero core velocity.

Panels (c) and (d) show the $\mathbf{G}$ and $\mathbf{G^s}$ correlations, both of which yield thin, elongated correlation profiles aligned with the axes of the vortices, while the $\mathbf{G^s}$ correlation is sharper. This again reflects that, at the core of the vortices, the vorticity vectors are well-aligned. Panels (e) and (f) show $\mathbf{H}$ and $\mathbf{H^p}$, which also yield strong correlation profiles at the cores, aligned with the vortices. This is because the swirling velocity field has a Biot–Savart relation with the vorticity at the vortex core regions.

Overall, the correlations are capable of identifying vortices that are arbitrary aligned. The exact values yielded, of course, would change upon rotating the correlation bases, but in a qualitative sense, this effect will not influence the results and conclusions.

D. Summary from canonical flows

The overall study using canonical vortex based flows shows that

1. **Vortex core** regions typically have high vorticity and low velocity. Here, $\mathbf{L^s}$ is high due to the velocity anti-symmetry of the swirling flow around the core, while $\mathbf{L}$ remains close to zero. These are invariably regions where $\mathbf{L^s}$ and $\mathbf{L}$ *do not* coincide. Vortex cores also yield high values of $\mathbf{G}$ and $\mathbf{G^s}$ since the

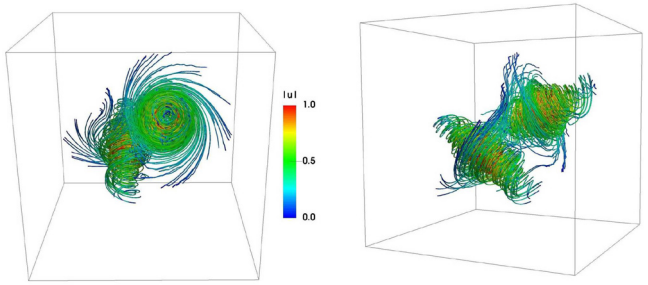

(a) View 1 (b) View 2

FIG. 8. Two arbitrary aligned Burgers vortices are shown, with isolated swirling-flow regions in (a) view 1 and (b) view 2 (isometric). The velocity streamlines are colored according to the velocity magnitude, normalized between 0 and 1, which show that the two vortices begin to "interact." The edges of the cubes shown here run from $\{x, y, z\} \in [10, 90]$.

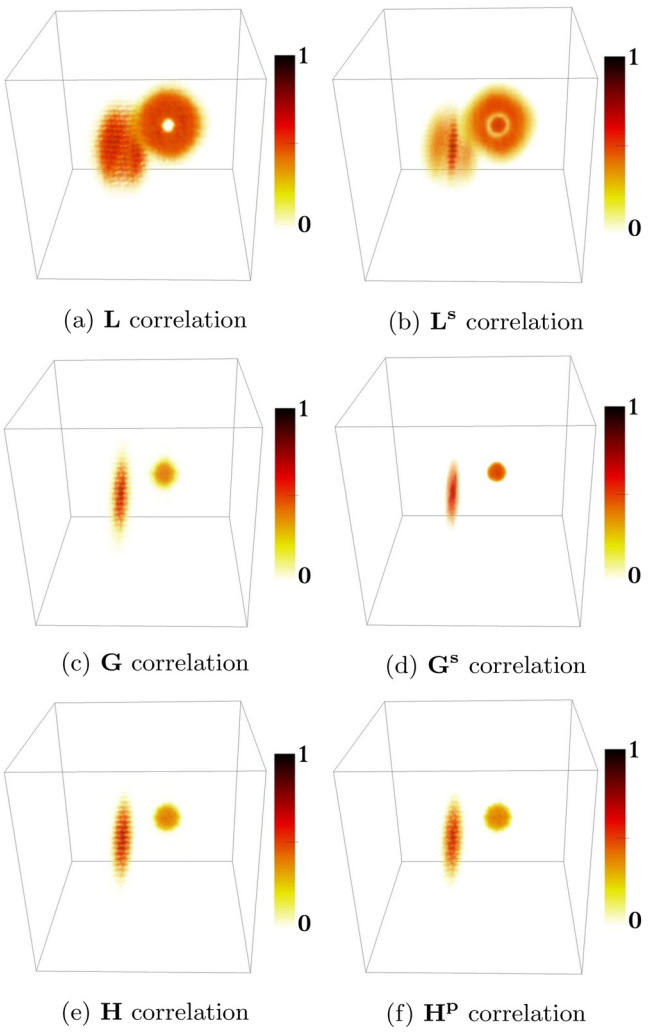

FIG. 9. Amplitude of all correlations calculated for the two Burgers vortices are shown for view 1 in Fig. 8, which gives a simultaneous look at the axis of one vortex and the core region of the other. All correlations are normalized as $\psi = |\psi|/|\psi|_{max}$. The edges of the cubes shown here run from $\{x, y, z\} \in [10, 90]$. The panels show (a) **L**, (b) $\mathbf{L^s}$, (c) **G**, (d) $\mathbf{G^s}$, (e) **H**, and (f) $\mathbf{H^p}$.

vorticity is aligned and symmetric, and high values of **H** and $\mathbf{H^p}$, since the swirling velocity is self-induced.

2. **Vortex swirl** regions, surrounding vortex cores, typically have high velocity and low vorticity. Here, **L** and $\mathbf{L^s}$ both yield high values, due to the aligned velocity streamlines, but do not coincide. Due to the low vorticity, **G**, $\mathbf{G^s}$, **H,** and $\mathbf{H^p}$ remain low.
3. **Streaming flow** regions can arise from the interaction of swirling vortices (as described in the literature[4]), which can have intermediate to high velocity and negligible vorticity. Here, **L** and $\mathbf{L^s}$ coincide and yield high values due to the aligned velocity field, while **G** and $\mathbf{G^s}$ remain low. Since these regions are *externally induced*, **H** and $\mathbf{H^p}$ are also low.
4. **Convergent flow** regions can arise from very specific vortex arrangements and may, hence, be an unlikely feature in turbulence fields. Here, both velocity and vorticity are close to zero, yielding low values of **L**, **G**, **H,** and $\mathbf{H^p}$. The larger symmetries around such regions, however, can give rise to high $\mathbf{L^s}$ and $\mathbf{G^s}$.

The coincidence and differences between the correlation fields are key to drawing conclusions on the nature of the coherent structures. We now apply these tools to turbulence fields, additionally bringing in a Biot–Savart based decomposition paradigm to further unravel how structures are organized. This allows us to examine how different turbulence fields are in comparison with purely vortex-based flows.

VI. CORRELATIONS APPLIED TO HOMOGENEOUS ISOTROPIC TURBULENCE

A turbulence velocity field is considered, typically, to have structures across multiple scales,[2] while the vorticity field mainly comprises structures at the smaller scales.[21,22] All these fields, however, are highly complex and irregular, while regions with a high degree of coherence are expected to yield large correlation values.

We begin with a brief description of the simulation method used to generate the turbulence data. Following which we describe how the correlation fields look qualitatively in comparison with the vector fields they are based on. We then describe the statistics of the correlation fields, their spectral characteristics, and their spatial organization. The Biot–Savart decomposition of structures is presented in Sec. VI A.

A. Simulation details and dataset

For this study, we use a dataset from DNS simulations of homogeneous isotropic turbulence, for which the Navier–Stokes equations with a body force **F** are solved numerically,

$$\frac{\partial \mathbf{u}}{\partial t} + (\mathbf{u}\cdot\nabla)\mathbf{u} = -\frac{\nabla p}{\rho} + \nu\nabla^2\mathbf{u} + \frac{\mathbf{F}}{\rho}, \tag{31}$$

$$\nabla\cdot\mathbf{u} = 0. \tag{32}$$

Turbulence is generated in a periodic box by means of low wavenumber forcing, which is divergence-free by construction and is concentrated over a range of Fourier modes. It is of the form given by Biferale *et al.*[41] and has properties similar to that devised by Alvelius[42] and Ten Cate *et al.*,[43] which can be written as

$$\begin{aligned} F_x &= \sum_{k=k_a}^{k_b} \rho A(k)\left[\sin\left(2\pi k y + \phi_y(k)\right) + \sin\left(2\pi k z + \phi_z(k)\right)\right], \\ F_y &= \sum_{k=k_a}^{k_b} \rho A(k)\left[\sin\left(2\pi k x + \phi_x(k)\right) + \sin\left(2\pi k z + \phi_z(k)\right)\right], \\ F_z &= \sum_{k=k_a}^{k_b} \rho A(k)\left[\sin\left(2\pi k x + \phi_x(k)\right) + \sin\left(2\pi k y + \phi_y(k)\right)\right]. \end{aligned} \tag{33}$$

The forcing is stochastic (white noise) in time, which is achieved by varying each $\phi(k)$ randomly, and the force is distributed over a small range of wavenumbers, given by $k_a \le k \le k_b$ (for this study we fix $k_a = 1, k_b = 8$), and the amplitude $A(k)$ of each of these wavenumbers is a Gaussian distribution in Fourier space, centered around a central forcing wavenumber k_f, given as

TABLE I. Simulation details, with all quantities presented in dimensionless lattice units [*lu*], average kinetic energy $\langle E_k \rangle = (\sum_k E(k))/N$, and the average rate of energy dissipation $\langle \epsilon \rangle = (\sum_k 2\nu k^2 E(k))/N$.

N^3	k_f	ν	u'	ω'	$\langle E_k \rangle$	$\langle \epsilon \rangle$	λ	$\mathcal{L}$	Re_λ	η	τ_k
256^3	2	0.004 7	0.034	0.010 3	1.8×10^{-3}	5.0×10^{-7}	13	128	95	0.67	97

$$A(k) = A \exp\left(-\frac{(k-k_f)^2}{c}\right), \tag{34}$$

where c sets the width of the distribution ($c = 1.25$ here), $k_f = 2$, and A is the forcing amplitude. We solve Eqs. (31) and (32) with a standard lattice-Boltzmann (LB) solver, incorporating the turbulence forcing as per Eq. (33). This method has been used before for simulating homogeneous isotropic turbulent flows of various kinds.[41,43–46]

The simulation is performed in a periodic box of size $(2\pi)^3$ resolved over N^3 grid points along each direction, all units being dimensionless, hence, resolving a range of wavenumbers from $k = 1$ (i.e., the largest scale has a length N [*lu*]) to $k = N/2$ (i.e., the smallest scale has a length 2 [*lu*]). Since we simulate homogeneous isotropic turbulence, by definition, all physical quantities are fluctuating and do not have a mean value, i.e., $\mathbf{u} = \mathbf{u}'$ and $\boldsymbol{\omega} = \boldsymbol{\omega}'$. The Kolmogorov scale is defined as $\eta \sim (\nu^3/\epsilon)^{1/4}$, where ν and ϵ are the kinematic viscosity and energy dissipation rate, respectively. We adhere to the criterion for a DNS, as given by Moin and Mahesh,[47] i.e., $k_{\max}\eta > 1$. The Taylor microscale is calculated as

$$\lambda = \left(\frac{15\nu u'^2}{\langle \epsilon \rangle}\right)^{1/2}, \tag{35}$$

where u' is the root mean square velocity. The average rate of energy dissipation $\langle \epsilon \rangle$ is calculated as $\langle \epsilon \rangle = \nu \langle \omega^2 \rangle$, where $\langle \omega^2 \rangle$ is the average enstrophy. Note that the enstrophy $\omega^2 = \boldsymbol{\omega} \cdot \boldsymbol{\omega}$ is analogous to the turbulence kinetic energy $E_k = \mathbf{u} \cdot \mathbf{u}/2$. For homogeneous isotropic turbulence, since $u' = v' = w'$, we have $E_k = 3u'^2/2$ or $u' = \sqrt{2E_k/3}$. The root mean square vorticity, ω', is obtained as $\langle \boldsymbol{\omega} \cdot \boldsymbol{\omega} \rangle^{1/2}$. In general, E_k and ϵ (apart from ν) are average measures of u' and ω', respectively.

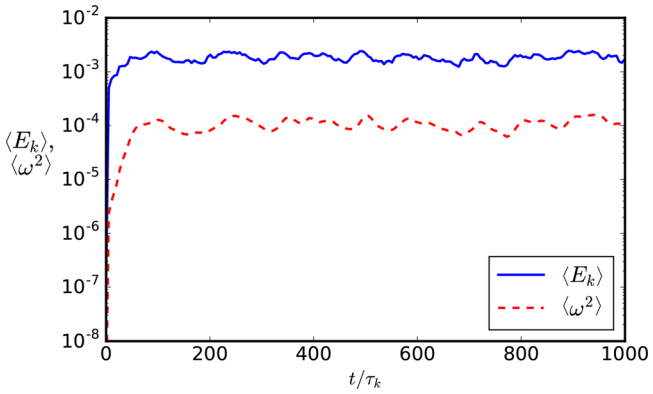

FIG. 10. Time evolution of the volume averaged turbulence kinetic energy $\langle E_k \rangle$ and enstrophy $\langle \omega^2 \rangle$. Both quantities attain a steady-state value, reflecting a developed turbulence state.

The large eddy turnover timescale is given as $T^\star = \mathcal{L}/u'$, where $\mathcal{L}$ is the forcing lengthscale, given as $\mathcal{L} = N/k_f$. Using λ, the Taylor Reynolds number is calculated as

$$Re_\lambda = \frac{u'\lambda}{\nu}, \tag{36}$$

and the Kolmogorov timescale is given as

$$\tau_k = \left(\frac{\epsilon}{\nu}\right)^{-1/2}. \tag{37}$$

The turbulence simulation (parameters given in Table I) is performed for a fluid initially at rest, to which the turbulence force is applied. After a brief transient duration, turbulence becomes well developed and attains a statistical steady-state, i.e., with a balance of power input and energy dissipation. The simulation is then run for several additional large eddy timescales ($\sim 20 - 30T^\star$), during which around $\sim$20 field snapshots are retained for analysis, all separated by $50\tau_k$, to give converged statistical results.

Figure 10 shows the evolution of $\langle E_k \rangle$ and $\langle \omega^2 \rangle$. Both quantities attain their steady-state values within a short transient phase, $\sim 100\tau_k$, after which they continue to oscillate around their temporal mean values. Beyond $100\tau_k$, turbulence is well developed, with a sufficient separation of scales. The small temporal oscillation of $\langle E_k \rangle$, due to the finite volume of the simulation, further manifests in the temporal oscillation of $\langle \omega^2 \rangle$, due to the turbulence dynamics.[41,48]

Figure 11 shows a snapshot of the turbulence kinetic energy E_k and enstrophy ω^2 fields, as 3D volume renderings and planar cross sections, at a simulation time of $500\tau_k$. Typical features of the kinetic energy and enstrophy can be seen, where the kinetic energy is

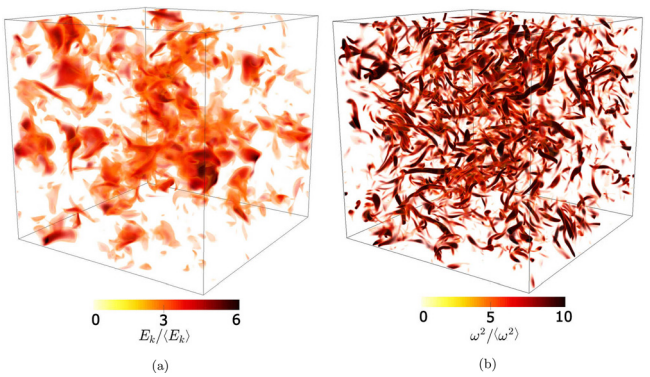

FIG. 11. Snapshots of fully developed turbulence fields (at $t = 500\tau_k$), show qualitative features of (a) kinetic energy E_k and (b) enstrophy, ω^2, as 3D volume renderings. (Note that field values have been clipped below the mid-way mark, to show only the high amplitude regions. Hence, regions with $E_k/\langle E_k \rangle < 3$ and $\omega/\langle \omega^2 \rangle < 5$ appear white.)

distributed over a range of length scales and forms diffused, small and intermediate sized, irregular structures. Enstrophy (and vorticity in general) is concentrated at the smaller scales, in spatially intermittent tube-like structures, also called "worms."

Figure 12 shows typical probability distributions (PDFs) of the velocity and vorticity. The velocity components follow a Gaussian distribution (shown as the dashed line), and their fluctuations are not extreme (here they range from $-4 < u_i/u_i' < 4$), and 65% and 97% of the velocity has a magnitude below u_i' and $2u_i'$, respectively. Extreme values of the velocity, around $|u_i| > 3u_i'$, occupy a very small fraction of the total volume. The vorticity components are highly non-Gaussian and exhibit typical long-tail distributions. The extent of these tails gives a measure of the intermittency in the vorticity field, where increasingly extreme values can occur with a low probabilities. Furthermore, 70% and 95% of the vorticity field have a magnitude below ω_i' and $2\omega_i'$, respectively.

We note that the vorticity field is often classified into a few "ranges." For our subsequent Biot–Savart analysis in Sec. VII D, where we disentangle the various vorticity contributions to the generation of velocity field structures, we use a classification similar to She *et al.*,[21,49] which is based upon the amplitude and structure of the vorticity-streamlines. Originally, She *et al.*[21,49] proposed

1. "High-vorticity" to represent the range $\omega \gg \omega'$, which occupies a very small fraction of the volume, forms vorticity-streamlines that are well-aligned, while the velocity field in the vicinity of these structures has a spiral, swirling motion.
2. "Moderate-vorticity" to represent the range $\omega > \omega'$, which had a less organized structure and was described as "sheet-like" and "ribbon-like," while the associated velocity streamline patterns were not discussed.
3. "Low-vorticity" represented the level of the root-mean-square vorticity, i.e., $\omega \sim \omega'$ and $\omega < \omega'$, which occupied most of the volume and was found to form random vorticity streamlines with no apparent structure.

Many studies have discussed the structure and behavior of the high vorticity worms. However, since it is vorticity at the level of ω', which occupies most of the volume, it is expected to have a significant contribution to the Biot–Savart velocity reconstruction. Hence, we term this range of vorticity, based upon its amplitude, as "weak" and "intermediate" *background vorticity*, since it permeates the volume. We use this classification only as a guideline to interpret our results.

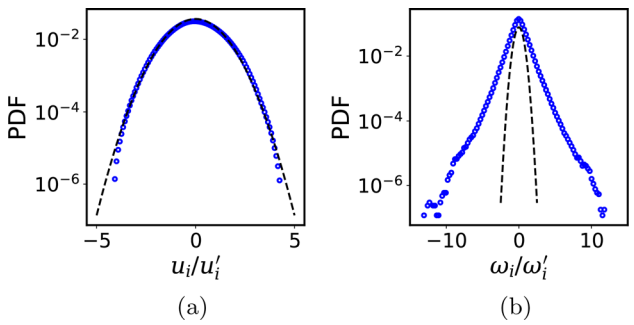

FIG. 12. Characteristic PDFs of the (a) velocity and (b) vorticity. The dashed lines show a typical Gaussian distributions.

B. Qualitative and statistical features of the correlation fields

Correlations are calculated for the snapshot of the data presented in Fig. 11, for an integration length of $\Lambda = \lambda$. Each correlation field, say $\mathbf{L}$, is normalized by its respective root mean square (rms) value, L', which is calculated as $L' = \langle \mathbf{L} \cdot \mathbf{L} \rangle^{1/2}$, where $\langle \cdot \rangle$ denotes volume averaging here, enabling comparison of field values to the instantaneous root mean square value. The amplitude of a correlation field, say $|\mathbf{L}|$, is simply referred to as L. The correlation fields are shown in Fig. 13. Figure 14 shows the PDFs of a single component (ψ_i) for each correlation $\boldsymbol{\psi}$, since, due to isotropy, the PDFs of ψ_x, ψ_y and ψ_z are

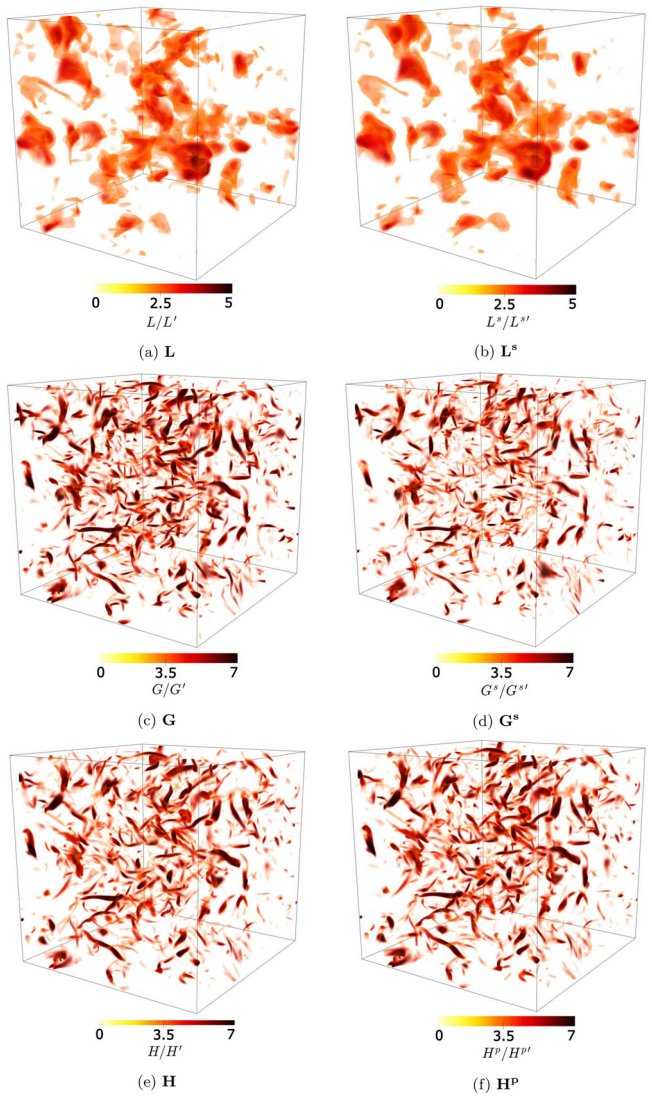

FIG. 13. Correlation field snapshots at $500\tau_k$ are shown as volume renderings with (a) $\mathbf{L}$, (b) $\mathbf{L^s}$, (c) $\mathbf{G}$, (d) $\mathbf{G^s}$, (e) $\mathbf{H}$, and (f) $\mathbf{H^p}$. Each correlation field is normalized with its respective root mean square value. (Field values below the mid-way mark are again clipped and appear white.)

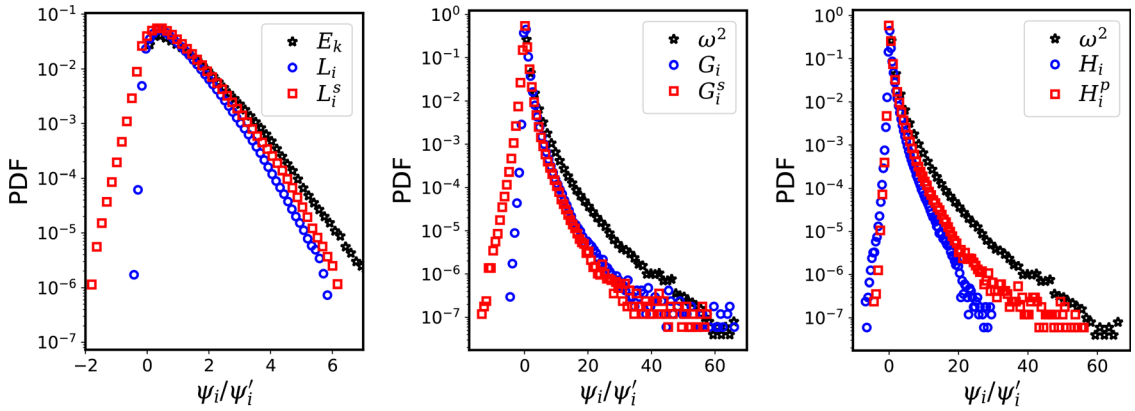

(a) E_k, **L** and $\mathbf{L^s}$ (b) ω^2, **G** and $\mathbf{G^s}$ (c) ω^2, **H** and $\mathbf{H^p}$

FIG. 14. PDFs of the correlation measures (a) **L** and $\mathbf{L^s}$, (b) **G** and $\mathbf{G^s}$, and (c) **H** and $\mathbf{H^p}$, shown for a single component ψ_i, due to statistical isotropy of the fields, together with the distributions of E_k and ω^2 normalized by their respective mean values.

identical.[50] Table II shows the correspondence between pairs of measures, calculated as the usual correlation coefficient,

$$r(f,g) = \frac{\sum_i (f_i - \bar{f})(g_i - \bar{g})}{\sqrt{\sum_i (f_i - \bar{f})^2 \sum_i (g_i - \bar{g})^2}}, \tag{38}$$

where f_i and g_i are field magnitudes at positions i and $\bar{f}$ and $\bar{g}$ denote means.

Figure 13(a) shows the **L** field, which exhibits features across various lengthscales, with diffused regions of high magnitude ranging from intermediate to small sizes. These features, furthermore, are very similar to the features in the E_k field (as seen in Fig. 11). Note that small, isolated, regions of the correlation field with typically a high magnitude, which we refer to as *correlation kernels*, are measures of the correlation in *larger regions* of the velocity and vorticity fields surrounding them (since these measures are non-local). The PDF of L_i in Fig. 14(a) shows that the correlation is highly positively skewed. This follows from the definition of **L**, which identifies regions of well-aligned streamlines, i.e., the local velocity $\mathbf{u}(\mathbf{x})$ is expected to be aligned with the velocity in the neighborhood $-\Lambda < x_i < \Lambda$, and the product of the two is positive. The strong coincidence of high L with regions of high E_k, with $r = 0.98$ (see Table II), where L is a non-local measure and E_k is a *point* quantity, reflects that high E_k regions comprise locally *jet-like* flows, with parallel streamlines exhibiting a high degree of alignment. Furthermore, similarly to u_i, the PDF of L_i does not extend over a very large range of values; however, it is strongly non-Gaussian. Approximately 70% and 93% of L_i is below L_i' and $2L_i'$, respectively.

TABLE II. Correlation $r(f, g)$ between the pairs of fields. Strong correlations are shown in boldface.

	L	L^s	G	G^s	H	H^p	E_k	ω^2
L	1	**0.98**	−0.001	0.032	−0.01	−0.01	**0.98**	0.005
L^s		1	−0.04	0.008	−0.05	−0.05	**0.94**	−0.03
G			1	**0.85**	**0.93**	**0.94**	0.02	**0.92**
G^s				1	**0.79**	**0.8**	0.07	**0.76**
H					1	**0.97**	0.01	**0.88**
H^p						1	0.01	**0.87**
E_k							1	0.03
ω^2								1

Figure 13(b) shows that the L^s field bears a striking similarity to the L field, with $r = 0.98$ (while some rare, high negative values of $\mathbf{L^s}$ are also found, that may not coincide with high L). The L^s field also has intermediate and small sized diffused regions, with a strong coincidence with high E_k. While the L^s kernels are slightly smaller than the L kernels, the strong overall correspondence between the two correlation fields is in stark contrast to the canonical vortical flows (where **L** and $\mathbf{L^s}$ do not coincide at vortex cores). This shows that most high values of L^s arise due to parallel streamlines, which further corroborates that high E_k structures from *compact* jet-like regions. Curiously, from a spectral perspective, most of the energy is concentrated at the large forcing scale, but this does not seem to have a physical-space analogue of equally large high E_k structures. The spectral signature comes from the distribution of these jets in the physical space. Note that Hunt, Wray, and Moin[4] also qualitatively described jet-like flow *streams*, however, there are several differences—they proposed that streams occur *between* interacting canonical vortices (as in the Taylor–Green flow example, Sec. V) and have *lower* velocities than the eddies themselves. While these might arise, the jet-like flow associated with L and L^s is distinct in that they have the *highest* kinetic energy, and moreover, as will be shown in the subsequent sections, they are generated by vorticity that does not have a very distinct structure or a high amplitude. The distribution of L_i^s in Fig. 14(a) is highly positively skewed. Large positive values of $\mathbf{L^s}$ reflect parallel streamlines, while high negative values of L^s are also found (possibly associated with low E_k, high ω^2 swirling structures), albeit with low probabilities. Similarly to the L_i field, approximately 70% and 93% of the L_i^s field are below $L_i^{s'}$ and $2L_i^{s'}$, respectively.

Figure 13(c) shows the **G** field (the $\boldsymbol{\omega}$ equivalent of **L**). The distribution of G is found to closely resemble the ω^2 field (with $r = 0.89$),

where the G field at high magnitudes also forms worm-like structures. High values of $\mathbf{G}$ indicate regions, which have both high vorticity and a high degree of alignment of the vorticity-streamlines. These aligned regions of high vorticity have been qualitatively described before,[19–21] to also have a local jet-like structure (which have also been referred to as *vortex-tubes,*[49] while in general, vortex tubes can also be irregular). The distribution of G_i in Fig. 14(b) is long-tailed and positively skewed, further reaffirming that high ω^2 regions are neighborhoods of a high degree of alignment of the vorticity-streamlines. Approximately 84% and 94% of the G_i fields are below G_i' and $2G_i'$, respectively, showing that most of the vorticity field does not have a simple, well-organized jet-like structure, which is limited only to the high $\mathbf{G}$ regions.

Figure 13(d) shows the $\mathbf{G^s}$ field (i.e., the $\boldsymbol{\omega}$ equivalent of $\mathbf{L^s}$), which appears "patchy" in comparison with $\mathbf{G}$, and its kernels are found to be more sparse and fragmented, since $\mathbf{G^s}$ is more sensitive to changes in the symmetries of $\boldsymbol{\omega}$. Visually, we find that there are no high amplitude G^s regions that do not coincide with high amplitude G. The distribution of G_i^s in Fig. 14(b) is also positively skewed, showing that the only symmetry of high valued $\boldsymbol{\omega}$ is parallel vorticity-streamlines. Negative values of G_i^s are slightly more prevalent than negative values of G_i, but are limited to the low amplitudes, showing the presence of some weak, more complex symmetries.

Figure 13(e) shows the $\mathbf{H}$ field, which relates the local vorticity $\boldsymbol{\omega}(\mathbf{x})$ to the velocity field along directions r_i. Similarly to the G and G^s fields, the H field also closely resembles the enstrophy field in Fig. 11 (with $r = 0.88$). The distribution of H_i in Fig. 14(c) is also positively skewed and long-tailed. Together, these results show that the velocity field in the vicinity of strong vorticity regions has an angular velocity closely positively aligned with the local vorticity streamlines. This is because (i) there exists a strong spatial correspondence between the occurrence of strong enstrophy regions and high magnitude $\mathbf{H}$, and (ii) the distributions of H_i dominantly show positive values, which means that the local flow, in the Λ-neighborhood, has an angular velocity well correlated with the vorticity. Approximately 82%, 94%, and 99% of H_i are below H_i', $2H_i'$, and $3H_i'$, respectively.

Finally, Fig. 13(f) shows the $\mathbf{H^p}$ field, which, similarly to the G, G^s, and H fields, also closely resembles the enstrophy field ($r = 0.87$). Similarly to H_i, the distribution of H_i^p in Fig. 14(c) is highly positively skewed and long-tailed, with slightly more extreme values than H_i.

Note that we verified for Gaussian random velocity fields that all correlation PDFs are perfectly symmetric, showing that the skewness observed here is due to the nature of the physical fields and not introduced by the correlation measures. The similarity between H^p and H, together with the other results, shows that the high ω^2 *invariably* forms small regions of aligned vorticity surrounded by *velocity-swirls* in the neighboring region. Finally, approximately 86%, 94%, and 97% of the H_i^p fields are within $H_i^{p'}$, $2H_i^{p'}$, and $3H_i^{p'}$, respectively, which are values similar to the relative levels of the H_i fields.

In summary, we note that coincidence between different correlation measures reflects a certain *simplicity* in the underlying turbulence fields for, in principle, different measures can yield very different correlation profiles. For example, $\mathbf{G}$, $\mathbf{G^s}$, $\mathbf{H}$, and $\mathbf{H^p}$ need not coincide in general, i.e., small-scale high vorticity-jets may not necessarily be surrounded by velocity-swirls (for instance when the local flow has a large externally induced component). Or, as shown in the canonical flow examples, $\mathbf{L}$ and $\mathbf{L^s}$ coincide in regions of uniform flow, whereas at vortex cores, $\mathbf{L^s}$ coincides with $\mathbf{H^p}$, while $\mathbf{L}$ remains negligible. In turbulence fields, hence, the overall correspondence between $\mathbf{L}$ with E_k and $\mathbf{L^s}$ shows that high E_k regions, locally, form highly aligned jet-like streamlines. Swirling regions of high E_k would lead to spatial differences in the distribution of $\mathbf{L}$ and $\mathbf{L^s}$, which we do not find. Similarly, the correspondence between $\mathbf{G}$, $\mathbf{G^s}$, $\mathbf{H}$, and $\mathbf{H^p}$ show that strong vorticity regions have highly aligned vorticity streamlines that are invariably associated with velocity-swirls in their surrounding regions.

Finally, the coincidence between $\mathbf{L}$ and E_k does not imply that one is the proxy for the other, since $\mathbf{L}$ is a *non-local* measure and E_k is a *point* quantity. The similarity occurs because (i) high E_k regions are composed of jet-like flow and (ii) the definition of $\mathbf{L}$ weighs in the local velocity magnitude. For instance, we find that $\hat{\mathbf{L}}$ (or equivalently $\hat{\mathbf{G}}$ for vorticity), operating on the *locally* normalized velocity field $\hat{\mathbf{u}}(\mathbf{x})$, indeed yields very different patterns in comparison to $\mathbf{L}$ and E_k (or $\mathbf{G}$ and ω^2), but a full exposition of these additional measures and their fields is beyond the scope of this work.

We also applied these correlations to a reference dataset obtained from the Johns Hopkins Turbulence Databases (JHTD),[51,52] and the results were found to be essentially similar to those presented here.[50]

C. Influence of the choice of Λ

Before further analysis of the correlation fields, it is important to consider the influence of Λ on the results. The obvious values of Λ that can be disregarded are those extremely small or large. Too small a Λ is somewhat meaningless, since we intend to capture non-local structures which have a *finite* physical size. On the other hand, very large values of Λ ($\sim N_x/2$) will introduce periodicity effects in the correlation fields, which should be avoided. However, there is a range of values of Λ in $0 \ll \Lambda \ll N_x/2$, which are viable. Here, we do not intend to study in detail the influence of Λ on the correlation measures; instead, we would like to choose a value of Λ large enough to cover most structure sizes, while ensuring that the results do not depend strongly on Λ.

The correlations $\mathbf{G}$ and $\mathbf{G^s}$ are not expected to vary significantly for different choices of Λ (once Λ is large enough to cover the size of these structures), since the structures in the vorticity field are small-scaled, and more or less randomly distributed throughout the volume. Similarly, the correlations $\mathbf{H}$ and $\mathbf{H^p}$ are expected to be even more insensitive to the choice of Λ, since the Biot–Savart influence of the vorticity decays with the square of the distance. We consider the $\mathbf{L}$ correlation, since it identifies intermediate sized structures in the velocity field and can potentially be influenced by the choice of Λ. $\mathbf{L}$ has the form

$$L_i(\mathbf{x}, \Lambda) = \int_{r=-\Lambda}^{\Lambda} \mathbf{u}(\mathbf{x}) \cdot \mathbf{u}(\mathbf{x} + r\mathbf{e}_i)\, \mathrm{d}r, \tag{39}$$

where $\mathbf{u}(\mathbf{x})$ can be placed outside the integral as

$$\begin{aligned} L_i(\mathbf{x}, \Lambda) &= \mathbf{u}(\mathbf{x}) \cdot \int_{r=-\Lambda}^{\Lambda} \mathbf{u}(\mathbf{x} + r\mathbf{e}_i)\, \mathrm{d}r, \\ L_i(\mathbf{x}, \Lambda) &= 2\Lambda(\mathbf{u}(\mathbf{x}) \cdot \widetilde{\mathbf{u}}_i), \end{aligned} \tag{40}$$

where

$$\widetilde{\mathbf{u}}_i = \frac{1}{2\Lambda} \int_{r=-\Lambda}^{\Lambda} \mathbf{u}(\mathbf{x} + r\mathbf{e}_i)\, \mathrm{d}r. \tag{41}$$

The $\mathbf{L}$ correlation is essentially the inner product of the velocity field $\mathbf{u}$ with the $\widetilde{\mathbf{u}}$ field (which is a function of Λ). Hence, if the $\widetilde{\mathbf{u}}$ field varies significantly with Λ, so will $\mathbf{L}$. In Fig. 15, snapshots of the $\widetilde{u}_z = |\widetilde{\mathbf{u}}_z|$ field are shown for a wide range of Λ/λ values, at a planar cross section of the volume. At very small values, $\Lambda/\lambda < 1$, the $\mathbf{L}$ field looks very similar to the E_k field, which is expected since the limit $\Lambda \to 0$ reduces $\mathbf{u} \cdot \widetilde{\mathbf{u}}$ to $\mathbf{u} \cdot \mathbf{u}$. The $\widetilde{u}_z$ field does not appear to change significantly for $1 \leq \Lambda/\lambda < 7$, which is also true for $\Lambda/\lambda \geq 7$, although those values of Λ begin to approach the size of the simulation domain and should be disregarded.

It is interesting that the $\widetilde{u}_z$ field appears to vary slowly for $\Lambda/\lambda > 1$. The variation of $\widetilde{\mathbf{u}}_i$ with Λ can be quantified by calculating

$$\left|\frac{\mathrm{d}\widetilde{\mathbf{u}}_i}{\mathrm{d}\Lambda}\right| = \frac{|\widetilde{\mathbf{u}}_i^{\Lambda+\Delta\Lambda} - \widetilde{\mathbf{u}}_i^{\Lambda}|}{\Delta\Lambda}, \tag{42}$$

where $|\cdot|$ is the amplitude of the difference between the two fields. This is shown in Fig. 16 for $\widetilde{\mathbf{u}}_x, \widetilde{\mathbf{u}}_y$, and $\widetilde{\mathbf{u}}_z$, where $\langle\cdot\rangle$ denotes spatial averaging over the entire volumetric domain, and over two independent realizations of $\widetilde{\mathbf{u}}_i$ at $t \approx 500\tau_k$ and $1000\tau_k$. The change in $\langle|\mathrm{d}\widetilde{\mathbf{u}}_i/\mathrm{d}\Lambda|\rangle$ is large for $\Lambda/\lambda < 1$. This reflects the fact that most of the velocity structures in the flow are smaller than the Taylor microscale λ, and they get averaged over in the $\widetilde{\mathbf{u}}$ fields for increasing Λ. Next, $\langle|\mathrm{d}\widetilde{\mathbf{u}}_i/\mathrm{d}\Lambda|\rangle$ seems to decay exponentially for $\Lambda/\lambda > 1$, with a slope of approximately $-1/5$. This change in behavior occurs via a sharp transition around $\Lambda/\lambda \approx 1$. Previous works have also reported sharp transitions around the Taylor lengthscale for different measurements like velocity profiles in shear layers in isotropic and wall-bounded turbulence.[37,53]

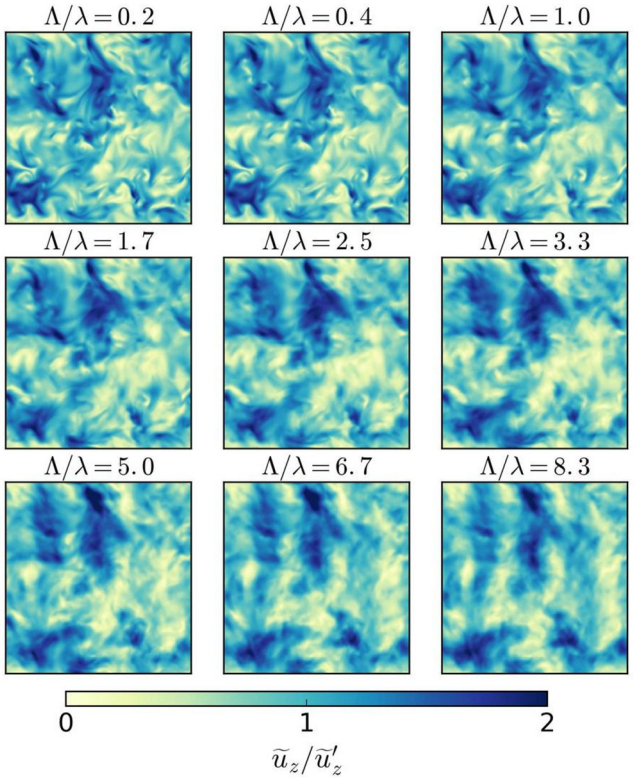

FIG. 15. Cross-sectional slices of the $\widetilde{u}_z$ field for varying Λ/λ.

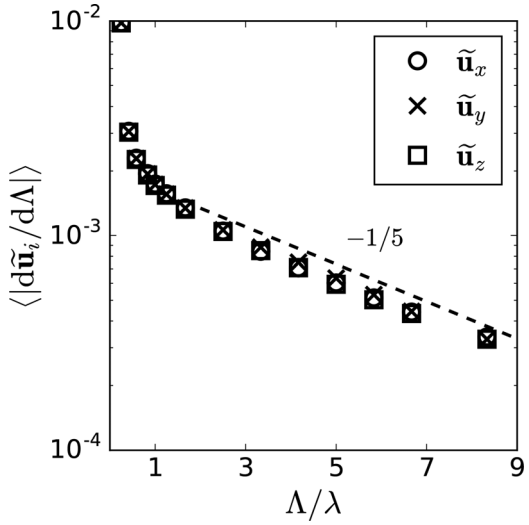

FIG. 16. Rate of change in the $\widetilde{\mathbf{u}}_i$ fields with an increase in Λ. Here, $\langle\cdot\rangle$ denotes spatial averaging.

The behavior of $\langle|\mathrm{d}\widetilde{\mathbf{u}}_i/\mathrm{d}\Lambda|\rangle$ shown in Fig. 16 indicates that for large Λ/λ, i.e., in the limit of $\Lambda \to \infty$: (i) $\mathrm{d}\widetilde{\mathbf{u}}_i/\mathrm{d}\Lambda \to 0$, (ii) $\widetilde{\mathbf{u}}_i \to 0$, (iii) $\mathrm{d}\mathbf{L}/\mathrm{d}\Lambda \to 0$, and (iv) $\mathbf{L}$ goes to a constant. This is consistent with Eq. (21) and the requirement that there should not exist "an organized motion over an infinite distance." Also, Fig. 16 shows that $\widetilde{\mathbf{u}}_i$ varies slowly for $\Lambda/\lambda > 1$ and suggests that $\Lambda|\widetilde{\mathbf{u}}_i|$ attains a maximum, roughly, in the range $1 \leq \Lambda/\lambda \leq 4$; hence, the results for $\mathbf{L}$ and $\mathbf{L}^{\mathbf{s}}$ are not expected to vary significantly in this range of Λ. This, together with the sharp transition around $\Lambda/\lambda \approx 1$, suggests that the Taylor microscale λ is a good measure to account for dominant structure sizes, as also found in earlier work,[37] and, hence, can be taken as a reasonable yardstick for the integration length of the correlations. For the remainder of this study, we use correlation fields calculated for $\Lambda = \lambda$. This value is also large enough to account for vorticity field structures and vorticity–velocity (i.e., Biot–Savart related) field structures.

In general, the variation with Λ can be considered for $\mathbf{G}$ by constructing $\widetilde{\omega}_i$ fields, $\mathbf{H}$ by replacing $\mathbf{u}(\mathbf{x})$ with $\boldsymbol{\omega}(\mathbf{x}) \times \mathbf{r}_i$ in Eq. (39) and $\mathbf{H}^{\mathbf{p}}$ by constructing area-averaged $\widetilde{u}_i$ fields. Such a study, performed on a larger dataset, can be interesting, but we do not pursue it here. For the remainder of this study, we calculate correlation fields with $\Lambda = \lambda$, which seems to be a suitable choice for $\mathbf{L}$, and hence also for $\mathbf{L}^{\mathbf{s}}$, due to their strong similarly. Furthermore, strong vorticity structures are also typically smaller than λ, making $\Lambda = \lambda$ a suitable choice also for the vorticity-based correlation measures, as we do not investigate structures associated with mild-vorticity in this study. Furthermore, here onward we only consider: (i) $\mathbf{L}$, due to the lack of larger velocity-anti-symmetries as shown by the coincide between $\mathbf{L}$ and $\mathbf{L}^{\mathbf{s}}$ and (ii) $\mathbf{H}^{\mathbf{p}}$, due to the fact that strong vorticity is invariably surrounded by velocity-swirls and the lack of significant vorticity-anti-symmetries, as shown by the coincidence between $\mathbf{H}^{\mathbf{p}}$, $\mathbf{H}$, $\mathbf{G}$, and $\mathbf{G}^{\mathbf{s}}$. Again, in other kinds of flow, this need not be the case.

D. Spectral characteristics of the correlation fields

The spectra of the three-dimensional correlation fields are shown in Fig. 17, in comparison with the kinetic energy (E_k) and enstrophy (ω^2) spectra. The correlation spectra are calculated in the same way as the E_k spectra, where the three-dimensional Fourier transforms $\hat{\phi}(\mathbf{k})$ of the correlation fields ϕ are squared and spherically averaged over wavenumber shells $k = \sqrt{\mathbf{k} \cdot \mathbf{k}}$. The spectra have also been time-averaged over 20 realizations, each separated by $50\tau_k$. Figures 17(a) and 17(b) show the **L** and $\mathbf{L}^s$ spectrum, respectively, that are found to have very similar shapes. This reflects that the spatial distribution of the $\mathbf{L}^s$ field is very similar to that of the **L** field, reaffirming that there are no large symmetries or anti-symmetries in the velocity field. The spectra, in comparison with the E_k spectrum, have a shift in the peak to higher wavenumbers. This is because **L** and $\mathbf{L}^s$ involve a product of the velocity field. Moreover, the correlation fields comprise relatively *smaller* correlation kernels associated with larger flow structures.

The spectra of **G** and $\mathbf{G}^s$ in Figs. 17(c) and 17(d), respectively, are found to closely resemble the enstrophy spectrum, with a slight shift in the spectral peak to higher wavenumbers for both cases, which is again due to the correlation kernels being relatively smaller than the vorticity field structures, and the product involved the correlation definitions.

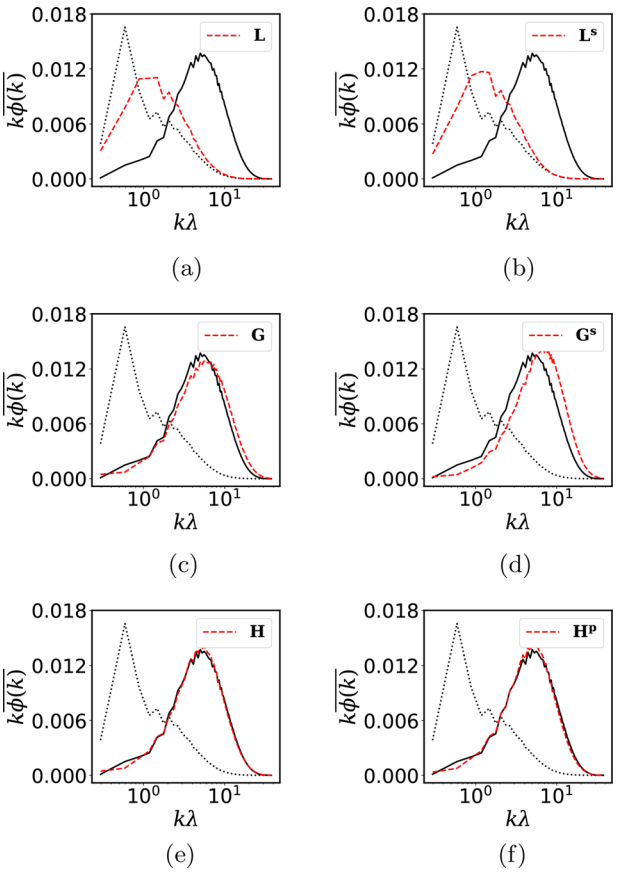

FIG. 17. Time-averaged premultiplied spectra of correlation fields (a) **L**, (b) $\mathbf{L}^s$, (c) **G**, (d) $\mathbf{G}^s$, (e) **H**, and (f) $\mathbf{H}^p$ shown together with the kinetic energy (E_k, dotted black line, "· · ·") and enstrophy (ω^2, solid black line "—") premultiplied spectra.

This shift is more pronounced in the $\mathbf{G}^s$ spectrum, which is consistent with the fact that the $\mathbf{G}^s$ field has sharper features, as can be seen in both Fig. 13(d) (volume rendered $\mathbf{G}^s$ field snapshot) and Fig. 5(e) (one-dimensional Oseen vortex-pair example).

The **H** and $\mathbf{H}^p$ spectra in Figs. 17(e) and 17(f), respectively, are found to have a striking similarity to the enstrophy spectrum. This reflects that the spatial variation of enstrophy consistently yields a similar spatial variation in the **H** and $\mathbf{H}^p$ fields. This also indicates that the "energy containing" wavelengths of the velocity field do not have any significant self-induced swirl, showing that the swirling flow structures are coupled with the vorticity structures, and decoupled from the strong velocity structures.

We find that the nature of (homogeneous isotropic) turbulence fields is such that there is, largely, a correspondence between **L** and $\mathbf{L}^s$. It is important to note that this need not be the case in general, as was clear from the canonical flows example. This reflects an underlying simplicity in the turbulence fields, which seem to lack regions with high E_k that have larger symmetries (high energy vortices), which would form regions where **L** and $\mathbf{L}^s$ differ. Similarly, **G**, $\mathbf{G}^s$, **H**, and $\mathbf{H}^p$ also coincide, while this may not be true in general either. For instance, in a situation where there is a uniform flow superposed on the turbulence velocity field, a local swirling region will be overwhelmed and appear as a velocity-jet, yielding high values of **L** and $\mathbf{L}^s$, while also yielding high values of **G** and $\mathbf{G}^s$ since the vorticity field will not reflect the uniform flow. **H** and $\mathbf{H}^p$, however, will remain low, since the local velocity is largely *externally induced* in this case. The various correlations, hence, form a *general* set of tools for a variety of flow situations, and correspondence between them is *also* indicative of the nature of the fields.

With the above considerations in mind, for the remainder of this study, we shall use only **L** and $\mathbf{H}^p$ correlations to refer to turbulence structures, for practical reasons.

E. Spatial distribution of correlation fields

Since the kernels of L and H^p identify distinct streamline patterns, the relative spatial distribution of these kernels sheds light on the distribution of coherent structures in physical space. Here, we discuss the spatial distribution statistics of L and H^p, in relation to E_k and ω. Figure 18(a) shows contours $2\langle E_k \rangle$ (in blue) together with contours of $3\omega'$. High E_k and high ω regions are found to be *spatially exclusive* to a large extent [with $r(E_k, \omega^2) = 0.03$]. The exclusivity between the two quantities might be a consequence of the dynamical separation between them, as high E_k and high ω are influenced by different aspects of the Navier–Stokes dynamics.[1] The two fields also begin to overlap when the thresholds are lowered and become more exclusive and distanced at higher thresholds. Figure 18(b) shows the distribution of $2L'$ (in blue) and $5H^{p\prime}$ (in red). The correlation kernels also remain spatially exclusive [with $r(L, H^p) = -0.01$], increasingly at higher threshold levels. The sizes of these kernels, in principle, can be related to the sizes of the underlying flow structures. The distribution of structure sizes, in principle, could be related to the distribution of kernel sizes.

Relative spatial distribution can be quantified with the joint-PDFs of pairs of variables. Figure 19 shows these distributions, using samples from over 20 field realizations. Figure 19(a) shows the joint-PDF of L and E_k. Since the two fields coincide strongly, they are highly correlated. Generally, large values of E_k also yield large values of L.

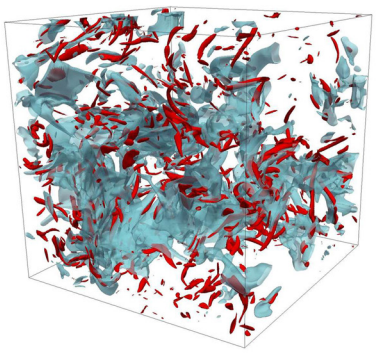

(a) Contours of $E_k = 2\langle E_k \rangle$ (blue) along with $\omega = 3\omega'$ (red) shows that these fields are spatially exclusive.

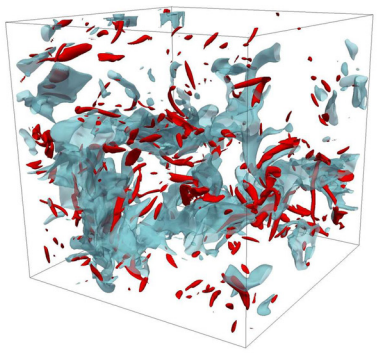

(b) Contours of $L = 2L'$ (blue) along with $H^p = 5H^{p'}$ (red) shows that these correlation fields are spatially exclusive.

FIG. 18. Spatial distribution of fields. Panel (a) shows contours of E_k and ω, and panel (b) shows contours of L and H^p, at the same time instant. (a) Contours of $E_k = 2\langle E_k \rangle$ (blue) along with $\omega = 3\omega'$ (red) shows that these fields are spatially exclusive. (b) Contours of $L = 2L'$ (blue) along with $H^p = 5H^{p'}$ (red) shows that these correlation fields are spatially exclusive.

This shows that all regions of high E_k comprise well-aligned streamlines, and there are no regions of high E_k with disordered velocity vectors.

Figure 19(b) shows that the H^p and ω fields are again strongly correlated, while the probability of occurrence of large-valued H^p is higher than large-valued ω. Higher values of ω are invariably associated with high H^p values, which shows that the flow around high ω regions always has a swirling motion.

The distribution of E_k and ω is shown in Fig. 19(c). The two quantities reflect intermediate sized, kinetic energy containing

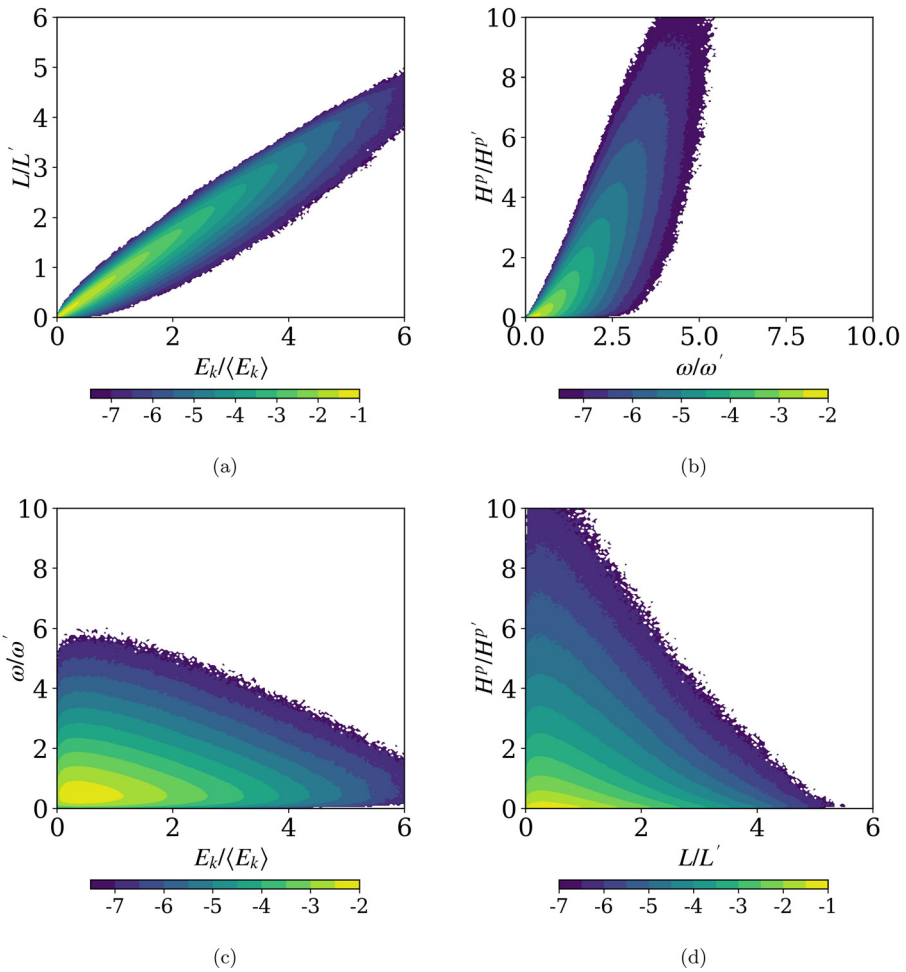

FIG. 19. Joint-PDFs of (a)L and E_k, (b) H^p and ω, (c) ω and E_k, and (d) H^p and L. The colors show logarithmically spaced values.

structures, and small-scale, high vorticity structures, respectively. The joint-PDF shows that high values of the two quantities are anti-correlated in space, i.e., the fields are mutually exclusive. For instance, the probability of finding a high E_k region, which also has a high ω value, is negligible. In principle, this situation is not forbidden and could arise for instance in a region of high swirl, where high uniform velocity is externally imposed, however, in isotropic turbulence, such coincidence does not arise. A similar anti-correlated distribution is found for H^p and L, in Fig. 19(d). High values of H^p coincide with regions of low L. This, together with the strong correlation between L and E_k in Fig. 19(a), shows that swirling-flow regions do not correspond with high kinetic energy structures and vice versa. This is consistent with the similarity between $\mathbf{L}$ and $\mathbf{L}^s$, since swirling-flow structures with high kinetic energy would be associated with large values of L^s.

To quantify the volume fraction and degree of spatial overlap between different fields, we construct the joint-CDFs, which are functions of the integration limits α_1, α_2, β_1, and β_2, on the joint-PDF of the fields f_1 and f_2. This is defined as a generalization of the one-dimensional CDF (see, for instance, Pope[54]) as

$$\mathrm{CDF}(f_1,f_2;\alpha_1,\alpha_2,\beta_1,\beta_2)=\int_{\beta_1}^{\beta_2}\left[\int_{\alpha_1}^{\alpha_2}\mathrm{PDF}(f_1,f_2)df_1\right]df_2\,. \tag{43}$$

The CDF can directly be interpreted, in a statistical sense, as the volume fraction of the region defined by the integration limits as follows:

$$\mathrm{CDF}(f_1,f_2;\alpha_1,\alpha_2,\beta_1,\beta_2)=\frac{V\{(\alpha_1\le f_1\le\alpha_2)\cap(\beta_1\le f_2\le\beta_2)\}}{V_t}, \tag{44}$$

where V is the intersection volume between regions where the conditions $\alpha_1\le f_1\le\alpha_2$ and $\beta_1\le f_2\le\beta_2$ are both met, while V_t is the total volume. The volume fraction of a single field, within prescribed threshold limits, can also be statistically quantified with the CDF as follows:

$$\mathrm{CDF}(f_1,f_2;\alpha_1,\alpha_2,0,\infty)=\frac{V(\alpha_1\le f_1\le\alpha_2)}{V_t}. \tag{45}$$

This is because the region $0\le f_2\le\infty$ corresponds to the total volume V_t, hence $V\{(\alpha_1\le f_1\le\alpha_2)\cap V_t\}\equiv V(\alpha_1\le f_1\le\alpha_2)$. The CDF can be used to evaluate the degree of spatial inclusivity between fields, $R(\widetilde{f}_1,\widetilde{f}_2)$, which can be defined as

$$R(\widetilde{f}_1,\widetilde{f}_2)=\frac{\mathrm{CDF}(f_1,f_2;\alpha_1,\alpha_2,\beta_1,\beta_2)}{\mathrm{CDF}(f_1,f_2;\alpha_1,\alpha_2,0,\infty)}, \tag{46}$$

where $\widetilde{f}_1$ and $\widetilde{f}_2$ are conditionally sampled f_1 and f_2 fields, i.e., the region $\widetilde{f}_1\equiv\alpha_1\le f_1\le\alpha_2$ and the region $\widetilde{f}_2\equiv\beta_1\le f_2\le\beta_2$. The numerator on the right hand side gives the volume fraction of the intersection region $\widetilde{f}_1\cap\widetilde{f}_2$, while the denominator gives the volume fraction of $\widetilde{f}_1$. Hence, the fraction denotes the degree of inclusivity of the region $\widetilde{f}_1$ in the region $\widetilde{f}_2$. Conversely, $R(\widetilde{f}_2,\widetilde{f}_1)$ gives the inclusivity of $\widetilde{f}_2$ in $\widetilde{f}_1$.

Figure 20(a) shows the inclusivity of the fields L and E_k, i.e., $R(\widetilde{L},\widetilde{E}_k)$ and $R(\widetilde{E}_k,\widetilde{L})$. The regions $\widetilde{L}\equiv L^t\le L\le\infty$ and $\widetilde{E}_k\equiv E_k^t\le E_k\le\infty$, where the thresholds L^t and E_k^t are values of L' and $\langle E_k\rangle$. The L field is found to remain completely enclosed within the corresponding E_k regions, since $R(\widetilde{L},\widetilde{E}_k)=1$. This can be understood from the fact that highly organized velocity with a high amplitude yields high L values, albeit, the kernels of the L correlation that are associated with a large region of velocity organization are themselves (relatively) smaller. This becomes more pronounced at higher levels of the L and E_k fields, as higher L values reflect both high E_k and larger organization. Note that higher levels of L give a good indication of the flow organization and velocity magnitude, L and E_k are not directly comparable, since L is a non-local measure of structure while E_k is a point criterion. $R(\widetilde{E}_k,\widetilde{L})$ is found, conversely, to become successively smaller at higher threshold values, further reflecting that high E_k regions occupy larger spatial regions than high L. This is also reflected in the volume fractions V_f of L and E_k, calculated as $\mathrm{CDF}(L,E_k;L^t,\infty,0,\infty)$ and $\mathrm{CDF}(L,E_k;0,\infty,E_k^t,\infty)$, respectively, as shown in Fig. 20(c). At increasing threshold levels, the $L>L^t$ field occupies smaller volume fractions in comparison with $E_k>E_k^t$. Finally, the kinetic energy content of the thresholded L and E_k regions is shown in Fig. 20(e). Regions corresponding to $E_k\ge\langle E_k\rangle$, $E_k\ge2\langle E_k\rangle$, $E_k\ge3\langle E_k\rangle$ occupy 40%, 10%, and 2.5% of the total volume [panel (c)], respectively, and contain 70%, 30%, and 9% of the total kinetic energy. Similarly, regions corresponding to $L\ge L'$, $L\ge2L'$ and $L\ge3L'$ occupy 30%, 5%, and 0.7% of the total volume, while containing 55%, 15%, and 3% of the total kinetic energy.

Figure 20(b) shows the inclusivity of the fields H^p and ω, i.e., $R(\widetilde{H^p},\widetilde{\omega})$ and $R(\widetilde{\omega},\widetilde{H^p})$, where the regions are defined as $\widetilde{H^p}\equiv H^{pt}\le H^p\le\infty$ and $\widetilde{\omega}\equiv\omega^t\le\omega\le\infty$. The fraction of the H^p field contained inside ω regions increases at higher threshold values. This shows, first, that the H^p field occupies successively smaller spatial regions at higher thresholds. Second, high H^p values are invariably found *inside* high ω regions, reaffirming that strong vorticity is associated with surrounding regions of swirling motion. This can also be seen from Fig. 19(b), where the lower bound on the value of H^p increases with ω. At low threshold values, $R(\widetilde{H^p},\widetilde{\omega})$ is low, which shows that the H^p field at low values occupies more space in comparison with low ω. This is reflected in $R(\widetilde{\omega},\widetilde{H^p})$, which has high values at low ω. It is further confirmed in Fig. 20(d), which shows that $H^p\ge H^{p'}$ occupies 26% of the volume, while $\omega\ge\omega'$ occupies 17% of the volume. Furthermore, the volume fraction occupied by the H^p field decays much faster than ω, when thresholded at successively higher values. Finally, panel (f) shows that regions of $H^p\ge H^{p'}$, $H^p\ge3H^{p'}$ and $H^p\ge5H^{p'}$ contain 85%, 22%, and 3% of the total enstrophy.

Finally, Fig. 21(a) shows $R(\widetilde{\omega},\widetilde{H^p})$, the inclusivity of regions of high vorticity ($\widetilde{\omega}\equiv\omega^t\le\omega\le\infty$) with regions of low H^p ($\widetilde{H^p}\equiv0\le H^p\le H^{p'}$). For all instances of $\omega^t\ge\omega'$, the intersection volume of $\widetilde{\omega}$ with $\widetilde{H^p}$ goes to zero. This confirms that there are no high ω regions in the flow field that are not associated with swirling motion in their vicinity. Figure 21(b) shows the inclusivity of the L and H^p fields, i.e., $R(\widetilde{H^p},\widetilde{L})$ and $R(\widetilde{L},\widetilde{H^p})$, for increasing threshold values. $R(\widetilde{H^p},\widetilde{L})$ shows that the correlation kernels become increasingly *spatially exclusive* at higher threshold values, which can also be seen from the joint-PDFs in Fig. 19(d), where the L and H^p fields are anti-correlated. This reflects the spatial exclusivity of highly organized kinetic energy jets and vorticity induced swirls. Interestingly, $R(\widetilde{L},\widetilde{H^p})$ coincides with $R(\widetilde{H^p},\widetilde{L})$ for the first few threshold levels, showing that the volume fractions of L and

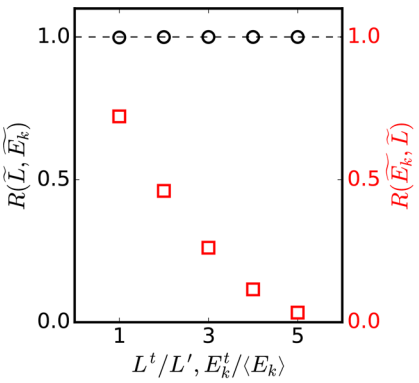

(a) Inclusivity of $\widetilde{L}$ and $\widetilde{E_k}$.

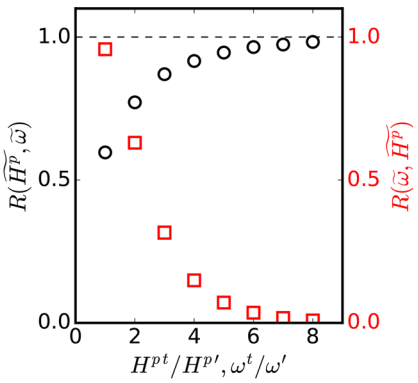

(b) Inclusivity of $\widetilde{\omega}$ and $\widetilde{H^p}$.

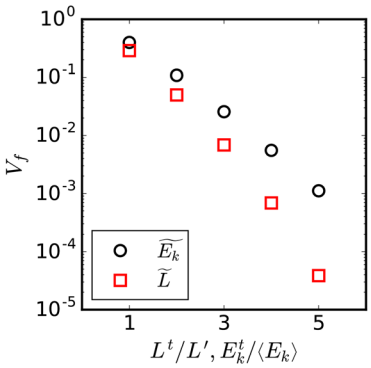

(c) Volume fraction V_f of $\widetilde{L}$ and $\widetilde{E_k}$.

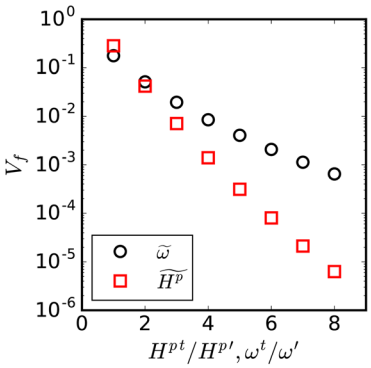

(d) Volume fraction V_f of $\widetilde{\omega}$ and $\widetilde{H^p}$.

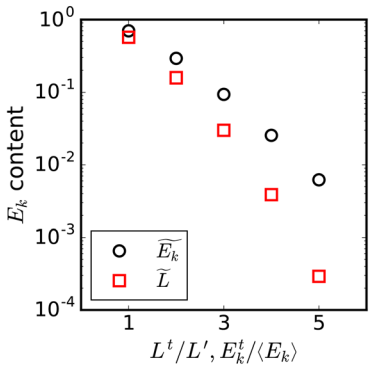

(e) Kinetic energy fraction contained in $\widetilde{L}$ and $\widetilde{E_k}$ regions.

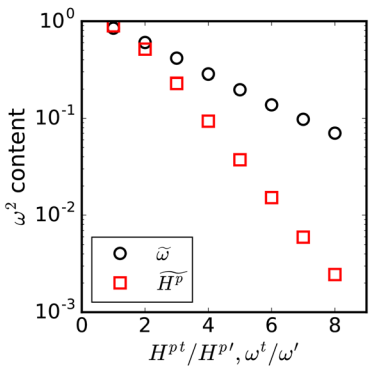

(f) Enstrophy fraction contained in $\widetilde{\omega}$ and $\widetilde{H^p}$ regions.

FIG. 20. Statistics of inclusivity between (a) $\widetilde{L}$ and $\widetilde{E_k}$, and (b) $\widetilde{H^p}$ and $\widetilde{\omega}$ regions, where each region, say $\widetilde{\psi}$, is defined as the thresholded ψ field in the range $\widetilde{\psi} \equiv \psi_1 \le \psi \le \psi_2$. Panels (c) and (d) show the volume fractions of different thresholded regions of the fields, and panels (e) and (f) show the kinetic energy and enstrophy contents of the regions, respectively. (a) Inclusivity of $\widetilde{L}$ and $\widetilde{E_k}$. (b) Inclusivity of $\widetilde{\omega}$ and $\widetilde{H^p}$. (c) Volume fraction V_f of $\widetilde{L}$ and $\widetilde{E_k}$. (d) Volume fraction V_f of $\widetilde{\omega}$ and $\widetilde{H^p}$. (e) Kinetic energy fraction contained in $\widetilde{L}$ and $\widetilde{E_k}$ regions. (f) Enstrophy fraction contained in $\widetilde{\omega}$ and $\widetilde{H^p}$ regions.

H^p kernels are comparable at these levels. Beyond that, the L field becomes (relatively) more inclusive in the H^p field (around $L > 3L'$ and $H^p > 3H^{p\prime}$), where the volume fraction of the kernels of L is smaller than the volume fraction of the kernels of H^p. This is because the H^p field can attain very high values in comparison with the L field (see Fig. 14), and the volume fraction decay of L is steeper than that of H^p.

VII. FLOW STRUCTURES IN HOMOGENEOUS ISOTROPIC TURBULENCE

A. Introduction

So far, we found that turbulence fields comprise (at least) two distinct coherent structures, both corresponding to high field magnitude regions, and both having a locally jet-like structure. High E_k regions

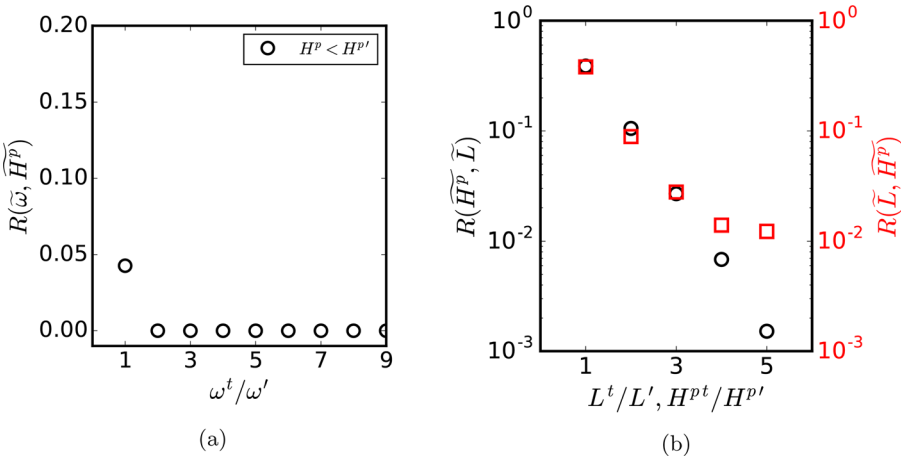

FIG. 21. Inclusivity of (a) high ω regions in low H^p regions and (b) high H^p regions and high L regions.

yield high L values, and form compact, well-aligned streamlines. High ω^2 regions have highly aligned vorticity streamlines and are associated with velocity-swirls in their neighborhoods (which has been qualitatively shown before[19–22]).

We now showcase individual flow structures in high L and H^p regions, demonstrating how regions of instantaneous coherence manifest in turbulence. Next, we shall investigate the Biot–Savart composition of these structures. This allows us to address two crucial questions regarding their composition (i) to what degree are these structures "self-inducing" in a Biot–Savart sense, as opposed to being externally induced and (ii) what is the relative contribution of different levels of vorticity in inducing these structures, and the total velocity field in general. Note that by "self-induction," we imply a flow field within a region $\mathcal{R}_\Omega$ being generated by the vorticity in $\mathcal{R}_\Omega$, while an externally induced (kinematically non-local) structure in $\mathcal{R}_\Omega$ is generated by the Biot–Savart contribution of the vorticity outside of $\mathcal{R}_\Omega$ (as illustrated in Fig. 3). This allows us to "disentangle" the velocity field into its various Biot–Savart components. We further show qualitatively and quantitatively, what is the relative contribution of different levels of vorticity in inducing these structures, and the total velocity field in general. A brief note on some practical concerns regarding the calculation of the Biot–Savart velocity field is presented in the Appendix.

We first show individual flow structures qualitatively, following which, we consider the Biot–Savart contributions from a statistical perspective. Finally, we summarize the picture of turbulence organization that emerges from this study.

B. Individual flow structures

We first look at regions of high L by identifying isolated contours of the L field. High L regions, since they coincide with high E_k, are the "energy containing" structures. We find that the level of $2.5L'$ marks regions of high correlation, which occupy ≈2% of the volume while containing ≈10% of the total kinetic energy. At this level, the L field forms separate, individual regions, which can be considered distinctly. At lower correlation levels ($L < 1.5L'$), the L regions become more connected, while at higher levels ($L > 3.5L'$), the L regions become very small (occupying less than 0.2% of the volume). We, hence, select $2.5L'$ regions for the present analysis, while the results remain essentially similar for slightly different values of L.

Figure 22(a) shows three isolated kernels of $2.5L'$, along with the local flow streamlines (initialized within a small region around the core of the correlation kernels), while panel (b) shows the compact, *jet-like* coherent flow streamlines separately. This visually confirms high E_k structures to be *velocity-jets*, with a core region of highly aligned streamlines, which often have low curvature along their length. The streamlines diverge into more chaotic patterns away from the correlation kernels, which shows that the coherence of these structures is localized. We note that these structures are not directly features of the "energy injection" mechanism, since by construction, the forcing $\mathbf{F}$ is white-noise in time, such that the quantity $\langle \mathbf{F} \cdot \mathbf{u} \rangle = 0$.[42,46] Hence, the forcing does not correlate with flow structures, which typically have a finite lifetime. Comparing these results for decaying turbulence can help to further establish this.

We reconstruct the self-induced Biot–Savart velocity field of these structures, using all $L \geq 2.5L'$ regions. While in principle *only* the vorticity contained in the isolated regions should be used, it adds additional complexity to the calculation. Since the L regions remain isolated in space and, moreover, have low ω (refer to Table III), their already low Biot–Savart contribution is negligible outside the correlation regions. Hence, in practice, the self-induced velocity field around any high L region is essentially the same even upon reconstructing the velocity using all $L \geq 2.5L'$ regions.

Figure 22(c) shows streamlines of the self-induced velocity of the kernels in panel (a), which have a very low magnitude and a very different structure than the total velocity in these regions. These two aspects lead to an interesting finding that the high E_k velocity-jets are not self-inducing and are *kinematically non-local*, being entirely externally induced, as shown in Fig. 22(d). She *et al.*[49] suggested that in isotropic turbulence, strong gradient regions are associated with strong coherence, while weak gradient regions were deemed essentially random. We show that not only do the coherent and dynamically important "energy containing structures" correspond to weak-gradient regions, but, as subsequent analysis reveals, they have a subtle relation to intermediate background vorticity. These results are similar for correlation kernels determined in the range $2.0 \leq L \leq 3.0$. At much higher L regions will have an even smaller self-induced contribution due to their lower levels of vorticity, since the two are anti-correlated (see Fig. 19), while at much lower levels of L, the self-induced contribution can be expected to increase.

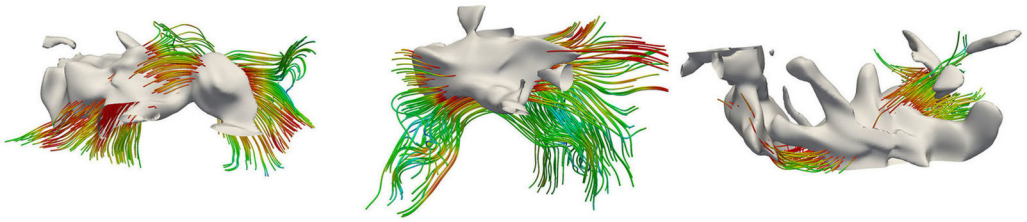

(a) Contours of $L = 2.5L'$ along with local streamlines of the total velocity field.

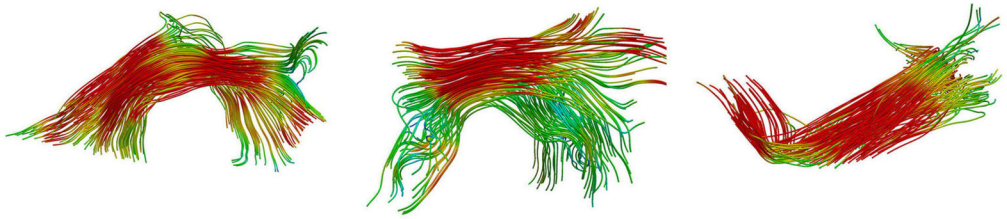

(b) Streamlines of the total velocity.

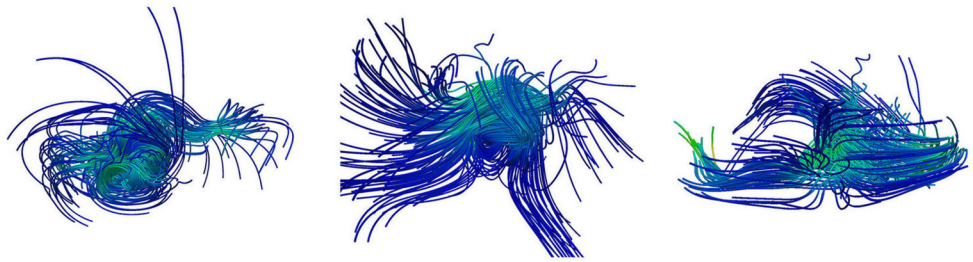

(c) Streamlines of the self-induced velocity of $L \geq 2.5L'$ regions.

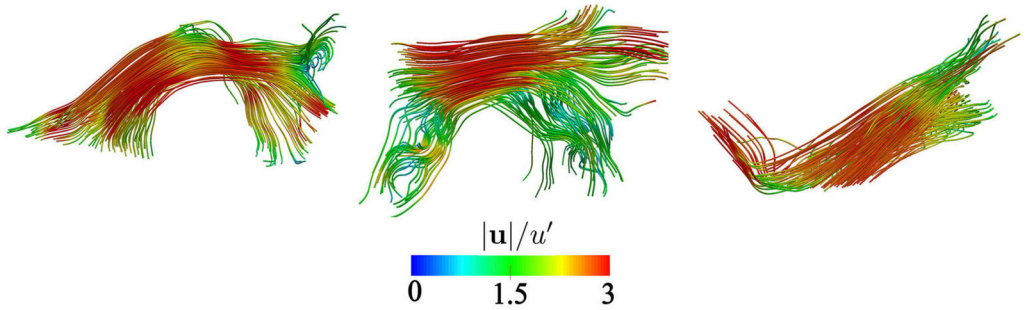

(d) Streamlines of the externally-induced velocity.

FIG. 22. Velocity-jets corresponding to three regions of $2.5L'$ are shown: (a) $L = 2.5L'$ contours and total-velocity streamlines, (b) total-velocity streamlines alone, (c) self-induced velocity streamlines and (d) externally induced velocity streamlines. Colorbar shows the velocity magnitude.

TABLE III. Contributions of the self-induced and externally induced flow to the total velocity within correlation kernels used to identify high kinetic energy jets and high enstrophy swirling regions, i.e., $2.5L'$ and $5H^{p\prime}$, respectively.

Region	V_f	Mean ω	Mean E_k	BS-self	BS-external
$L \geq 2.5L'$	0.02	$0.78\omega'$	$3.67\langle E_k\rangle$	11.32%	88.65%
$H^p \geq 5H^{p\prime}$	0.00018	$3.46\omega'$	$1.12\langle E_k\rangle$	34.15%	65.84%

Next, we show the flow structure around kernels of H^p. The $5H^{p\prime}$ level is found to represent a high level of the correlation field, while occupying a meaningful volume (≈0.018%) and accounting for 4% of the total enstrophy, while forming distinct kernels. Higher values, like $H^p > 7H^{p\prime}$, do not occupy significant fractions of the volume (<0.001%), while at lower levels, the H^p field becomes more diffused than the vorticity field [see Fig. 20(b)] and does not adequately represent regions of strong swirling motion. The present results are similar in the range $4 < H^p/H^{p\prime} < 6$.

Figure 23(a) shows three instances of $5H^{p\prime}$ kernels with the local flow streamlines, while Fig. 23(b) shows the streamlines separately. Toward the core of these structures, the velocity field shows a strong swirling motion, while the flow decays into more disordered streamlines away from the core regions. The velocity of these structures is mostly in the intermediate and low E_k range (with very small occurrences of high E_k).

Figure 23(c) shows the self-induced velocity field, which forms purely swirling motion in the core regions, along with an instance of two vortices interacting in a figure-eight velocity pattern (right-most). This swirling velocity decays to a low amplitude away from the core region, which shows that the strong vorticity at the core influences the total velocity field only within a small region of influence (due to the rapid decay of the Biot–Savart contribution). The externally induced velocity streamlines in panel (d) resemble the total velocity streamlines outside the core of the H^p regions and is found to have an intermediate amplitude. This shows that some region *around* the $5H^{p\prime}$ kernels also contains vorticity of a large enough amplitude to generate swirling motion in the neighborhood. High H^p structures are, hence, a superposition of self-inducing swirling flow, along with a background induced flow field, which has a swirling component and a more disorganized structure away from the core regions. Performing this calculation for different thresholds of H^p will change the relative contribution of the self-induced and externally induced velocities to the total

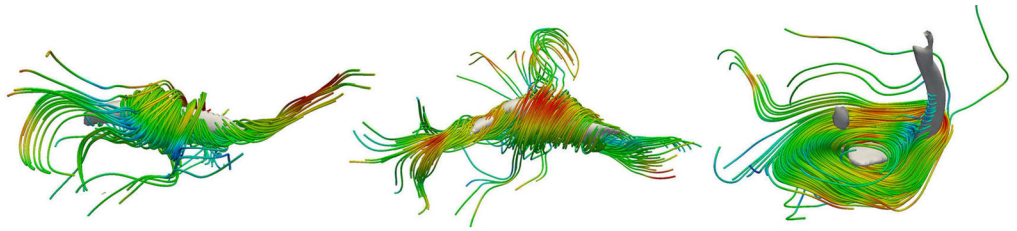

(a) Contours of $H^p = 5H^{p\prime}$ along with local streamlines of the total velocity field.

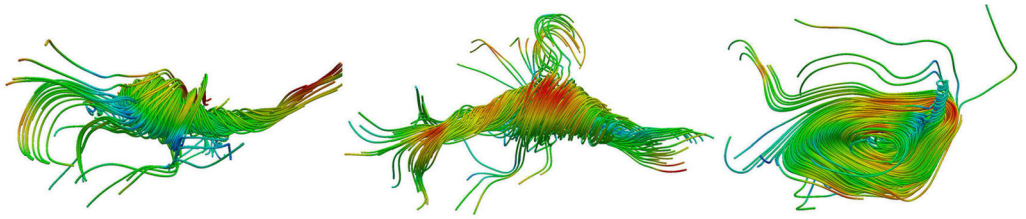

(b) Streamlines of the total velocity.

(c) Streamlines of the self-induced velocity.

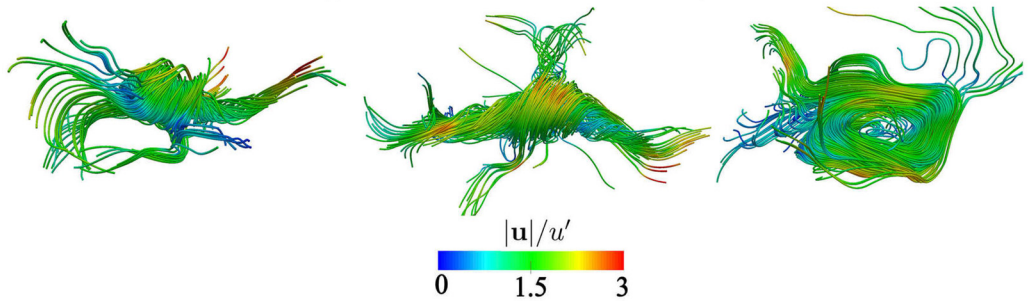

(d) Streamlines of the externally-induced velocity.

FIG. 23. Velocity-swirls around three high H^p regions are shown: (a) $5H^{p\prime}$ contours and total-velocity streamlines, (b) total-velocity streamlines alone, (c) self-induced velocity streamlines, and (d) externally induced velocity streamlines. Colorbar shows the velocity magnitude.

velocity. At lower H^p values, the correlation kernel is larger, and it will contain more vorticity (in the high and intermediate ranges) and, hence, will have a larger self-induced Biot–Savart contribution.

To quantify the self-induced and externally induced contributions to the velocity field, we define a general measure C using the Biot–Savart reconstructed velocity field $\mathbf{u}_{\mathrm{BS}}$ and the total velocity field $\mathbf{u}$ as

$$C(\mathcal{R}_\Omega, \mathcal{R}_{\mathrm{BS}}) = \frac{\langle \mathbf{u} \cdot \mathbf{u}_{\mathrm{BS}} \rangle_\Omega}{\langle \mathbf{u} \cdot \mathbf{u} \rangle_\Omega}, \tag{47}$$

where $\mathcal{R}_\Omega$ denotes the region where C is evaluated, which can be defined based upon a conditional sampling criterion, for instance, $\mathcal{R}_\Omega \equiv L > L^t$, where L^t is a threshold value for L. The regions of vorticity used to generate the Biot–Savart velocity field $\mathbf{u}_{\mathrm{BS}}$ are denoted by $\mathcal{R}_{\mathrm{BS}}$ (also a conditional sampled volume). Finally, $\langle \cdot \rangle_\Omega$ denotes averaging over the region $\mathcal{R}_\Omega$. We also use this measure to test the accuracy of the Biot–Savart reconstruction, by calculating $C(V, V)$, i.e., the correlation over the total volume V, of the total velocity field $\mathbf{u}$, with the Biot–Savart reconstructed velocity field $\mathbf{u}_{\mathrm{BS}}$ generated using the total vorticity field. It is found that $C(V, V) \approx 0.99$, which means that our Biot–Savart reconstruction faithfully reproduces 99% of the velocity field, while there is a numerical error of ≈1%.

In Table III, we quantify the self-induced and externally induced Biot–Savart contributions to the velocity field within all $2.5L'$ and $5H^{p\prime}$ kernels, using Eq. (47). The self-induced component of the velocity-jets, i.e., $C(L \geq 2.5L', L \geq 2.5L')$, is found to be ≈11%, while the externally induced velocity dominates these structures with ≈88% contribution, which is quantitative evidence of their degree of kinematic non-locality. We here observe what might be a more general result that, from a Helmholtz-decomposition perspective, in *any* vector field (which has a zero infinity-field contribution, i.e., zero-mean), if a region has *jet-like* structure, it *must* be externally induced. This is because the gradients of the field within the jet-like region will be small or negligible. For instance, by corollary to the velocity-jets, the vorticity-jets identified by $\mathbf{G}$ and $\mathbf{G}^{\mathbf{s}}$ must also be externally induced by the *divorticity*, $\nabla \times \boldsymbol{\omega}$, since $\nabla \cdot \boldsymbol{\omega} = 0$ [while in general the divergence might contribute as well, see Eq. (18)], if a similar Biot–Savart reconstruction is performed using the divorticity field, which we do not explore.

For the $5H^{p\prime}$ structures, the self-induced contribution, i.e., $C(H^p \geq 5H^{p\prime}, H^p \geq 5H^{p\prime})$ is ≈34%, while the externally induced contribution is ≈66%. Note that we performed these calculations for regions contained *inside* the correlation kernels, however, the kernels themselves are markers of larger regions of coherence *around* them. Particularly, the $5H^{p\prime}$ regions occupy a small fraction of the volume (≈0.018%), while they are associated with swirling motion *outside* the kernel regions. This is why the velocity inside $5H^{p\prime}$ regions has a relatively low self-induced contribution, as it is significantly influenced by the strong vorticity, which can be found in the immediate neighborhood of the $5H^{p\prime}$ kernels [see Fig. 20(b), where the right $y-$ axis shows that a large fraction of the high vorticity is contained outside $5H^{p\prime}$ regions].

Finally, jet-like and swirling-flow structures were found to correspond to high L and high H^p regions, respectively, also in a reference Johns Hopkins Turbulence Dataset.[50]

C. Contributions from different levels of vorticity in generating flow structures

So far, we have shown that high kinetic energy jets are mostly externally induced coherent flow regions, while high enstrophy swirling regions are a superposition of self-induced flow and background induced flow. We now show, and quantify, the relative Biot–Savart contribution of different levels of the vorticity field in generating these structures, and the total velocity field in general. From the outset, one can expect that the weak vorticity range ($\omega_b \ll \omega'$) will have a small or negligible Biot–Savart contribution in generating the velocity field, due to the low vorticity amplitude. Significant contributions can come from (i) the strong vorticity, i.e., $\omega_b \gg \omega'$, which can intermittently assume very large amplitudes, albeit with a low volume fraction [see Fig. 12(c)] and (ii) the intermediate background vorticity, i.e., $\omega \sim \omega'$, which has a lower magnitude, but permeates most of the volume and can hence have, when combined, a significant Biot–Savart contribution.

We divide the vorticity into logarithmically spaced bins $\omega_l \leq \omega_b/\omega' < \omega_h$, with the lower and higher vorticity limits ω_l and ω_h. To determine the precise range of the bins, we start with the original classification of $\omega \geq 4\omega'$ as "strong" vorticity by She *et al.*[21] This is roughly where deviation from Gaussianity begins in the vorticity PDF, see Fig. 12(b). Hence, we form a vorticity bin for the range $\omega \geq 4\omega'$. Since almost the entire volume, i.e., ≈99%, has vorticity lower than $4\omega'$, we need a number of separate vorticity bins for the range $\omega < 4\omega'$. We do this by successively dividing the upper limit of vorticity for each bin by a factor of 2, in total creating 7 bins, which have been detailed in Table IV. We also give a classification for these bins based upon the vorticity amplitude, for purpose of further discussion. The choice of these 7 bins, albeit arbitrary, gives a good representation of the different vorticity levels with a sufficient separation of scale in the vorticity magnitude, while highlighting the small region around the peak of the vorticity PDF.

We then compute the Biot–Savart velocity field, corresponding to each vorticity bin individually, while the sum of all these Biot–Savart fields together gives the total velocity field. Figure 24 shows planar velocity streamlines (in the xy-plane, at an arbitrary z location, which is representative of the planar streamline structure found throughout the data), for Bin1–Bin7 going from panels (a)–(g), while panel (h) shows the streamlines of the total velocity field. Furthermore, panel (i) shows the planar field of seven vorticity bins, colored by number, along with $2.5L'$ regions shown as dashed contour lines and $5H^{p\prime}$ regions shown as solid contour lines (the latter, being

TABLE IV. Vorticity field divided into seven logarithmically spaced bins, along with an indicative classification based upon the vorticity amplitude.

Bin	$\omega_l \leq \omega_b/\omega' < \omega_h$	Classification
Bin1	$0 \leq \omega_b/\omega' < 0.1$	Weak
Bin2	$0.1 \leq \omega_b/\omega' < 0.25$	Weak
Bin3	$0.25 \leq \omega_b/\omega' < 0.5$	Weak
Bin4	$0.5 \leq \omega_b/\omega' < 1.0$	Intermediate weak
Bin5	$1.0 \leq \omega_b/\omega' < 2.0$	Intermediate high
Bin6	$2.0 \leq \omega_b/\omega' < 4.0$	High
Bin7	$4.0 \leq \omega_b/\omega' < \infty$	Very high

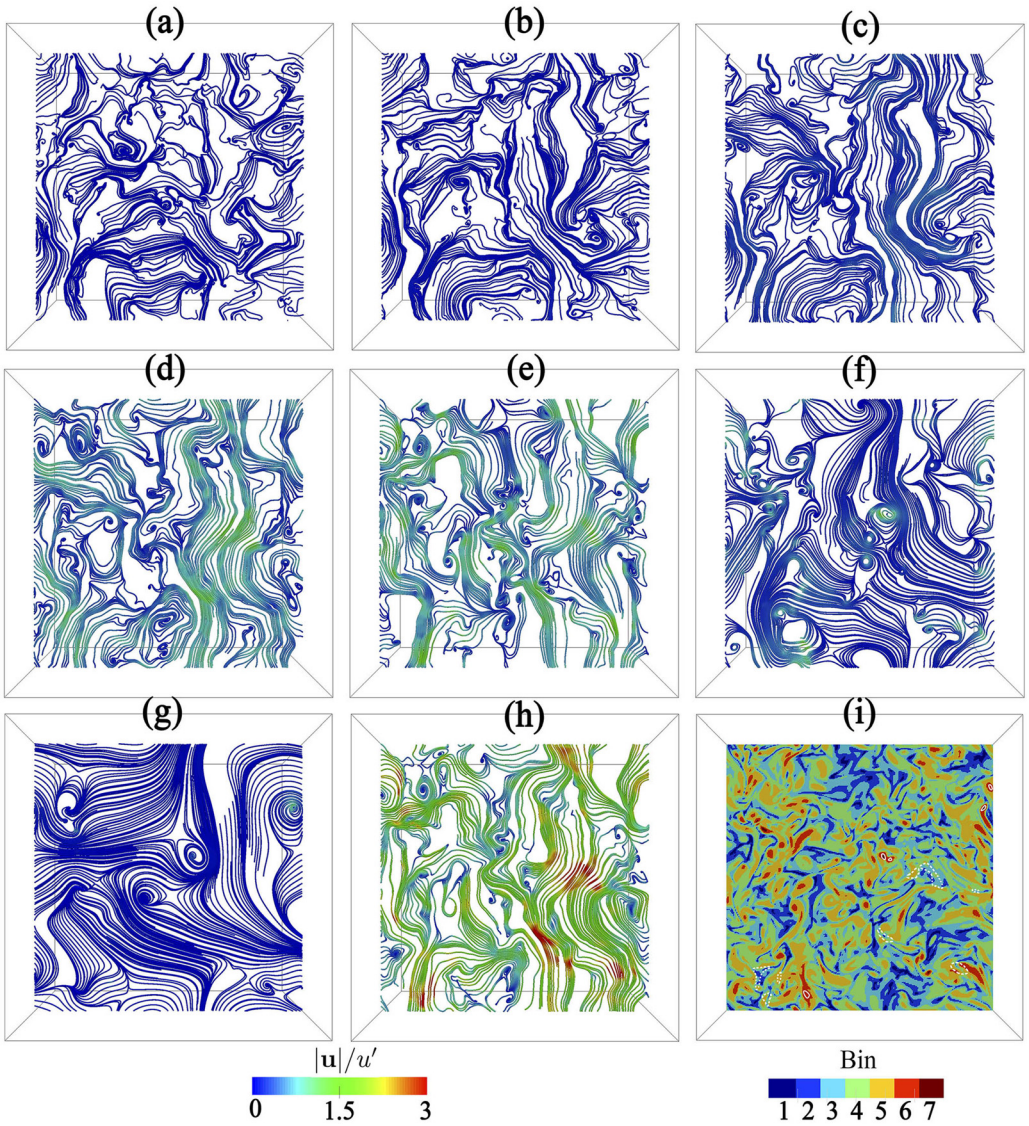

FIG. 24. Planar velocity streamlines (in the entire $xy-$ plane, at an arbitrary z location) have been shown for Bin1 through Bin7 going from panels (a) through (g), while panel (h) shows the streamlines of the total velocity field. Panel (i) shows the vorticity field colored by the bin number, along with contours of $2.5L'$ (dashed white lines) and $5H^{p'}$ (solid white lines). Colorbar shows the velocity magnitude.

very small, can be seen upon zooming into the figure). We first consider the total velocity streamlines in panel (h). The overall structure appears disorderly, with mostly E_k in the intermediate range. A few small regions contain high E_k jets, where the streamlines become well aligned. Other regions of aligned streamlines, albeit with intermediate E_k, can also be seen. The total streamline structure does not seem to result from a single (or a few) "large eddies," as for instance could be seen in the Taylor-Green velocity structure (see Fig. 7). A few small regions with swirling velocity, with intermediate and weak E_k, can also be seen. The vorticity bins in panel (i) also appear mostly disorderly. Most of the volume is occupied by Bin4 and Bin5, which have a very convoluted, fragmented structure, and there is no clear large-scale organization of the vorticity, which is perhaps the reason why a large-scale organization does not emerge in the velocity field (as happens in the case of the Taylor–Green velocity field, where a few large-scale velocity structures are associated with an underlying pattern in the vorticity field). Furthermore, the contours of $2.5L'$ show that these regions mostly coincide with intermediate and weak vorticity, showing that the jet-like flow emerges in regions of weak vorticity, surrounded by regions of intermediate (and occasionally, strong) vorticity. Contours of $5H^{p'}$ are found coinciding with strong vorticity bins, i.e., Bin6 and Bin7. It can be seen that the $5H^{p'}$ contours are surrounded by relatively larger regions of high vorticity, corresponding to Bin6—which further explains why the self-induced flow due to $5H^{p'}$ regions

(see Fig. 23) is weak and does significantly contribute to the swirling-flow, which receives a large contribution from the surrounding strong vorticity.

Panel (a) shows that Bin1 generates disordered velocity streamlines, with a negligible amplitude, as can be expected from the low vorticity magnitude in this bin. Panels (b) and (c), corresponding to Bin2 and Bin3, show that the streamlines due to these bins begin to have a weak organization, similar in pattern to the streamlines due to Bin4 and Bin5, which resemble some of the larger features of the total velocity field shown in panel (h). The magnitude of the streamlines due to Bin2 and Bin3, however, is still weak. Since Bin3 surrounds Bin4 and Bin5, it is not surprising that the velocity generated by them has a similar shape in many regions. Panel (d) and (e), i.e., Bin4 and Bin5, most resemble the total velocity field in panel (h), in both structure and velocity magnitude. Panel (f) shows Bin6, which has small, localized, regions of intermediate velocity amplitude, and larger regions of ordered streamlines with a low amplitude. Finally, panel (g) shows the streamlines for Bin7, corresponding to the very high vorticity range ($\omega/\omega' \geq 4.0$). At this range, the vorticity regions become spatially isolated and occupy very small volumes. The associated velocity field shows large-scale structures, which look like a more disordered Taylor–Green flow pattern. However, due to the very low velocity magnitude, these structures do not emerge in the total velocity field in panel (h), as they are overwhelmed by the contributions from the other bins. Bin7, hence, influences the velocity field *only* in the immediate neighborhood of the regions of high vorticity. The precise contribution of each bin to generating the velocity field is quantified in Sec. VII D.

We next look at instances of individual flow structures, along with the Biot–Savart contribution of each vorticity bin in generating this structure. Figure 25 focuses on the first $2.5L'$ structure shown in Fig. 22(a). Panels (a)–(g) show the Biot–Savart contribution of Bin1 to Bin7 in generating the total velocity structure, which is shown in panel (h). We find that the most significant contribution comes from Bin4 and Bin5, i.e., panels (d) and (e), both of which represent bins with $\omega \sim \omega'$. The streamlines resemble the structure of the high E_k jet in panel (h) and also have an intermediate level of velocity amplitude. Bin6 also has a small contribution to the total velocity structure. Bin1 and Bin2 have a negligible contribution, while Bin3 has a mild contribution. Finally, it is interesting to find that Bin7, which corresponds to the higher levels of vorticity, also has a negligible contribution to the generation of the kinetic energy jet. This result also reflects the spatial

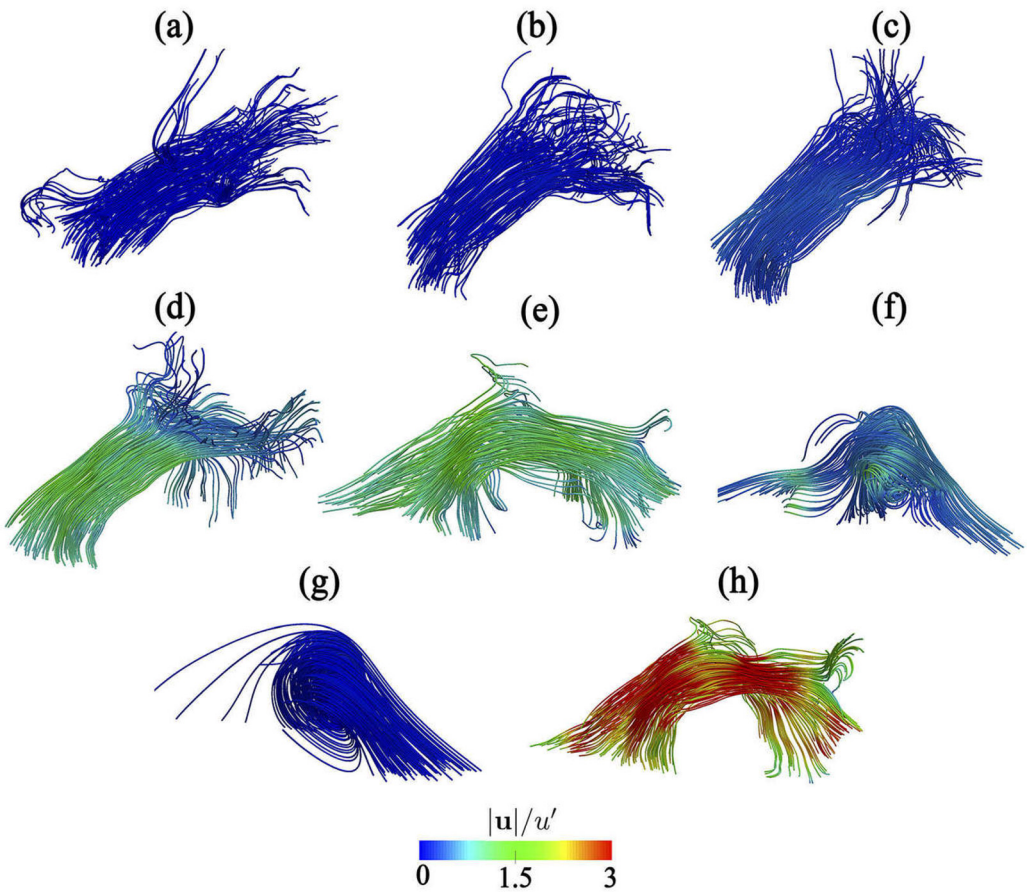

FIG. 25. A single $2.5L'$ high kinetic energy region is highlighted, where panels (a)–(g) show the contribution from Bin1 to Bin7 to the generation of the total velocity field shown in panel (h).

exclusivity between high kinetic energy and high enstrophy. From Figs. 19(a) and 19(c), we know that the joint distribution of L and ω is anti-correlated. The very localized, high vorticity regions, do not extend their influence on the velocity field beyond their immediate neighborhoods. These results show that high kinetic energy jets are induced by non-local intermediate vorticity contributions, in the range of $\omega \sim \omega'$.

Figure 26 shows the first $5H^{p\prime}$ swirling flow structure from Fig. 23(a). The Biot–Savart contribution from Bin1 to Bin7 is shown in panels (a) to (g). Bin5 and Bin6 in panels (e) and (f) are found to contribute most significantly to the swirling flow region. Bin1 to Bin3 in panels (a) to (c) have a negligible contribution, while Bin4 in panel (d) has a relatively mild velocity and can, hence, be expected to have only a small contribution to the generation of the total velocity. Bin7 in panel (g), corresponding to the highest range of vorticity, is also found to generate a very weak velocity field and contribute negligibly to the swirling flow region in this example. Note that this range of vorticity, $\omega > 4\omega'$, occurs intermittently. From the first structure shown in Fig. 23(c), we know that this particular $5H^{p\prime}$ region self-induces a swirling velocity field, albeit with low magnitude. Since the Bin7 contribution is found to be negligible, we can conclude that this structure contains vorticity in the range of Bin6 and lower. In general, high H^p structures will tend to have high vorticity (as evident from the joint-PDF in Fig. 19), while the higher amplitude regions will become exponentially smaller in size. Some of the high H^p regions will indeed have contributions from Bin7, which becomes clear in Sec. VII D where we quantify the vorticity bin contributions statistically.

D. Statistics of the Biot–Savart contributions

So far, the results show that both kinetic energy jets (identified by $L > 2.5L'$) and swirling flow regions (identified by $H^p > 5H^{p\prime}$) have a significant Biot–Savart contribution from the intermediate range vorticity. This finding is interesting, since it implies that the bulk of the volume, which contains vorticity of a relatively mild magnitude ($\omega \sim \omega'$), is significant in determining the structure of the velocity field, possibly everywhere. We quantify this by calculating the correlations $C(L > 2.5L', \omega_b)$ and $C(H^p > 5H^{p\prime}, \omega_b)$, along with $C(V, \omega_b)$,

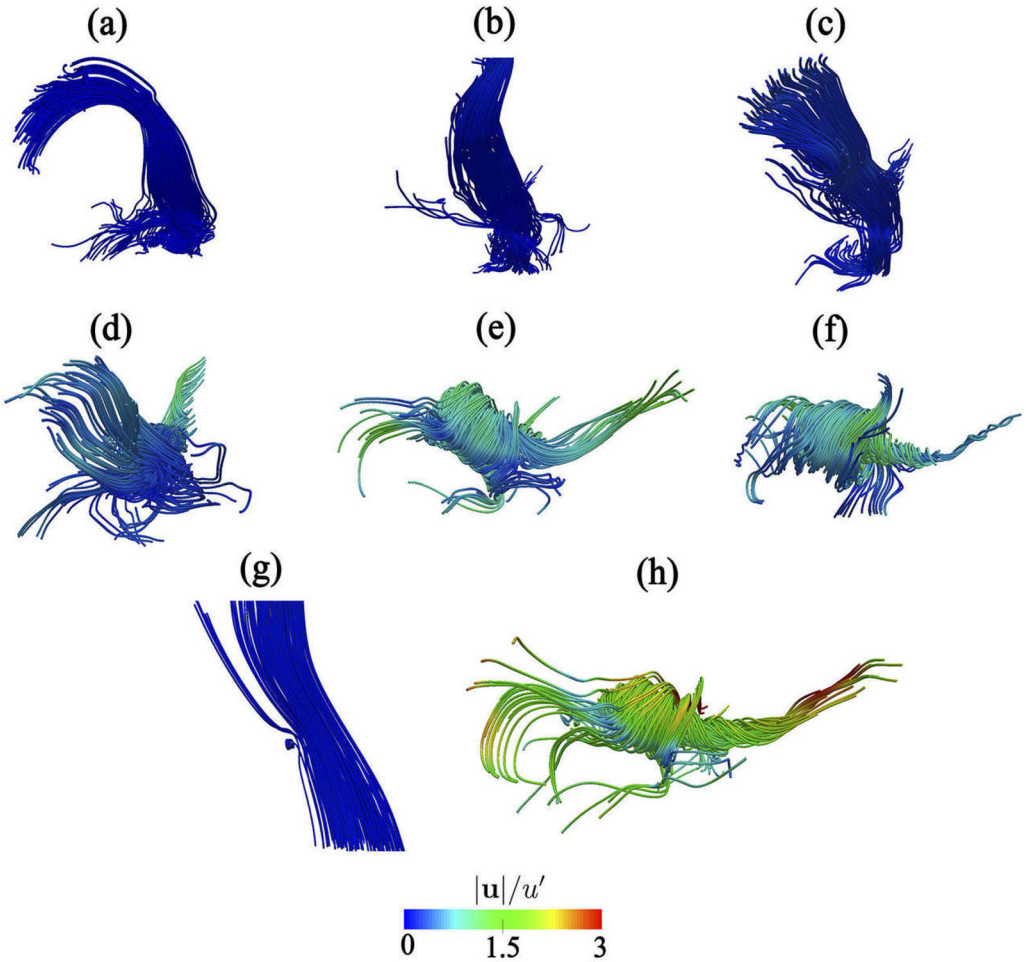

FIG. 26. A single $5H^{p\prime}$ swirling flow region is highlighted, where panels (a)–(g) show the contribution from Bin1 to Bin7 to the generation of the total velocity field shown in panel (h).

which have been shown in Fig. 27. Note that the x-axis in these figures shows the limits of consecutive vorticity bins, and the points representing each bin, which have been placed in between their corresponding limits, have been connected with lines to guide the eye. Furthermore, the second y-axis (on the right) shows the volume fraction (in red) of each vorticity bin $V_f(\omega_b)$, to give a complete picture, which includes the Biot–Savart contribution of each vorticity bin along with the volume it occupies.

The black curve (circles) in Fig. 27(a) shows $C(L > 2.5L', \omega_b)$. The highest contribution to the induction of high L kinetic energy jets, of ≈45%, comes from Bin5, i.e., $1 \leq \omega_b/\omega' < 2$, which occupies ≈25% of the volume. Bin4, i.e., $0.5 \leq \omega_b/\omega' < 1$ contributes ≈26% while occupying ≈40% of the volume. The only other significant contribution is from Bin6, i.e., $2 \leq \omega_b/\omega' < 4$, of ≈20%, which occupies a much smaller volume (<4%). Strong vorticity, i.e., $\omega_b/\omega' \geq 4$, has a negligible Biot–Savart contribution to the generation of the kinetic energy jets. This again reflects the spatial exclusivity of high kinetic energy and high vorticity regions, where the latter occupies isolated, small regions of the volume. It is interesting to find that strong vorticity, which forms the long tails of the vorticity PDF, is insignificant in the Biot–Savart sense. Furthermore, as expected, weak vorticity, i.e., $\omega_b/\omega' < 0.5$, also has a negligible contribution.

The blue curve (squares) in Fig. 27(a) shows $C(H^p > 5H^{p'}, \omega_b)$, where the distribution of vorticity bin contributions is found shifted toward the higher vorticity ranges, as can be expected. The intersection between the distribution of bin-wise volume fraction and bin-wise Biot–Savart contribution, in comparison with $L > 2.5L'$, is also shifted toward higher vorticity levels. In this case, Bin6, i.e., $2 \leq \omega_b/\omega' < 4$, has the highest contribution (≈34%) to generating flow inside $5H^{p'}$ regions, while occupying only 4% of the volume. This is closely followed by the contribution from Bin5 of ≈30%. Strong vorticity in the range of $\omega_b/\omega' \geq 4$ is also found to contribute ≈13%, i.e., a small amount as was anticipated in the discussion regarding Fig. 26. One difference between the distribution of vorticity bin contributions for $2.5L'$ and $5H^{p'}$ is that the former [black curve in Fig. 27(a)] appears relatively narrower and higher peaked than the latter [blue curve in Fig. 27(a)], which has a broader distribution. This reflects the fact that the velocity field in high H^p swirling flow regions has a background induced contribution, and a degree of self-induction due to the high vorticity levels.

Trends in the distribution of vorticity bin contributions when considering the entire velocity field $[C(V, \omega_b)]$, shown in Fig. 27(b), are found to be the same as those for $C(L > 2.5L', \omega_b)$. It can be summarized that vorticity in the range of $0.5 \leq \omega_b/\omega' < 1.0$ (Bin4) occupies the maximum volume, but due to a lower amplitude has a slightly smaller Biot–Savart contribution than vorticity in the range $1 \leq \omega_b/\omega' < 2$ (Bin5), which has vorticity of a higher amplitude, but occupies a lower fraction of the volume. Together, the vorticity in these two bins, which is essentially at the level of ω' (and may be termed *intermediate*), both permeates most of space and generates most of the velocity field. The strong vorticity range, i.e., $\omega/\omega' \geq 4$, remains insignificant for generating the velocity field, except in the immediate vicinity of high vorticity regions.

E. Summary

In summary, high L structures, which have high E_k, are compact, coherent velocity-jets, while containing very low levels of vorticity. The coherence of these structures is externally induced, with most dominant contributions of the intermediate background vorticity. The high H^p regions that coincide with high ω^2 are interspersed in a more or less random manner through the flow field, and they do not add up together, in a Biot–Savart sense, to give rise to high E_k structures. These regions form vorticity-jets that are surrounded by velocity-swirls, which are a superposition of self-induced swirling flow and an intermediate background vorticity induced flow. This gives a clear picture of these flow structures that together comprise turbulence fields (at high amplitudes), along with their Biot–Savart compositions.

VIII. CONCLUSIONS AND OUTLOOK

We developed a generalized correlation framework for identifying instantaneous, spatial, coherent structures in vector fields. Interpreting coherence to mean correlation, we began by generalizing the usual two-point correlation tensor, i.e., a statistical concept, to an instantaneous and deterministic correlation measure. This measure is reduceable to a correlation manifold around each spatial point, while, for simplicity, we sample this manifold along an arbitrary orthogonal base, yielding three-tuple correlation fields. Based on this general method, we propose several simple correlation measures using the velocity and vorticity, aimed at identifying basic field patterns. These are summarized below, together with some general possibilities:

1. **L** identifies regions of well aligned (parallel) velocity streamlines, where the velocity magnitude is also high. $\mathbf{L}^s$ identifies non-local symmetries/anti-symmetries of velocity streamlines, also

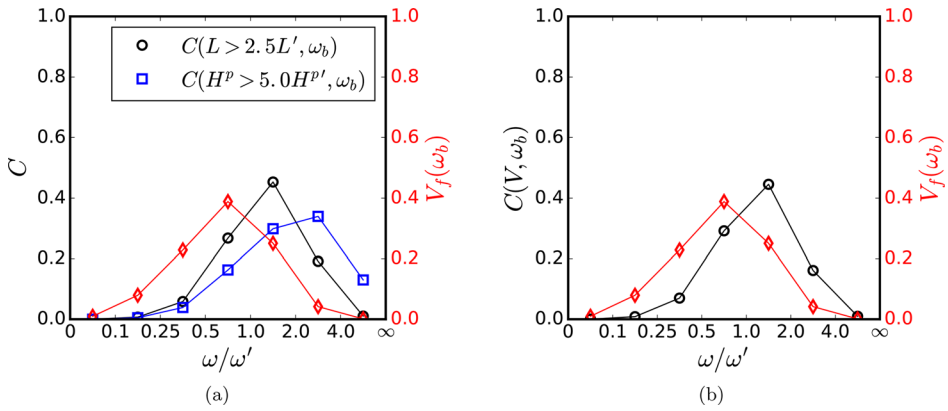

FIG. 27. Distribution of vorticity bin contributions to (a) the flow *within* L and H^p regions, i.e., $C(L > 2.5L', \omega_b)$ and $C(H^p > 5H^{p'}, \omega_b)$, respectively, and (b) the generation of the total flow field, in the entire volume V, i.e., $C(V, \omega_b)$. The left y-axis shows the correlation C, while the right y-axis shows the volume fraction of the vorticity bin $V_f(\omega_b)$.

weighing in the velocity magnitude. Both **L** and $\mathbf{L^s}$ yield high values in uniform (or jet-like) velocity regions, while at the core of swirling velocity regions with a high magnitude, only $\mathbf{L^s}$ is high.
2. **G** and $\mathbf{G^s}$ are defined for the vorticity field, analogously to **L** and $\mathbf{L^s}$, respectively. Both correlations yield high values that are vortex core regions where the vorticity if well-aligned and high, while $\mathbf{G^s}$ can also identify larger symmetries/anti-symmetries in the vorticity field.
3. **H** and $\mathbf{H^p}$ are defined, inspired by the Biot–Savart law, as line and planar measures, respectively, of the correlation between the vorticity at a point with the surrounding velocity. These correlations yield high values when a region of swirling velocity is induced by the local vorticity. In general, this is not necessarily true, and one could have regions of high vorticity without swirling velocity, when the velocity is induced non-locally in a Biot–Savart sense.
4. Correlations $\hat{\mathbf{L}}$ and $\hat{\mathbf{G}}$, operating on the velocity and vorticity fields point-wise normalized to unit vectors, are able to separate organization effects from field magnitude effects and have potential for studying an intermediate range of structures.
5. Similarly, other correlation measures can be easily constructed in order to identify different types of structures. For example, correlations involving symmetries and anti-symmetries between velocity and vorticity fields can be proposed to identify vorticity-stretching structures.
6. A variety of other correlations, for instance, using the force-density fields of pressure gradient and viscous stress, could be readily defined along similar lines to study turbulence dynamics. Relations between different fields could also be exploited.
7. The integration length of the correlations, Λ, provides a way to gauge structure sizes, and changing the limits of integration allows identifying purely non-local structures.
8. The correlations can be readily adapted to different dimensional data-sets, or be recast as space-time-correlations to study the evolution of spatial coherent structures.
9. Lastly, we underline that these correlations may be applied when the amplitude of the signal is larger than that of noise. In the reverse case, filtering procedures might be needed to tame the level of noise, for instance using Moving Window averaging or Top–Hat Fourier filtering, etc., following which the correlations may be calculated. In principle, any such pre-processing of the data is possible using global or local operations, and structures can be found in the processed fields. This may be important for experimental data, especially when investigating structures with mild amplitudes.

After testing the correlations on canonical flows, we applied them to a DNS dataset of incompressible, homogeneous isotropic turbulence, which led us to identify dominant coherent structures in turbulence. The Biot–Savart reconstruction of the velocity field, using different levels and regions of the vorticity field, revealed interesting features of the velocity field and its structures. These findings and their implications are summarized below:

1. Turbulence has, at least, two basic coherent flow patterns. These correspond, in the velocity and vorticity fields, to regions of *jet-like* alignment and a high field amplitude.
2. High E_k regions consistently yield high values of both **L** and $\mathbf{L^s}$, showing that they form *velocity-jets* and are not swirling regions (in which case only $\mathbf{L^s}$ would be high). These jets, being *energetic* and *unrelated* to regions of strong vorticity (as revealed by the Biot–Savart analysis), are *distinct* from the vortex-induced *weak* E_k streams proposed in the literature.[4] We only analyzed isotropic turbulence with structureless-in-time energy injection. In other kinds of flows, for instance, channel flow, where the energy injection has a spatio-temporal structure, the **L** and $\mathbf{L^s}$ fields may reveal other structures. Lastly, increasing levels of E_k lead to an increase in the local flow organization.
3. High ω^2 regions are found to yield high values of **G**, $\mathbf{G^s}$, **H,** and $\mathbf{H^p}$ correlations. The coincidence of **G** and $\mathbf{G^s}$ shows that these regions form *vorticity-jets* (which can be considered a particular kind of vortex tube) and that there are no significant anti-symmetry regions in the vorticity field. Predominantly high values of $\mathbf{H^p}$ in these regions further confirm that the neighborhood of high ω^2 structures invariably form *velocity-swirls*, as has been qualitatively described before,[19–22,49] further corroborated by the joint distribution of H^p and ω.
4. Spatial distribution statistics show that the velocity-jets and vorticity-jets (which are associated with velocity-swirls) are *spatially exclusive*. This is consistent with the dynamical separation between high E_k and the high ω^2 structures, which represent different parts of the Navier–Stokes dynamics.
5. Biot–Savart reconstruction of the velocity field shows that the velocity-jets are *kinematically non-local* entities, i.e., they are *externally* induced by non-local vorticity contributions (≈88%), while the self-induced contribution is low at ≈11% (since these structures have weak gradients). This result will translate to the Helmholtz-decomposition of other vector fields as well, since any jet-like vector field region will have weak gradients and cannot, therefore, self-induce. For instance, the vorticity-jets associated with high **G** and $\mathbf{G^s}$ are expected to be externally induced by the divorticity ($\nabla \times \boldsymbol{\omega}$), since the divergence of the vorticity is zero. This highlights the importance of our framework of using geometrical, non-local correlation criteria to identify structures, since, from any gradient-based perspective, the dynamically important high E_k structures will be shadowed in favor of gradient dominated structures.
6. The velocity-jets, furthermore, are dominantly induced by $\omega \sim \omega'$, which permeates the volume and has an intermediate (mild) magnitude, while strong vorticity has a negligible contribution. This suggests that, unlike what is usually held, mild-gradient regions are not wholly irregular; otherwise, they would not additively lead to coherent regions. This may be important from the perspective of Large Eddy Simulations (LES) of turbulence structures as well. If the flow organization at intermediate to large scales has an important contribution from the Biot–Savart interaction of small scales, the finite spectral cutoff in LES will not adequately capture the influence of these small scales.
7. High ω^2 velocity-swirls have a background vorticity contribution of ≈65% to their induction, and a self-induced flow of ≈35%. A significant Biot–Savart contribution (≈34%) comes from the $2 \leq \omega/\omega' < 4$ range. Intermediate, background vorticity, i.e., $0.5 \leq \omega/\omega' < 2$, contributes ≈50%. This shows that swirling velocity regions are structures in superposition of background and self-induced flows.

8. Flow streamlines of the entire velocity field appear, overall, disorganized, while being interspersed with localized regions of velocity-jets (high E_k, low ω^2) and velocity-swirls (moderate E_k, high ω^2). At intermediate field values, distinctions begin to blur and structures can overlap.
9. The bin-wise vorticity field also shows a disorganized structure. Most of the volume is occupied by a convoluted and fragmented intermediate vorticity field, i.e., $0.5 < \omega/\omega' < 2$, which is also found to most significantly induce the velocity field everywhere (≈80%). Vorticity in this range corresponds to the narrow (almost) Gaussian peak of the vorticity distribution. Strong vorticity ($\omega \geq 4\omega'$) is intermittent and appears in isolation and generates (in a Biot–Savart sense) a large-scale flow pattern, resembling a disordered Taylor–Green flow, which, due to its weak amplitude, does not contribute to the total velocity field. The influence of strong ω regions to the velocity is limited to their immediate neighborhood. Usually, most research has focused on extreme vorticity, for instance, due to its influence on mixing and particle dispersion. It turns out that the bulk of the velocity field and, in particular, the E_k containing regions are *impervious* to extreme vorticity. Weak vorticity, i.e., $\omega < 0.5\omega'$, as can be expected, does not contribute much to the generation of the velocity field.

A structural view of turbulence fields, as suggested by these results, is illustrated in Fig. 28. Particularly, the coherence of the kinetic energy containing jets being induced by non-local vorticity shows that these structures are not self-determining. The traditional cascade perspective of turbulence dynamics explains the phenomena as being dominated by high kinetic energy, large-scale structures, which in turn determine the structure and generation of successively smaller scales via an "eddy breakup" mechanism, dating back to the idea of Richardson.[26] The presence of externally induced, localized kinetic energy jets suggest a *nonhierarchical* flow organization. Most of the velocity field, which is traditionally believed to comprise a range of "coherent scales" (corresponding to the inertial range), is also generated, in a Biot–Savart sense, by the permeating, intermediate range background vorticity. Finally, small scale swirling flow regions are found to be a superposition of background induced flow and self-induced flow to varying degrees.

Within limitations, an alternative view on (homogeneous isotropic) turbulence can be considered, where its overall organization, along with its statistical features, can be thought to *emerge* from the combined contribution of the global vorticity field, dominated by the permeating intermediate background vorticity in the range $\omega \sim \omega'$. This is contrary to the usual view that large-scale kinetic energy structures drive the dynamics. Further investigation of the lifecycle of the velocity and vorticity structures, along with identification of the typical force-field structures that govern the dynamics (i.e., structures associated with the pressure gradient and viscous stress fields), will help to illumine or dispel notions regarding the existence of hierarchical coherent structures (corresponding to the inertial range) that has been expounded in different representational spaces, while having been elusive in the physical (real) space where the phenomenon of turbulence occurs. Normalized measures like $\hat{\mathbf{L}}$ might prove useful in this search for intermediate range structures.

It would also be interesting to investigate Reynolds number effects on the form and composition of the coherent flow regions. We expect that, in homogeneous isotropic turbulence, high E_k regions will manifest as jets (while high ω swirling flow regions have been shown widely), as hinted by a brief study involving reference data from the Johns Hopkins Turbulence Dataset, which has a higher Re_λ.[55] The *fraction* of Biot–Savart contribution from different vorticity levels to the generation of flow structures might have some degree of Re_λ dependence, which remains to be seen. Finally, a more detailed Biot–Savart analysis can also be performed, which considers both the magnitude of the vorticity in a region $\mathcal{R}_1$ and its distance from another region $\mathcal{R}_2$, when estimating the Biot–Savart contribution of $\mathcal{R}_1$ on $\mathcal{R}_2$. This will paint a fuller picture of the Biot–Savart composition of the velocity field and the spatial organization of coherent structures. In principle, a Helmholtz-decomposition hierarchy of structure generation can also be investigated, where, for instance, a strong velocity-swirl is largely self-induced by the core vorticity-jet, while the

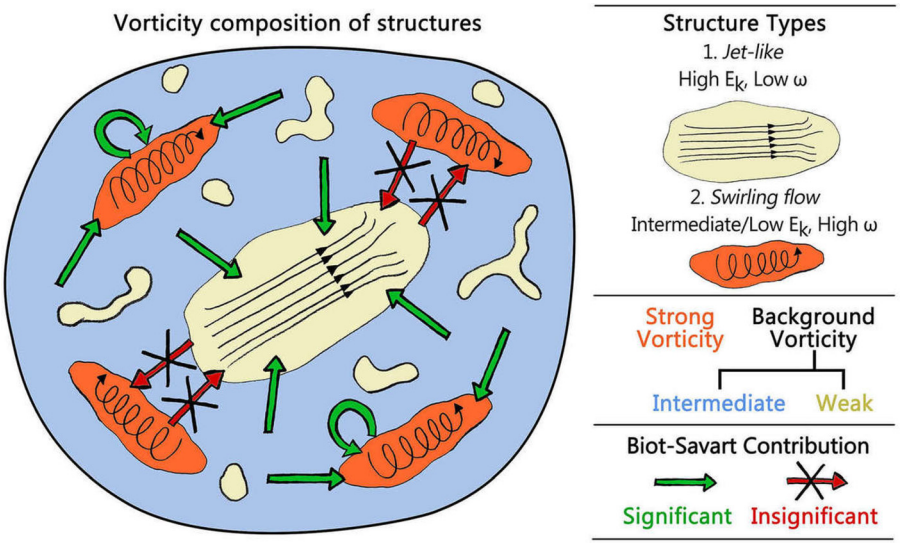

FIG. 28. Schematic of the organization of turbulence structures along with the Biot–Savart contributions. Vorticity ranges are color coded as strong vorticity (orange), intermediate background vorticity (blue), and weak vorticity (off-white). The kinetic energy containing *velocity-jets* have a low vorticity content and are induced, almost entirely, by non-local, intermediate background vorticity contributions (shown in blue), while the strong vorticity contribution is negligible. Strong vorticity regions form *vorticity-jets* and are surrounded by *velocity-swirls*. These structures are a superposition of an intermediate background vorticity generated flow and a self-induced accentuation of the swirling flow.

vorticity-jet itself will be externally induced by the divorticity, and so on, showing how structures of one field manifest in another field.

The tools presented in this paper (or modified versions of them) can be readily applied to identifying structures in any scalar or vector fields like pressure, strain, or eigenvector distributions. Furthermore, they can be useful in a wide range of fields apart from turbulence, like for identifying polar/nematic order and defects in both active and passive matter, emergent anomalous Eulerian features in active flows,[56] electromagnetic fields, or general large numerical datasets. Most importantly, we believe this correlation-decomposition framework opens a new door into studying the dynamics of turbulence from the perspective of its physical space structures and may pave the way toward a real structure-driven description of turbulence organization.

ACKNOWLEDGMENTS

The authors thank Dr. Zhao Wu (Johns Hopkins University) for providing access to the JHTD turbulence database. S.M. would also like to thank Dr. Jason Picardo (IIT-Bombay), Professor Harm Jonker (TU Delft), Elin Vesper (TU Delft), and Frank Groen (TU Delft), for some useful discussion and suggestions.

AUTHOR DECLARATIONS

Conflict of Interest

The authors have no conflicts of interest to declare.

DATA AVAILABILITY

Data and codes to calculate the correlations that support the findings of this study are available from the corresponding author upon reasonable request.

APPENDIX: CALCULATING THE BIOT–SAVART INTEGRAL

Here, we describe a few practical aspects regarding the computation of the Biot–Savart integral over periodic domains. As described in Sec. IV, for the case of incompressible flow in a periodic domain, the Helmholtz decomposition reduces to $\mathbf{u} = \mathbf{C}$ [Eq. (13)], with $\mathbf{C}$ given by the Biot–Savart formula as

$$\mathbf{C}(\mathbf{x}) = \frac{1}{4\pi}\int_V \frac{\boldsymbol{\omega}\times\mathbf{r}}{|\mathbf{r}|^3}\,\mathrm{d}V'. \tag{A1}$$

For a triperiodic domain, it is important to note that all points in the volume V are equivalent, as there is no distinct location like a "real boundary" or a "center" in the flow. This becomes important when calculating the Biot–Savart integral for points near to the "simulation boundary."

We perform the Biot–Savart integral in a radially symmetric manner, for which we first tesselate the simulation domain V (which has an edge length of N) along each direction. We then consider the volume $\widetilde{V} = (4/3)\pi r^3$, around the *fictitious* center of the original cube, for the integral, i.e., the contribution of $\mathbf{C}$ to $\mathbf{u}$. We test different values of the radius r, to check how closely does $\mathbf{C}$ recover the original velocity field $\mathbf{u}$ (while, in principle, a large enough r will reproduce the velocity field within V to 100% accuracy, discounting numerical errors). We find that an integral over $r = N\sqrt{3}/2$ generates a Biot–Savart velocity field of ≈95% accuracy in comparison with the original velocity field, while an integral over $r = N$ generates a Biot–Savart velocity of ≈99% accuracy. Hence, for this paper, we use a Biot–Savart reconstruction over $r = N$ (with $\widetilde{V} = (4/3)\pi N^3$).

An alternative calculation was also tested, where *each* point in the domain is treated as a *fictitious center*, and a radially symmetric region of radius r is created around it by tessellating the periodic cube. This region is then used to calculate the Biot–Savart velocity for the central point. This method, with $r = N$, was also found to yield an accuracy of approximately 99% in reconstructing the velocity field, while being computationally more expensive.

REFERENCES

[1]A. Tsinober, *The Essence of Turbulence as a Physical Phenomenon* (Springer, 2014), Vol. 10, pp. 978–994.
[2]U. Frisch, *Turbulence: The Legacy of an Kolmogorov* (Cambridge University Press, 1995).
[3]B. Dubrulle, "Beyond Kolmogorov cascades," J. Fluid Mech. **867**, P1 (2019).
[4]J. C. Hunt, A. A. Wray, and P. Moin, "Eddies, streams, and convergence zones in turbulent flows," Center for Turbulence Research Report No. CTR-S88, 1988.
[5]J. Jeong and A. Hussain, "On the identification of a vortex," J. Fluid Mech. **285**, 69–94 (1995).
[6]Y. Dubief and F. Delcayre, "On coherent-vortex identification in turbulence," J. Turbul. **1**, N11 (2000).
[7]M. Chong, A. Perry, and B. Cantwell, "A general classification of three-dimensional flow fields," Phys. Fluids A **2**, 765–777 (1990).
[8]G. Haller, "An objective definition of a vortex," J. Fluid Mech. **525**, 1–26 (2005).
[9]M. Farge, K. Pellegrino, and G. Schneider, "Coherent vortex extraction in 3D turbulent flows using orthogonal wavelets," Phys. Rev. Lett. **87**, 054501 (2001).
[10]A. Hussain, "Coherent structures and turbulence," J. Fluid Mech. **173**, 303–356 (1986).
[11]L. Sirovich, "Turbulence and the dynamics of coherent structures. I. Coherent structures," Q. Appl. Math. **45**, 561–571 (1987).
[12]T. Peacock and J. Dabiri, "Introduction to focus issue: Lagrangian coherent structures," Chaos **20**, 017501 (2010).
[13]T. Peacock and G. Haller, "Lagrangian coherent structures: The hidden skeleton of fluid flows," Phys. Today **66**(2), 41–47 (2013).
[14]G. Haller, "Lagrangian coherent structures," Annu. Rev. Fluid Mech. **47**, 137–162 (2015).
[15]F. Waleffe, "On a self-sustaining process in shear flows," Phys. Fluids **9**, 883–900 (1997).
[16]F. Waleffe, "Exact coherent structures in channel flow," J. Fluid Mech. **435**, 93–102 (2001).
[17]K. Deguchi and P. Hall, "Canonical exact coherent structures embedded in high Reynolds number flows," Philos. Trans. R. Soc. London A **372**, 20130352 (2014).
[18]A. Lozano-Durán and J. Jiménez, "Time-resolved evolution of coherent structures in turbulent channels: Characterization of eddies and cascades," J. Fluid Mech. **759**, 432–471 (2014).
[19]E. D. Siggia, "Numerical study of small-scale intermittency in three-dimensional turbulence," J. Fluid Mech. **107**, 375–406 (1981).
[20]R. M. Kerr, "Higher-order derivative correlations and the alignment of small-scale structures in isotropic numerical turbulence," J. Fluid Mech. **153**, 31–58 (1985).
[21]Z. She, E. Jackson, and S. Orszag, "Intermittent vortex structures in homogeneous isotropic turbulence," Nature **344**, 226 (1990).
[22]J. Jiménez, A. Wray, P. Saffman, and R. Rogallo, "The structure of intense vorticity in isotropic turbulence," J. Fluid Mech. **255**, 65–90 (1993).
[23]F. Moisy and J. Jiménez, "Geometry and clustering of intense structures in isotropic turbulence," J. Fluid Mech. **513**, 111–133 (2004).
[24]F. Argoul, A. Arneodo, G. Grasseau, Y. Gagne, E. Hopfinger, and U. Frisch, "Wavelet analysis of turbulence reveals the multifractal nature of the Richardson cascade," Nature **338**, 51 (1989).
[25]A. Alexakis and L. Biferale, "Cascades and transitions in turbulent flows," Phys. Rep. **767–769**, 1 (2018).

[26]L. Richardson, *Weather Prediction by Numerical Process* (Cambridge University Press, 1922).
[27]A. Sharma and B. McKeon, "On coherent structure in wall turbulence," J. Fluid Mech. **728**, 196–238 (2013).
[28]C. W. Rowley and S. T. Dawson, "Model reduction for flow analysis and control," Annu. Rev. Fluid Mech. **49**, 387–417 (2017).
[29]K. Taira, M. S. Hemati, S. L. Brunton, Y. Sun, K. Duraisamy, S. Bagheri, S. T. Dawson, and C.-A. Yeh, "Modal analysis of fluid flows: Applications and outlook," AIAA J. **58**, 998–1022 (2020).
[30]D. F. Gayme and B. A. Minnick, "Coherent structure-based approach to modeling wall turbulence," Phys. Rev. Fluids **4**, 110505 (2019).
[31]M. Buzzicotti, F. Bonaccorso, P. C. Di Leoni, and L. Biferale, "Reconstruction of turbulent data with deep generative models for semantic inpainting from TURB-Rot database," Phys. Rev. Fluids **6**, 050503 (2021).
[32]H. Kim, J. Kim, S. Won, and C. Lee, "Unsupervised deep learning for super-resolution reconstruction of turbulence," J. Fluid Mech. **910**, A29 (2021).
[33]F. Waleffe, "The nature of triad interactions in homogeneous turbulence," Phys. Fluids A **4**, 350–363 (1992).
[34]L. Portela, "Identification and characterization of vortices in the turbulent boundary layer," Ph.D. thesis (Stanford University, School of Mechanical Engineering, 1997).
[35]L. Portela, "The vortex concept and its identification in turbulent boundary layer flows," in *IUTAM Symposium on Simulation and Identification of Organized Structures in Flows* (Springer, 1999), pp. 249–258.
[36]P. E. Hamlington, J. Schumacher, and W. J. Dahm, "Direct assessment of vorticity alignment with local and nonlocal strain rates in turbulent flows," Phys. Fluids **20**, 111703 (2008).
[37]G. Elsinga, T. Ishihara, M. Goudar, C. Da Silva, and J. Hunt, "The scaling of straining motions in homogeneous isotropic turbulence," J. Fluid Mech. **829**, 31–64 (2017).
[38]G. K. Batchelor, *The Theory of Homogeneous Turbulence* (Cambridge University Press, 1953).
[39]J. Wu, H. Ma, and M. Zhou, *Vorticity and Vortex Dynamics* (Springer Science & Business Media, 2007).
[40]H. B. Phillips, *Vector Analysis* (John Wiley, 1933).
[41]L. Biferale, P. Perlekar, M. Sbragaglia, S. Srivastava, and F. Toschi, "A lattice Boltzmann method for turbulent emulsions," J. Phys.: Conf. Ser. **318**, 052017 (2011).
[42]K. Alvelius, "Random forcing of three-dimensional homogeneous turbulence," Phys. Fluids **11**, 1880–1889 (1999).
[43]A. T. Cate, E. V. Vliet, J. Derksen, and H. Van den Akker, "Application of spectral forcing in lattice-Boltzmann simulations of homogeneous turbulence," Comput. Fluids **35**, 1239–1251 (2006).
[44]A. Ten Cate, J. Derksen, L. Portela, and H. Van Den Akker, "Fully resolved simulations of colliding monodisperse spheres in forced isotropic turbulence," J. Fluid Mech. **519**, 233–271 (2004).
[45]P. Perlekar, L. Biferale, M. Sbragaglia, S. Srivastava, and F. Toschi, "Droplet size distribution in homogeneous isotropic turbulence," Phys. Fluids **24**, 065101 (2012).
[46]S. Mukherjee, A. Safdari, O. Shardt, S. Kenjeres, and H. Van den Akker, "Droplet-turbulence interactions and quasi-equilibrium dynamics in turbulent emulsions," J. Fluid Mech. **878**, 221–276 (2019).
[47]P. Moin and K. Mahesh, "Direct numerical simulation: A tool in turbulence research," Annu. Rev. Fluid Mech. **30**, 539–578 (1998).
[48]B. Pearson, T. Yousef, N. Haugen, A. Brandenburg, and P. Krogstad, "Delayed correlation between turbulent energy injection and dissipation," Phys. Rev. E **70**, 056301 (2004).
[49]Z. She, E. Jackson, and S. Orszag, "Structure and dynamics of homogeneous turbulence: Models and simulations," Proc. R. Soc. London, Ser. A **434**, 101–124 (1991).
[50]S. Mukherjee, "Unravelling turbulent emulsions with lattice-Boltzmann simulations," Ph.D. thesis (Delft University of Technology, 2019).
[51]E. Perlman, R. Burns, Y. Li, and C. Meneveau, "Data exploration of turbulence simulations using a database cluster," in *Proceedings of the 2007 ACM/IEEE Conference on Supercomputing* (ACM, 2007), p. 23.
[52]Y. Li, E. Perlman, M. Wan, Y. Yang, C. Meneveau, R. Burns, S. Chen, A. Szalay, and G. Eyink, "A public turbulence database cluster and applications to study Lagrangian evolution of velocity increments in turbulence," J. Turbul. **9**, N31 (2008).
[53]L. Wei, G. E. Elsinga, G. Brethouwer, P. Schlatter, and A. V. Johansson, "Universality and scaling phenomenology of small-scale turbulence in wall-bounded flows," Phys. Fluids **26**, 035107 (2014).
[54]S. B. Pope, *Turbulent Flows* (Cambridge University Press, 2001).
[55]S. Mukherjee, M. Mascini, and L. M. Portela, "Correlation and decomposition framework for identifying and disentangling flow structures: Canonical examples and application to isotropic turbulence," arXiv:2011.07455 (2020).
[56]S. Mukherjee, R. K. Singh, M. James, and S. S. Ray, "Anomalous diffusion and Lévy walks distinguish active from inertial turbulence," Phys. Rev. Lett. **127**, 118001 (2021).